THE UNIVERSITY OF CHICAGO

X-RAY INDUCED LUMINESCENCE IMAGING: SENSITIVITY MEASUREMENTS, SELECTIVE PLANE GEOMETRY, AND DUAL-MODALITY X-RAY FLUORESCENCE IMAGING

A DISSERTATION SUBMITTED TO
THE FACULTY OF THE DIVISION OF THE BIOLOGICAL SCIENCES
AND THE PRITZKER SCHOOL OF MEDICINE
IN CANDIDACY FOR THE DEGREE OF
DOCTOR OF PHILOSOPHY

COMMITTEE ON MEDICAL PHYSICS

BY
BRYAN P. QUIGLEY

CHICAGO, ILLINOIS
JUNE 2018

To Grandma Marilyn, for encouraging an appreciation of science and education ever since I was a child.

"Be a physician, Faustus, heap up gold,
And be eternized for some wondrous cure.
Summum bonum medicinae sanitas:
The end of physic is our body's health
Why Faustus, hast thou not attained that end?"

— Christopher Marlowe, *The Tragical History of Dr. Faustus*

TABLE OF CONTENTS

LIST OF FIGURES

LIST OF TABLES

ACKNOWLEDGMENTS

First and foremost, I would like to acknowledge my thesis advisor Dr. Patrick J. La Rivière for his support and guidance throughout this work. When I first started at the University of Chicago, I was tasked with finding a rotation lab for the fall quarter. After a series email conversations with other labs that led nowhere, I reached out to Dr. La Riviere to see if he had a project. We met later that afternoon and discussed luminescent nanoparticles and small animal irradiators. The interaction was straightforward and uncomplicated; it just felt right. I accepted the lab rotation and achieved my first radioluminescence image that December before leaving for Christmas break. This marked the beginning of what would be another four and half years of experimental research. Throughout this time, Dr. La Riviere provided insight and support during the various stages of the research. I was continually amazed at the energy and dedication he put towards my project while simultaneously juggling other students and collaborators working on entirely different imaging modalities. I honed my writing abilities, presentation skills, and analytical reasoning through his mentorship, and I am forever grateful for the chance to learn and grow as a member of his research group.

I would like to acknowledge Dr. Rodney D. Wiersma, and Dr. Chin-Tu Chen for serving on my thesis advisory committee. Dr. Wiersma was instrumental in the dosimetry measurements in the small animal irradiator and Dr. Chin-Tu Chen offered invaluable insight to my understanding of molecular imaging and its applications. Early on in my research, I relied heavily on Dr. Shih-Hsun Cheng and Dr. Jeffrey Souris during my first experiments with the nanoparticles. They helped with synthesizing the nanoparticles and imaging within the small animal irradiator.

I would like to thank the present and former members of the La Riviere research group. Dr. Dimple Modgil, Phil Vargas, Dr. Dave Rigie, Corey D. Smith, Talon Chandler, and Scott Trinkle. They were a great community to commiserate with during the difficult moments of research and celebrate with after achieving successful results. A special thank-you to Dimple

for all the snacks and meals of delicious Indian food she brought to the lab. I'm grateful for all the guidance Dave provided me as a senior student in the lab and for answering my questions on the thesis writing process. Finally, a huge thank-you to Corey for all the help with the deconvolutions and coding. He was a knowledgeable resource as I learned Python during the final stretch of my research and offered countless tips on how to improve my coding technique. Furthermore, he made me a better chef by sharing many recipes with me and teaching me advanced cooking techniques.

Next, I would like to thank my family for their continued support throughout my graduate education. Mom, Dad, Sean, Conor, and Grandma, I love you all so much and you have been instrumental to my success. My mother and father have always given me a great deal of support for all my educational endeavors, especially for my undergraduate education at Tulane University. My mother provided constant encouragement throughout my time in the graduate program in medical physics, and she kept me going with countless conversations on the phone telling me to push through whatever project I was struggling with. My father similarly was very supportive throughout the process until the end. A big thank-you for being there during my thesis defense. It was always great to get out of the city and visit my brothers during my time in graduate school. I truly feel blessed to be part of the trio of Quigley brothers. I would like to acknowledge Grandma Marilyn for the many phone calls and letters I received during my education. You were the best cheerleader I could ask for.

Finally, I would like to say a special thank-you to Calvert House. You were a refuge during my last year at the University of Chicago as I sought to leave behind the vices of an extended adolescence and mature into an adult with better habits. It was beautiful to learn about the Catholic faith from the RCIA classes and the members of the Calvert community. I am extremely grateful for the chance to complete my conversion to Catholicism with Calvert during this last Holy Week and Easter. Thank you for everything you have taught me as I begin this new journey in my life.

ABSTRACT

X-ray induced luminescence imaging employs lanthanide-doped nanophosphors that emit near-infrared light in the presence of ionizing radiation. This nascent modality has potential applications in molecular imaging or theranostic medicine. The penetrating nature of x-rays, which activate the imaging probes, allows for imaging at depths beyond conventional optical fluorescence imaging in a diffuse environment like mammalian tissue. The x-ray induced luminescent properties of europium-doped nanophosphors are initially characterized with experimental measurements within a small animal irradiator. Measurements in optical gel phantoms are used to calibrate an imaging model that is then used for simulations that evaluate the sensitivity of the nanoparticles with respect to concentration, dose, and imaging depth. Shaping the incoming x-ray beam geometry constrains the x-ray induced luminescence to a known region within the object, thus reducing the ill-posedness of reconstructing nanophosphor distributions at depth from a detected surface radiance measurement. A selective-plane geometry is presented which allows for a two-dimensional deconvolution-based reconstruction and is experimentally demonstrated in optical gel phantom measurements. A benchtop system with a pencil beam geometry is presented which allows for dual-modality imaging of x-ray induced luminescence and of x-ray fluorescence. The x-ray induced luminescence reconstruction reduces to a one-dimensional deconvolution and the reconstructed x-ray fluorescence image serves as prior information that enhances the x-ray induced luminescence reconstruction. Experimental measurements demonstrate that the x-ray luminescence/x-ray fluorescence joint reconstruction combines the high resolution of the x-ray fluorescence imaging with the high sensitivity of the x-ray luminescence imaging.

CHAPTER 1
INTRODUCTION TO X-RAY INDUCED LUMINESCENCE IMAGING

1.1 Introduction

X-ray induced luminescence imaging is a hybrid x-ray/optical technique that uses radioluminescent nanoparticles that emit optical light in response to radiation dose deposited in their surrounding environment. Depending on the nanophosphor composition and the energy of the incident x-rays, it is also possible to image the nanoparticles using x-ray fluorescence, in which incident x-rays stimulate emission of characteristic x-rays from high-Z components of the nanoparticles. This chapter begins with a brief explanation of the x-ray induced luminescence and fluorescence processes. It then presents a literature review of the field of x-ray luminescence computed tomography from its inception in 2010 to the state of research in 2018. Finally the chapter concludes with a brief discussion of diffuse optical imaging and outlines the limitations to reconstructing nanophosphor distributions in tissue from a surface radiance measurement. Methods for reducing the ill-posed nature of x-ray induced luminescence imaging are presented, including dual-modality imaging with x-ray fluorescence.

1.2 X-ray induced luminescence and x-ray fluorescence phenomena

X-ray induced luminescence imaging employs nanophosphors that emit visible light in response to x-ray irradiation. The nanophosphors are composed of scintillating nanocrystals similar to the compounds used in some x-ray and gamma-ray detectors. Various radioluminescent nanoparticles are currently being explored as potential molecular imaging and/or

therapeutic agents. For imaging alone, such probes would be used in low concentrations for targeting molecular structures. In such an environment, the vast majority of x-ray interactions are with the surrounding material, which can be considered as water equivalent for mammalian tissue. These x-rays deposit their energy in the tissue and liberate fast electrons via Compton scattering, which go on to cause further ionization events. In the resulting cascade of liberated electrons, some energy is deposited across the radioluminescent nanocrystals. This energy then excites electrons in the phosphorescent element that dopes the nanoparticles through an upconversion process. When these electrons return to a lower-energy state, a visible light photon is released, which is the resulting x-ray induced luminescence. Radioluminescence with low concentrations of nanoparticles is then dependent on the dose deposited in surrounding tissue rather than direct x-ray interactions with the nanophosphors.

X-ray fluorescence is a process that is element specific and depends heavily on the energy of the incoming photons. X-rays interact with an element's inner shell electrons via the photoelectric process and liberate a bound electron. Then two different events may occur. An outer shell electron will drop to fill the inner shell vacancy and the atom will either emit an x-ray photon or an Auger electron. The former case is known as x-ray fluorescence and the emitted photon's energy is dependent on the binding energy difference between the outer and inner shell electrons. This process requires the incoming x-ray photons to have an energy greater than or equal to the binding energy of the inner shell electron and has the highest probability of occurring if the energy is only slightly above the threshold. The emitted fluorescent x-rays are characteristic of the element interacting with the incident x-rays via the photoelectric effect and the fluorescence can therefore be used to identify the element.

1.3 Review of x-ray induced luminescence imaging

The physical phenomenon of x-ray induced luminescence has been exploited for decades in medical imaging due to the fact that it has traditionally been easier to use a bulk scintillator to convert incoming x-rays and gamma-rays into optical photons for detection with a charge-coupled device (CCD) camera or photomultiplier tube than engineer a detector that directly images the ionizing rays. Bulk inorganic scintillators have been well studied and developed for medical imaging systems such as fluoroscopy, x-ray computed tomography, and positron emission tomography [3]. More recently, a new generation of x-ray scintillating materials has been developed by incorporating materials similar to these inorganic scintillators into the fabrication of nanoparticles [4, 5, 6, 7]. These resulting nanophosphors luminescence in the presence of ionizing radiation like the bulk scintillators, but have a novel set of applications in their particulate form as probes for molecular imaging or as therapeutic agents.

Traditional optical fluorescence imaging relies on optical light to activate the probes, which limits imaging sensitivity and resolution at depths beyond a few millimeters. There is a loss of sensitivity due to absorption of the excitation light as it travels through tissue to reach the probes below the imaging surface and further absorption of the optical fluorescence signal as it travels out of the turbid environment. There is also autofluorescence in the tissue, which reduces the ability to detect the optical photons specifically generated by the fluorescent probes. On top of this, resolution greatly suffers due to scattering of both the excitation source and the resulting optical fluorescence signal. These obstacles to optical imaging at depth in tissue are mitigated by activating the optical probes with x-rays. The higher-energy x-ray photons are far more penetrating and can reach probes at depth without significant attenuation. Furthermore they achieve this with minimal scattering. While the optical luminescence signal produced by the nanophosphors still undergoes a great deal of scattering events before detection, its origin is confined to the region of the x-ray beam. The potential for imaging in tissue with these x-ray activated phosphorescent probes was

demonstrated experimentally by the group of Anker with nanophosphors embedded in raw meat [8, 9].

Initial work investigating this novel imaging technique sought to characterize basic properties of the scintillating probes. They exhibited a linear luminescence response to both nanophosphor concentration and radiation dose [10, 11]. The first generation of x-ray luminescence tomographic imaging employed a first-generation tomographic geometry using a pencil-beam illumination with multiple positions comprising a view angle and multiple view angles comprising a sinogram for a slice in the object [12, 13, 14]. The resulting measurements of emitted optical photons were considered to be line integrals through the nanophosphor distribution. This work successfully demonstrated in both numerical simulations and phantom experiments the feasibility of tomographic imaging with x-ray activated nanophosphors. However this imaging geometry suffered from long image acquisition times that restricts *in vivo* imaging applications and results in high radiation doses.

Imaging times were reduced by widening the x-ray source from a pencil beam to a cone-beam, which was demonstrated in phantom imaging by Chen *et al* [15]. A further reduction in imaging time can be achieved by limiting the x-ray luminescence measurement to a single view, which was shown in simulation, phantom, and *in vivo* measurements by Liu *et al* [16]. Similarly, imaging time was reduced for the first-generation geometry of x-ray luminescence computed tomography by acquiring a limited-angle sinogram for use in reconstructing a slice [17].

These faster imaging approaches using wider x-ray fields and fewer views result in greater ambiguity in the reconstructions. Diffuse optical tomographic reconstructions are already an ill-posed problem, but this is heightened by reducing the selectiveness of the beam geometry. Therefore techniques like compressive-sensing are implemented in these reconstructions in order to recover the original nanophosphor distribution [18]. Other approaches to refining the reconstruction for cone-beam x-ray luminescence computed tomography involve the use

of structural *a priori* information gathered from x-ray computed tomography [19]. Further advancements on the reconstruction include the monitoring of x-ray scatter in the phantom and modeling the diffuse transport equations governing optical photon diffusion in the object [20, 21].

Other developments in the initial wave of x-ray luminescence research include multiplex imaging with nanophosphors emitting distinct wavelengths in small animals [22]. Numerical simulations for higher-resolution imaging suggested the use of zone plates [23] and polycapillary lenses [24] in order to focus the x-rays with a greater flux and a smaller beam width than what is achievable using a collimated pencil beam. Finally, a more complex imaging technique known as stored luminescence computed tomography was suggested, wherein nanophosphors activated by incoming x-rays then had to be illuminated with a secondary excitation laser to release optical photons [25]. All the research presented thus far was summarized in a review article by Ahmad *et al* [26]. In addition, a well-written overview of the various imaging geometries of x-ray luminescence computed tomography and the associated reconstruction techniques is outlined in a book chapter written by Xin Liu *et al* [27].

Similar to x-ray luminescence imaging, Cerenkov luminescence imaging detects an optical signal generated by x-rays, but without the need for exogenous probes. Cerenkov luminescence results when an charged particle travels through a dielectric medium faster than the phase velocity of light in that medium. High-energy x-ray irradiation releases fast electrons in tissue that surpass this threshold. The luminescence is dominated by shorter-wavelength visible light, because the intensity of Cerenkov luminescence is the inverse square of the emitted wavelength. Clinically it is limited to imaging applications within radiation therapy as it requires a minimum x-ray energy of 260 keV. Cerenkov tomography has been demonstrated experimentally using LINACs [28]. More recently, Pogue *et al.* have proposed a new imaging geometry using a planar x-rays that they call Cerenkov-excited luminescence sheet imaging (CELSI) [29, 30].

The sheet-beam geometry serves as a midpoint between cone beam and pencil beam geometries. The planar x-rays constrain the luminescence in one dimension, but create a much greater flux than the pencil beam by irradiating the object in the other two dimensions. Initial numerical simulations were performed for x-ray luminescence imaging using a sheet-beam illumination geometry [31]. Then experimental studies with a sheet-beam were presented by Quigley *et al.*, who use the term selective plane x-ray induced luminescence imaging (SPXIL) [32]. This work successfully imaged europium-doped nanophosphors in diffuse optical gel phantoms using a deconvolution-based reconstruction that took advantage of the sheet-beam imaging geometry.

The advantages of pencil-beam and sheet-beam geometries can be merged together using multiple pinhole collimator based x-ray luminescence computed tomography. Here an array of pencil beams are used to irradiate the object. It has a greater flux than a single pencil, but the reconstruction from the diffuse optical signal is more well-posed than in a full sheet beam illumination. Li *et al.* demonstrated this technique using in a simulation with four collimated pencil beams and then reported an experimental reconstruction using a dual-collimated pencil-beam geometry [33]. This approach offers the ability to greatly shorten imaging times from the first-generation pencil-beam geometry by providing an increase in x-ray flux. This was expanded upon by introducing a collimation grating or coded aperture on the x-ray source so that the illumination pattern produces more x-rays than a simple series of pencil beam. Numerical simulations demonstrated that this approach could achieve a marked enhancement in resolution compared to a cone-beam geometry with only slightly longer image acquisition times [34].

Another novel approach in experimental x-ray luminescence imaging is the use of an optical fiber-based detection system that offers fast, sparse sampling of the luminescence [35, 36]. An array of optical fiber bundles interfacing with the object's surface and connected to a PMT offers faster detection with a wider array of view angles for a single pencil beam

position than a single EMCCD camera-based detection scheme. These experiments also employed a polycapillary lens on the x-ray source in order to create a pencil beam with a greater flux, as suggested by earlier work with numerical simulations.

Advancements have also been made on the reconstructions for cone-beam x-ray luminescence computed tomography to address the ambiguity in reconstructing diffuse optical measurements. Xing *et al.* have presented a Bayesian-based method for cone-beam reconstructions, which uses a Gaussian Markov random field to mitigate the ill-posed nature [37]. Another proposed improvement in the reconstruction is using a prior model based on absorbed x-ray dose. Previous work with cone-beam x-ray luminescence computed tomography used a forward model based on the intensity distribution of x-rays within the object. However, the absorbed dose in a region induces the luminescence of the nanophosphors and therefore is a more accurate model of the physical process. Numerical simulations and phantom experiments using this approach with Tikhonov regularization demonstrated improvements in image quality compared to the traditional forward model based on x-ray intensity [38].

Up to this point, most of the research has been focused on demonstrating novel imaging geometries and improved image reconstruction strategies for x-ray luminescence computed tomography. Most experimental measurements in phantom and *in vivo* relied on sources with concentrations of nanophosphors on the order of 1 g/mL. These high concentrations are visible on x-ray computed tomography scans, making x-ray luminescence reconstruction unnecessary; these concentrations are irrelevant in the context of imaging molecular targets. Therefore some groups have sought to evaluate the potential sensitivity of x-ray luminescence imaging. One group researching sensitivity presented simulated results showing that an x-ray induced luminescent signal from a 1 mg/mL source could be detected 2 to 4 cm at depth in mammalian tissue using therapeutic radiation dose of 1 Gy [32]. Other researchers published experimental measurements using a pencil beam geometry, and they demonstrated imaging

concentrations as low as 0.01 mg/mL or 27.6 μM to a depth of 1.1 cm in a diffuse optical gel phantom [39]. While this second result did not cite dose, their measurements are comparable after accounting for the difference in exposure times, x-ray tube currents, phantom optical properties, source depths, and concentrations.

However these results on sensitivity have been tempered in a discussion by Pratx, where he outlines limitations of x-ray luminescence in molecular imaging and photodynamic therapy [40]. He describes the potential for background luminescence caused by radiation interacting with air, water, or biological molecules such as L-tryptophan. On top of this, some tissues such as oral cavity and digestive tracts can produce persistent luminescence post-radiation, further complicating the detection of nanophosphors and reducing the sensitivity of targeted x-ray luminescence. The effects of extraneous luminescence has begun to be characterized in experimental research [41], but more research is needed to better quantify how this effect limits the potential applications of x-ray induced luminescence imaging.

Nanophosphor engineering is another avenue of important research. The radioluminescent nanoparticles need to be functional in a physiological environment. PEGylated nanophosphors have exhibited colloidal stability in water [42]. Surface modifications to the nanoparticles can increase their luminescence efficiency while also making them more biocompatible [43]. New types of radioluminescent nanoparticles are being studied which do not rely on traditional phosphorescent scintillators. Instead they use metal clusters with biomolecules [44, 45]. Increased luminescence efficiencies of the probes will be vital for the success of x-ray luminescence imaging as it allows for lower radiation doses or greater depths of imaging in tissue.

Finally, the potential applications of x-ray luminescence computed tomography extend beyond simple reconstructions of nanoparticle distributions within a phantom or a small animal. The feasibility of endoscopic imaging has been investigated [46]. X-ray luminescence could also be used for monitoring drug delivery in the body [47]. A unique application which

does not require exogenous nanophosphors is implant imaging. An implant is engineered with nanophosphors on its surface which are then covered with a pH sensitive film. Changes in the pH environment around the implant would affect resulting x-ray luminescence measurements thus allowing a way to monitor infections [48]. Many of the challenges of imaging in tissue are greatly reduced in the realm of microscopy, where the depths of imaging can be an order of magnitude less compared to small animal or medical imaging. X-ray activation of luminescent probes has been implemented for optical imaging below the diffraction limit [49]. While these potential applications differ from standard tomography applications described in the previous paragraphs, their success will still be dependent on the development of proper modeling of the diffuse light transport of x-ray luminescence in tissue and could benefit from novel imaging geometries applied to their specific use cases.

1.4 The ill-posed nature of optical imaging in tissue

As previously mentioned in the literature review, x-ray induced luminescence imaging in tissue is an ill-posed problem i.e. the image reconstruction inverse problem does not have a well defined solution. This arises from the diffuse optical transport equations for light propagating in tissue and the ambiguity of reconstructing a three-dimensional distribution of nanophosphors from a two-dimensional surface radiance measurement. The ill-posed nature persists even in a noiseless system, since it arises from the fundamental equations governing the phenomenon of diffuse optical imaging. These results are well described in Chapter 9 of Lorenzo's book on diffuse light propagation [1].

As the visible light travels through a diffuse medium, such as tissue, it is scattered and absorbed. The further it travels from its source, the more its intensity is reduced and the more spread out its intensity profile becomes. In the case of a luminescent point source in a homogeneous, semi-infinite medium, the attenuation of the signal and its spread are defined by radially symmetric diffusion transport equations, which are based on the optical

properties of the medium. Nevertheless, the situation becomes more complicated when the luminescent object is no longer a point source and its distance from the point of measurement is unknown.

Imagine a two-dimensional circular luminescent source with a fixed radius in an optically homogeneous diffuse medium. Now define a plane of measurement parallel to the luminescent disc at a distance of z from it. The real luminescent source and the intensity profile in the plane of measurement are depicted in Figure 1.1. The optical parameters of the diffuse medium are known and so are the corresponding equations governing the diffusion of light in the medium. As expected, the intensity profile has a spread wider than the diameter of the luminescent source. Now imagine that there is no knowledge of the luminescent source's shape and its depth. From the intensity profile measurement it is impossible to reconstruct accurately the luminescent source's distribution without any prior information about the source depth. Rather than a small, bright source at depth z below the plane of measurement, the luminescent source could be a wider, but weaker distribution of nanophosphors closer to the plane of measurement. Indeed, there are an infinite number of solutions for luminescent source distributions at varying depths that would produce the same intensity profile in the plane of measurement.

Note that the ill-posed inversion example cited above was for a simple case of a two-dimensional luminescent source distribution in an optically homogeneous environment. Reconstructing a three-dimensional distribution of nanophosphors in an optically heterogeneous medium from a two-dimensional intensity profile has a greater degree of ambiguity. Furthermore, x-ray induced luminescence imaging measurements have a number of sources of noise that add more complexity to the inverse problem. The camera detectors have readout noise, thermal noise, and shot noise. As discussed in the literature review, there is potentially some background luminescence caused by the irradiation of tissue and air which reduces sensitivity, and background luminescence in the tissue may behave differently than the light emitted

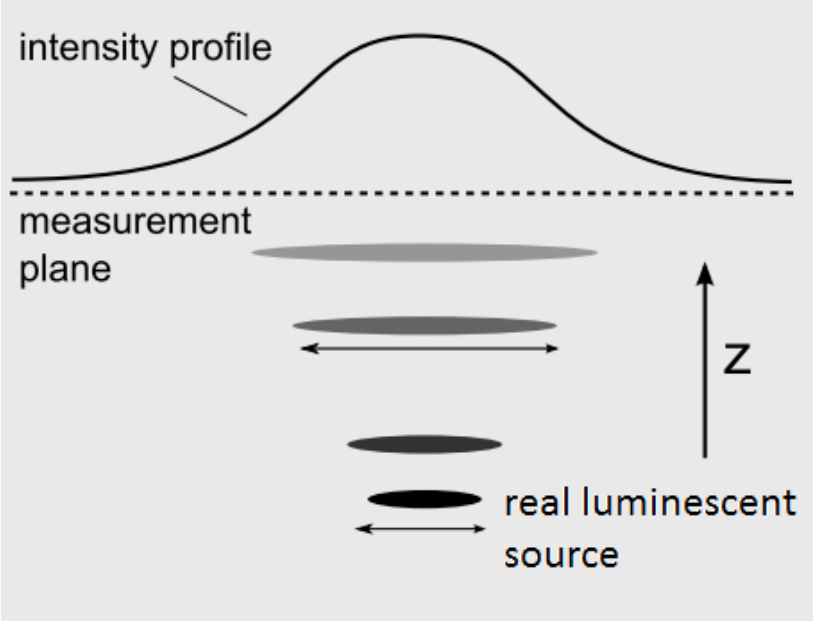

Figure 1.1: Luminescent source in a homogeneous optically diffuse medium at depth z below the plane of measurement and the resulting intensity profile. There are an infinite number of intensity profiles located at varying depths with different distributions of luminescence that produce the identical intensity profile in the measurement plane. Diagram sourced from Chapter 9 of Lorenzo's *Principles of Diffuse Light Propagation* [1].

from the nanophosphors. Therefore full irradiation with x-rays of a diffuse object containing luminescent nanophosphors will be able to discern little information about the concentration and distribution of the nanophosphors from the surface radiance measurements. However, there are ways do reduce the ill-posedness of the reconstruction as outlined by Lorenzo.

Introducing a spatial dependence on the nanophosphors emissions will make the reconstruction less ill-posed. This is an area where x-ray luminescence excels compared to other optical imaging techniques like fluorescence or bioluminescence. In the case of fluorescence, the excitation source is also visible light so it scatters and its distribution spreads out as it travels to deeper depths in the tissue. Thus there is a depth-dependent limitation to encoding spatial dependence in fluorescence imaging. In bioluminescence imaging, a substrate like luciferin is injected into the animal and it causes all of the cells containing the luminescent proteins to light up. Therefore it is impossible to introduce a spatial dependence to the

luminescence emission. X-rays are well suited for spatially encoding the luminescence of the nanophosphors. They are penetrating and are far less susceptible to scattering compared to to visible light, such as the lasers used in fluorescence imaging. This thesis examines the use of x-ray sheet beams and pencil beams for creating a spatial dependence in x-ray induced luminescence imaging and presents the associated reconstructions for phantom studies.

Another way to tackle the reconstruction problem is to introduce prior information when it is available. X-ray luminescence imaging can be integrated into a system that already does x-ray computed tomography (CT) imaging by including a camera and lens to detect optical photons. Thus a dual modality system could use the x-ray CT imaging to construct anatomical priors of the imaging object and estimate optical properties [50]. Something similar could be done using anatomical information from magnetic resonance imaging.

For appropriate nanoparticles and with added detection hardware, x-ray fluorescence can be used in tandem with x-ray luminescence to determine prior information about the nanoparticle distributions. X-ray fluorescence has the advantage of emitting x-ray photons that can escape tissue with minimal scattering compared to x-ray luminescence. This allows the x-ray fluorescence to form a direct image of the nanophosphors within the field of x-ray irradiation. The drawback of the x-ray fluorescence is that it generally emits far fewer photons compared to x-ray luminescence imaging. While x-ray luminescence imaging lacks the resolution of x-ray fluorescence, it has a greater sensitivity due to the generation of far more optical photons. During the irradiation, the nanophosphors will also luminescence, allowing simultaneous imaging after which the x-ray fluorescence reconstruction can be used as prior information to constrain the x-ray luminescence reconstruction.

CHAPTER 2

EXPERIMENTAL X-RAY INDUCED LUMINESCENCE IMAGING

2.1 Introduction

This chapter focuses on experimental x-ray induced luminescence imaging within a small-animal irradiator. It outlines the equipment used for radioluminescence imaging and fabrication of the nanophosphors. Initial imaging experiments explore the basic properties of the nanophosphors and their luminescence. Then a calculation of the luminescent efficiency of the nanoparticles is determined via a series of measurements. The chapter concludes with a section on optical gel phantom fabrication. These gel phantoms are important for research in subsequent chapters were they serve as a simulated tissue environment in which the nanoparticles are studied.

2.2 Materials and Methods

Experimental x-ray induced luminescence imaging requires a radiation source, x-ray activated nanophosphors, and a detector for the optical photons produced. The radiation source used for experimental radioluminescence imaging in this thesis is a small-animal irradiator (X-RAD 225Cx, Precision X-ray), which has multiple advantages. The high flux of the x-ray treatment tube allows sufficient radiation for activation of nanophosphors, even if they are located multiple centimeters deep within a phantom. Furthermore, the on-board computed tomography scanner allows anatomical imaging of phantoms containing the nanoparticles, and the system can easily move the nanophosphor sources to the isocenter of the irradiator with the motorized translational treatment bed.

The radioluminescence detection is accomplished with a cooled CCD (CoolSNAP HQ-

2, Photometrics) and a macro lens (DX Micro-NIKKOR, Nikon). This allows for relative measurements of the luminescent intensity of the nanoparticles. As shown in this chapter, the CCD camera is capable of characterizing basic properties like the relationships between nanoparticle concentration and radiation dose with x-ray induced luminescence. However it lacks the ability to measure an absolute photon count. Therefore a later section in the chapter introduces an indirect method for determining the photon output of the nanophosphors by using an optical mouse phantom with a calibrated LED.

Optical imaging within range of an x-ray source has some unique challenges. The camera detector is designed for low energy visible light photons and thus, is sensitive to interactions with high energy x-ray photons. The pixels in a CCD camera have an electron well that stores a charge proportional to the visible light photons detected. A single x-ray photon can interact with the pixel and flood the electron well, and the charge can spill over into neighboring pixels. This effect is more pronounced for longer exposure times that correspond to imaging during a therapeutic exposure. Therefore proper shielding of the camera is necessary to block stray x-rays from the treatment head and scattered x-rays from the object and bottom of the irradiator. The experimental setup here uses lead plates and leaded glass to shield the CCD camera from stray radiation. Due to imperfect shielding, some x-rays still interact with the CCD sensor causing hot pixels. Another way that this is managed is by acquiring multiple images and averaging across pixel values, since the scattered x-rays are random interactions that are not spatially correlated across pixels.

2.3 Nanophosphor Fabrication

The radioluminescent nanoparticles investigated in this work are yttrium oxide nanocrystals doped with europium (Y_2O_3:Eu^{3+}). The synthesis takes approximately a day, with an intermediate step leaving the nanoparticles to dry out overnight. Nanophosphor synthesis is a relatively simple process that requires only three chemicals: Yttrium (III) nitrate

hexahydrate, europium (III) nitrate hexahydrate, and urea. The yttrium nitrate and the europium nitrate are combined in a general urea homogeneous precipitation method. The product of this reaction is then separated out from the solution and put in a furnace. This stage is important, because it causes the europium to migrate into the nanocrystals, where it plays a critical role in the production of radioluminescence. The recipe for synthesizing the nanoparticles is as follows.

1. Dissolve 0.196 g of $Y(NO_3)_3 \times 6H_2O$ in 25 mL of distilled water. Dissolve 0.033 g of $Eu(NO_3)_3 \times 6H_2O$ in 25 mL of distilled water. Dissolve 3 g of Urea in 25 mL of distilled water.

2. Mix all components in a round bottle and sonicate until the solution is clear.

3. Heat the solution up to 85 °C by placing the round bottle in a oil bath on a magnetic stirring hot plate. Stir the solution at 500 rpm for 4 hours. The solution will turn an opaque white color when the reaction is finalized.

4. Pour the solution into 50 mL tubes and centrifuge at 8000 rpm for 15 minutes in order to separate the precipitate from the solution.

5. Pour off the excess water and leave the precipitate in the tubes to dry out over night at 100 °C.

6. Scrape the dried precipitate from the tube and transfer it to a ceramic boat. Place the ceramic boat in a furnace and anneal the nanoparticles at 800 °C for 4 hours.

7. After annealing is complete and the nanoparticles have cooled, check their phosphorescence with a short wavelength UV lamp. An example of a successful synthesis with the nanoparticles in the ceramic boat phosphorescing, is shown in Figure 2.1.

The yield from these proportions was approximately 33 mg of nanophosphors. The product ranges in the size of small chips to dust. The nanoparticles should be ground up

evenly to a dust before attempting to dissolve the nanoparticles into various solutions in preparation for measurements.

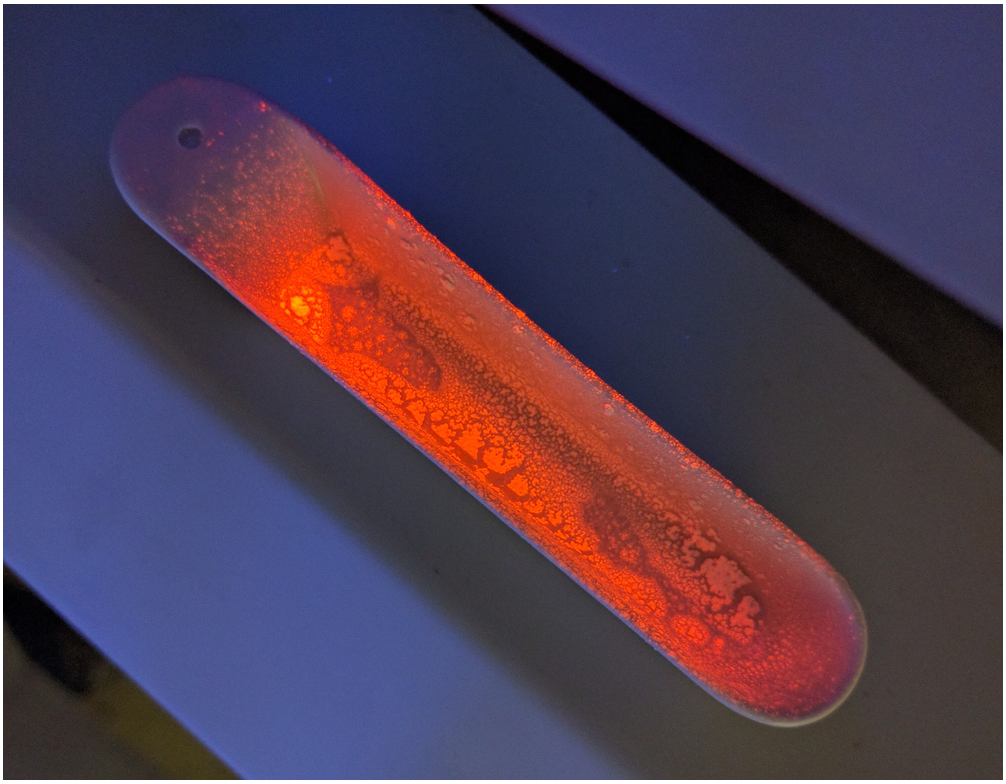

Figure 2.1: Nanoparticles in the ceramic boat after they have been annealed in the furnace for 4 hours. A short-wave UV lamp is used to check for phosphorescence, which indicates the synthesis was a success.

2.4 Nanophosphor Characterization

The first stage of the research is to characterize the fundamental properties of the radioluminescent nanoparticles. In this section the optical emission spectrum of the nanoparticles is measured and the relationship between nanophosphor concentration and x-ray induced luminescence is evaluated. Finally the relationship between the x-ray tube settings and the radioluminescence is investigated. These fundamental properties will serve as building blocks for subsequent theory, calculations, and simulations based on x-ray induced luminescence imaging.

2.4.1 Spectral Emission

Approximately 5 mg of synthesized nanophosphors were dissolved in an aqueous solution within a cuvette. A fiber-optic cable connected to a spectrometer (USB4000, Ocean Optics) was interfaced with the surface of cuvette. The solution was irradiated within the small animal irradiator with a tube voltage of 125 kVp and a tube current of 23 mA. The resulting spectral emission of the x-ray induced luminescence was measured and is plotted in Figure 2.2. The nanophosphors have a primary emission peak of approximately 611 nm with smaller secondary peaks around 590 nm, 627 nm, and 709 nm. These measured emission wavelengths match those reported in the literature [7, 11].

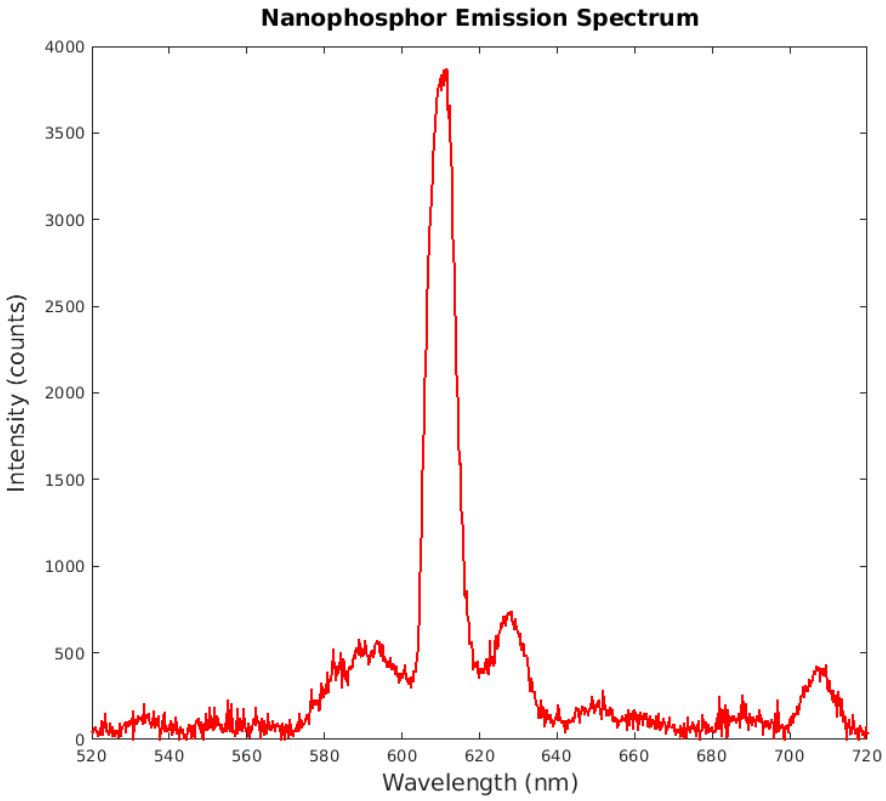

Figure 2.2: Luminescent spectral emission of $Y_2O_3 : Eu^{3+}$ nanoparticles in an aqueous solution when irradiated by an x-ray tube operating at 125 kVp and 23 mA. The primary emission peak of the nanoparticles is centered at 611 nm.

2.4.2 Nanophosphor Concentration Measurements

Next, the relationship between the nanophosphors' concentration and their luminescence was investigated. Various concentrations ranging from 10 mg/mL to 0.05 mg/mL of nanoparticles were dissolved in ethanol. The cuvettes were lined up together within the small animal irradiator with pieces of black paper placed in between the vials to block luminescence from the neighboring cuvettes. Figure 2.3 shows the CCD camera's field of view for the vials containing the concentrations of 0.5 mg/mL, 0.1 mg/mL, and 0.05 mg/mL of nanophosphors along with a cuvette of pure ethanol as control. The nanophosphors were irradiated for 20 s with unfiltered x-rays with a tube voltage of 70 kVp and a tube current of 20 mA. Four image exposures were acquired for each set of concentrations, with a sample image of the x-ray induced luminescence shown in Figure 2.4.

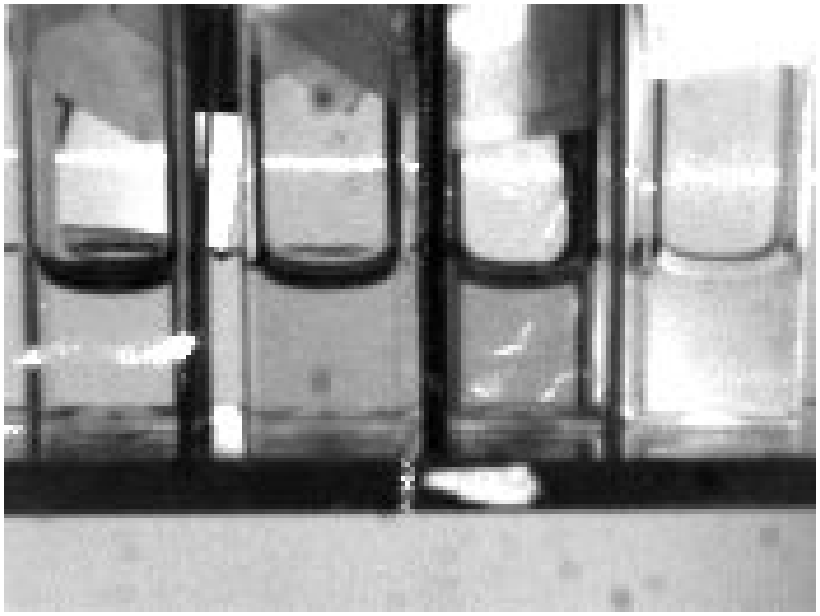

Figure 2.3: Photograph of the cuvettes with nanophosphors solutions used in concentration experiment. From left to right the vials contain pure ethanol (control), 0.05 mg/mL, 0.1 mg/mL, and 0.5 mg/mL of nanoparticles. Pieces of black paper were placed in between the cuvette so that luminescence generated in neighboring vials would not contaminate the measurement of a single cuvette's luminescence. After acquiring the x-ray induced luminescence image, this setup was repeated with the control and the vials containing 1 mg/mL, 5 mg/mL, and 10 mg/mL.

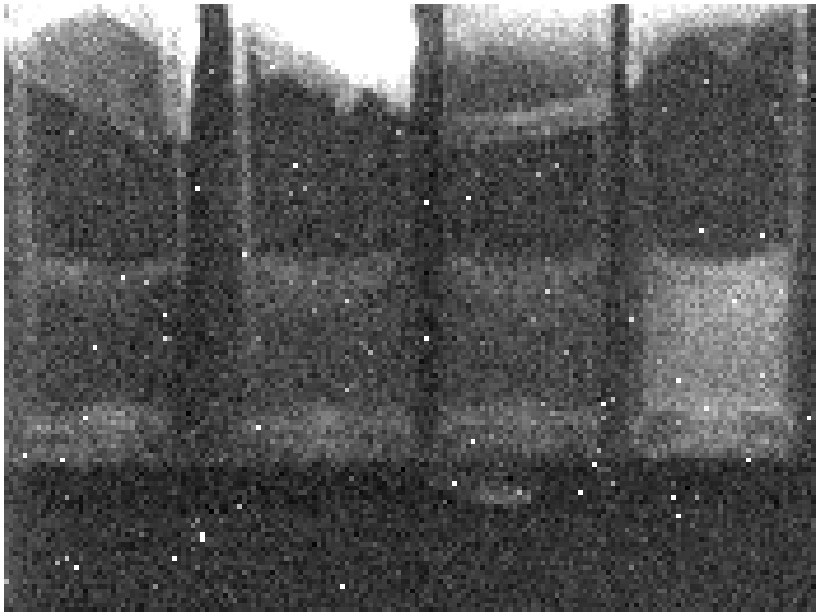

Figure 2.4: The resulting x-ray induced luminescence of the vials with various nanophosphor concentrations imaged above in Figure 2.3. The nanoparticle solutions were exposed for 20 s to an unfiltered x-rays from a tube operating at 70 kVp tube voltage and 20 mA tube current.

The four exposures of the measured luminescence were then averaged in order to reduce noise from scattered x-rays interacting with the CCD sensor. An averaged dark image was then subtracted from the averaged luminescence images. The mean of a region of interest (ROI) from an area of uniform luminescence within each cuvette was used to determine the resulting luminescence. The measured luminescence of the cuvettes versus their corresponding nanophosphor concentration are plotted in Figure 2.5. The x-ray induced luminescence exhibited a linear relationship with respect to nanoparticle concentration. This results reflect those reported in the literature for Europium and Terbium-based nanophosphors activated by x-ray radiation [51].

2.4.3 Tube Current and Tube Voltage Measurements

The relationships between radioluminescence and tube current and tube voltage were subsequently explored. Tube current serves as a proxy for radiation dose in these measurements,

assuming charged particle equilibrium within the cuvettes during the measurements. First, a cuvette containing 5 mg/mL of nanophosphors dissolved in ethanol was irradiated for 20 s with a set tube voltage of 100 kVp and tube currents ranging from 1 to 15 mA. Five acquisitions of each tube current were averaged and for noise reduction and an average dark image was subtracted. Luminescence was measured using the average pixel value of a 15 by 15 pixel region of interest of uniform luminescence within the cuvette. This process then was repeated for varying tube voltages ranges from 40 to 225 kVp and a fixed tube current of 13 mA. Again, luminescence was measured as the average pixel value of a region of interest after the average dark image was subtracted.

The radioluminescence versus tube current is plotted in Figure 2.6 and the relationship is linear. This implies a linear relationship between luminescent output and radiation dose, which has been reported previous in the literature [51]. The x-ray induced luminescence versus tube voltage is plotted in Figure 2.7. Here the nanophosphors exhibited a quadratic relationship with respect to the small animal irradiator's tube voltage. This is likely due to the fact that the photon flux of the x-ray tube increases quadratically with respect to the tube voltage. As tube voltage continues to increase, the incoming x-rays would have high enough energy that most would pass through the cuvette without interaction and the luminescence would no longer necessarily increase with respect to tube voltage. However this effect was not observed within the limits of the small animal iradiator's x-ray tube output.

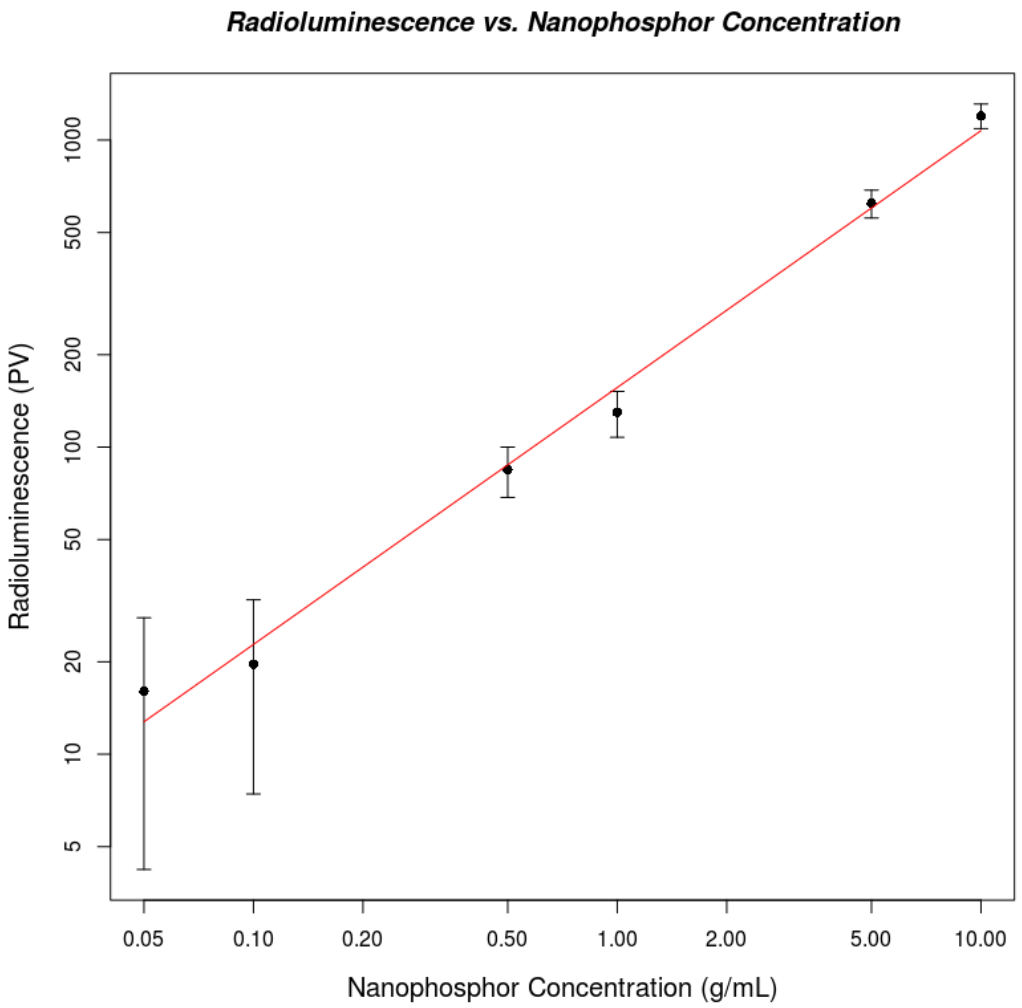

Figure 2.5: X-ray induced luminescence exhibits a linear relationship with respect to nanophosphor concentration. The cuvettes with varying concentrations were irradiated for 20 s with a tube voltage of 70 kVp and a tube current of 20 mA. The error bars represent the standard deviation of the pixel values measured in the ROIs.

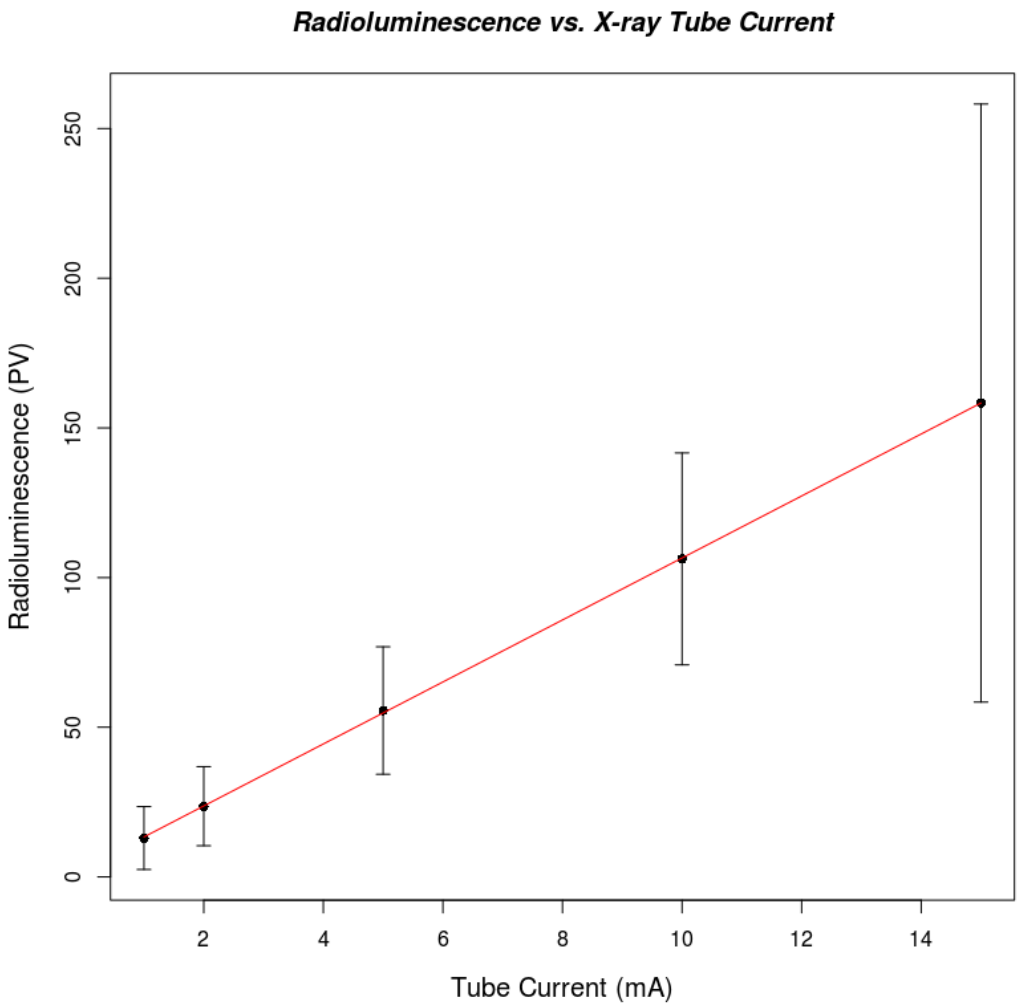

Figure 2.6: X-ray induced luminescence has a linear relationship with respect to tube current. A 5 mg/mL solution of nanophosphors was exposed for 20 s with a fixed tube voltage of 100 kVp. Tube current serves a proxy for x-ray dose in this experiment. The error bars represent the standard deviation of the pixel values measured in the ROIs.

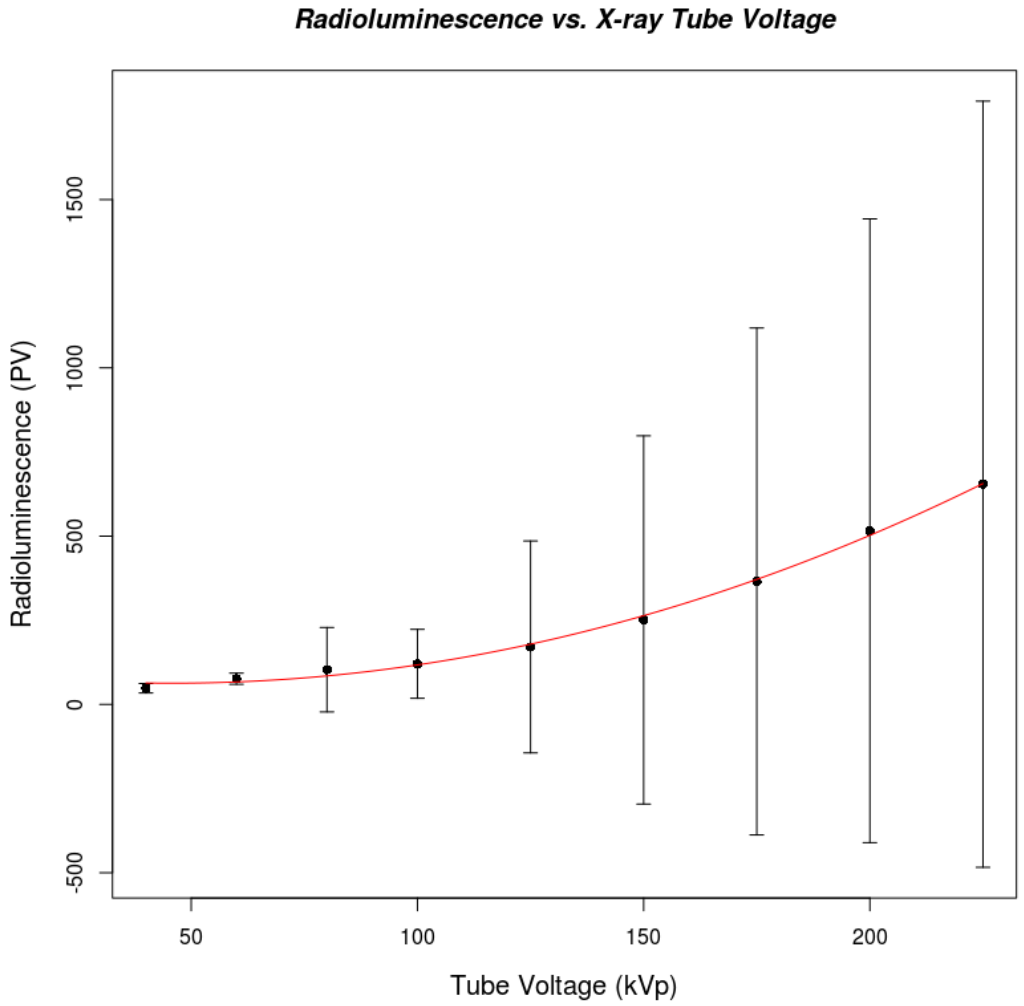

Figure 2.7: X-ray induced luminescence increases quadratically with respect to x-ray tube voltage. A 5 mg/mL solution of nanophosphors was exposed for 20 s with a fixed tube current of 13 mA. The error bars represent the standard deviation of the pixel values measured in the ROIs.

2.5 Luminescent Efficiency Measurement

2.5.1 Luminescence Efficiency Equation

The brightness of the nanophosphors is an important quality that will determine the potential imaging applications based on the radiation dose limitations. This sections quantifies the luminescent efficiency α_{NP} of the nanoparticles, which is a constant that relates the number of optical photons emitted to the absorbed dose and the concentration of the nanophosphors. The photon density P emitted in a region containing the nanophosphors is defined below in Equation 2.1 and has units photons/cm^3. It is linear with respect to the dose D (keV/g) and the concentration of the nanophosphors C_{NP} (g/mL), as experimental verified in the previous section. The energy deposited in the region of the nanophosphors is determined by multiplying the dose with the density of the region, denoted as tissue here ρ_{tissue} (g/cm^3). This section seeks to calculate the luminescence efficiency ($\frac{\text{photons/keV)}}{\text{g/mL}}$) of the nanophosphors by setting up an imaging experiment that calculates the other factors in Equation 2.1:

$$P = \alpha_{NP} \cdot C_{NP} \cdot D \cdot \rho_{tissue} \ . \tag{2.1}$$

2.5.2 Bioluminescence/Fluorescence Calibration Mouse Phantoms

The x-ray induced luminescence imaging with the cooled CCD camera provides a relative measurement of the optical photons emitted by the nanophosphors. It is able to quantify how bright one set of experimental conditions is compared to another, but it is unable to provide an absolute count of photons emitted. Therefore mouse phantoms used for calibrating bioluminescence and fluorescence imaging systems were employed in order to better quantify the the luminescent properties of the nanoparticles. The bioluminescence mouse phantom (XPM-2, Perkin-Elmer) contains two calibrated LEDs at different depths, which isotropically

emit photons at a known rate. The fluorescence mouse phantom (XFM-2, Perkin-Elmer) contains openings that allow the insertion of a photon source at depths matching those of the LEDs in the bioluminescence phantom. The underside of these phantoms contain a relatively flat surface from which the surface luminescence of the LED or nanophosphor source can be detected with the camera. The absolute value of the LEDs' output can then be compared to the measured relative brightness of the nanophosphors in the corresponding fluorescence mouse phantom, thus allowing for a measured absolute photon count of the nanophosphors output.

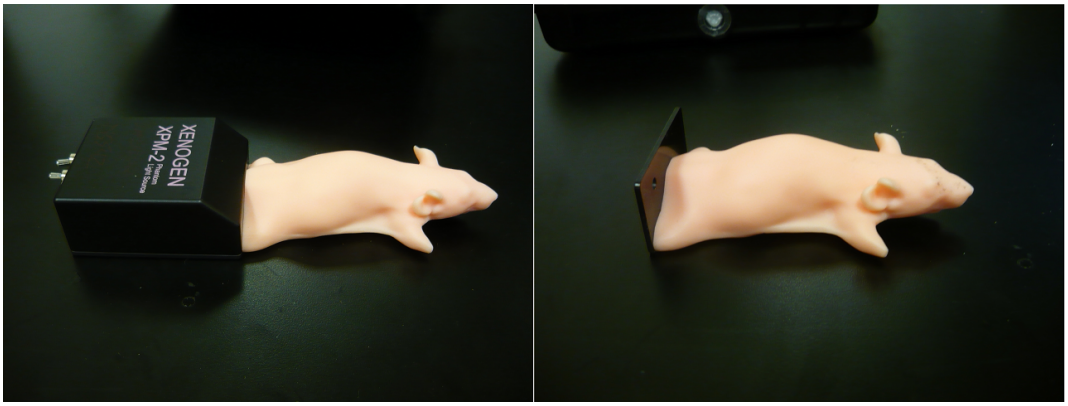

Figure 2.8: XPM-2 bioluminescence mouse phantom (left) and XFM-2 fluorescence mouse phantom (right). The bioluminescence mouse phantom contains calibrated LEDs with a known photon output and the fluorescence mouse phantom allows for the insertion of a radioluminescence point source at a matching depth.

2.5.3 Mouse phantom surface radiance measurements

A glass tube with 10.5 mg of nanophosphors in the tip was inserted into the fluorescent phantom such that it sat approximately 4 mm below the flat underside of the mouse. The mouse was placed on its side on the imaging bed so that the flat surface would face the camera. A CT scan of the mouse phantom containing the nanophosphors was acquired and was used to move the nanophosphor source to the isocenter of the irradiator. The CT image is displayed in Figure 2.9, and the nanoparticles exhibit a strong attenuation of the x-rays

as seen by the streaks and the reconstructed black center of the nanoparticle source. This CT scan was then used to determine the concentration of the nanoparticles. The volume occupied by the 10.5 mg of nanophosphors was calculated from the CT scan. Based on this the calculated concentration of the nanoparticles in the source was 1.81 g/mL.

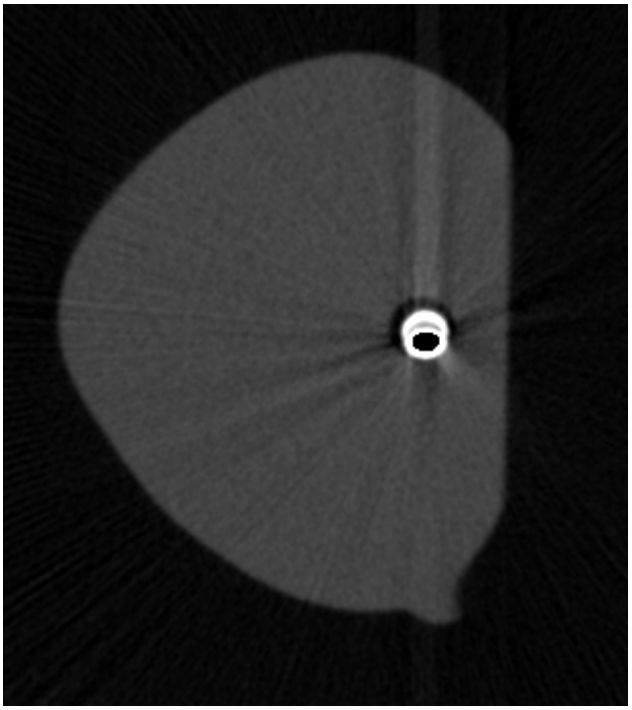

Figure 2.9: CT slice of the nanophosphor source sitting 4 mm below the flat imaging surface on the right side of the mouse phantom. The bone mid gain setting was used for the CT imaging which had a tube voltage was 80 kVp and a tube current of 0.20 mA. The nanoparticles exhibit strong attenuation of the incoming x-rays as seen by the streaks in the image.

The cooled CCD camera and its shielding were then moved into the small animal-irradiator after the fluorescence mouse phantom with the nanophosphor source was moved to the isocenter. A photo of the imaging setup is shown in Figure 2.10. The mouse phantom was irradiated for 20 s with a tube voltage of 70 kVp, a tube current of 40 mA, and a 2.8 mm aluminum filter. Eight images were acquired of the surface radiance for these exposure settings. The average of these eight exposures after subtraction of the dark image is depicted on the right in Figure 2.11.

Then the bioluminescence mouse was placed in the small animal irradiator and a CT scan was used to move the LED to the irradiator's isocenter. Eight images of surface radiance from the calibrated LED were acquired with a 20 s exposure. The average of these images with the dark image subtracted is shown on the left in Figure 2.11. Note the great reduction in spurious counts in the image due to the absence of x-rays.

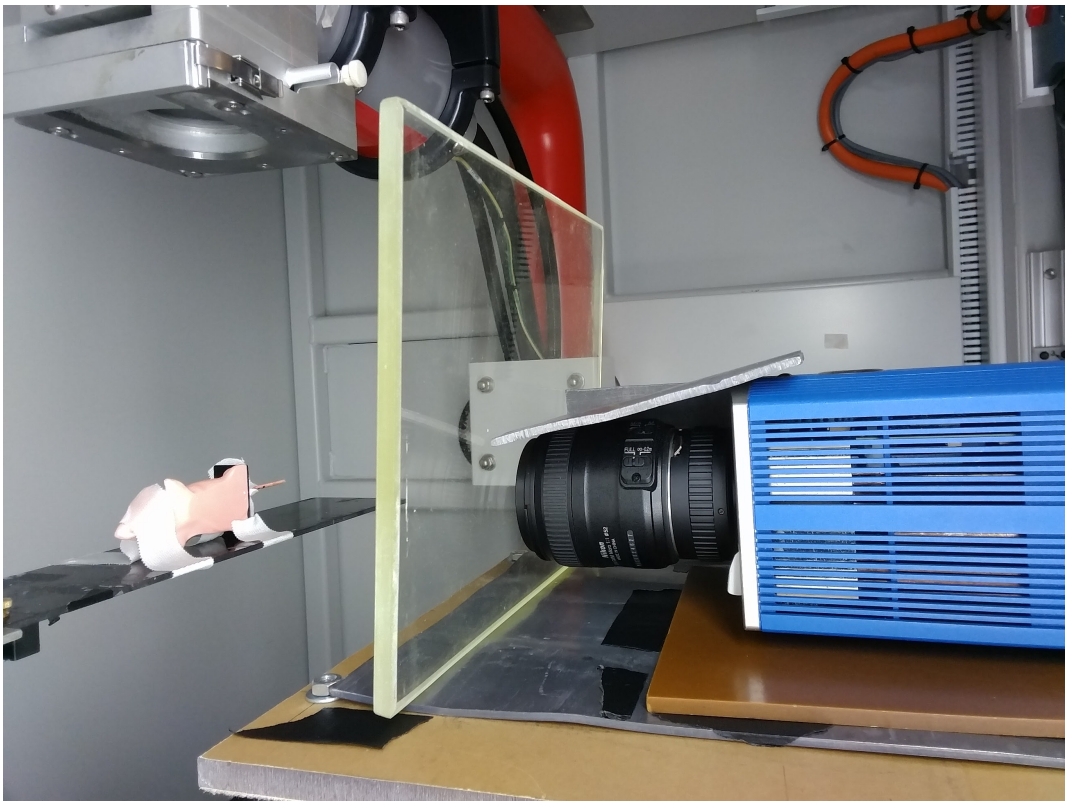

Figure 2.10: Fluorescence mouse phantom with 10.5 mg of nanoparticles inserted via glass tube. The nanophosphor source sits at the isocenter of the irradiator and 4 mm below the flat side of the mouse phantom, which faces the shielded cooled CCD camera.

2.5.4 Small Animal Irradiator Dosimetry

The final measurement necessary to calculate the luminescent efficiency is the dose to the nanophosphors. The first step in determining the nanoparticle dose was measuring the surface dose of the 20 s exposure with the 70 kVp tube voltage, 40 mA tube current, and

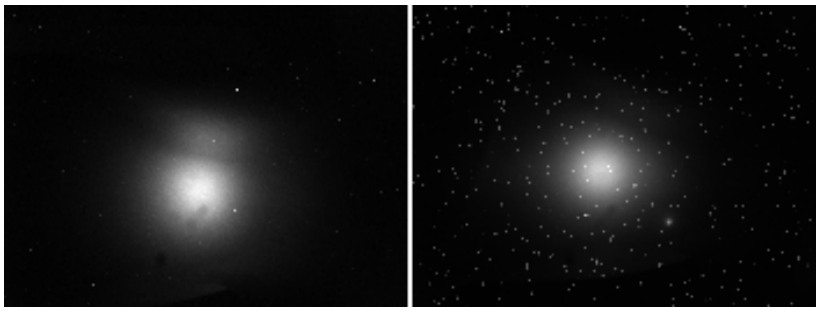

Figure 2.11: Surface radiance measurement of the bioluminescence mouse phantom with calibrated LED 4 mm below the imaging surface (left). Surface radiance measurement of the fluorescence mouse phantom with the 10.5 mg nanophosphor source 4 mm below the imaging surface (right).

a 2.8 mm aluminum filter. An A-12 ionization was placed on top of 10 cm of solid water and surrounded with water equivalent gel pads as shown in Figure 2.12. The chamber was moved to the isocenter of the irradiator and exposed to the experimental tube settings. The collected charge measurements were averaged and then electrometer, recombination, polarity, and temperature-pressure correction factors were applied. The corrected charge reading was then used in a protocol for kilovoltage x-ray dosimetry [52]. The resulting measured surface dose was 95.3 ± 2.2 cGy.

An x-ray spectrum simulator (Siemens Healthcare GmbH) was then used to determine the mean x-ray energy at the depth of the nanophosphors in the mouse phantoms. The x-rays impinging on the mouse phantom from above traveled a distance of approximately 1.27 cm in the plastic mouse phantom, as measured from the CT images. The simulator modeled the 2.8 mm aluminum filter and x-rays path through the mouse phantom, and calculated an average x-ray energy of 43.4 keV with an air kerma transmission factor of 0.639. Using the air kerma transmission factor and surface dose measurement, the dose to the mouse phantom in the region of the nanophosphors was $3.80 \pm 0.09 \times 10^{12}$ keV/g.

The nanoparticles themselves are composed of high-Z elements like yttrium and europium, so the absorbed dose would be increased compared to the surrounding plastic mouse. A dose correction was then applied using the ratio of the mass-energy absorption coefficients.

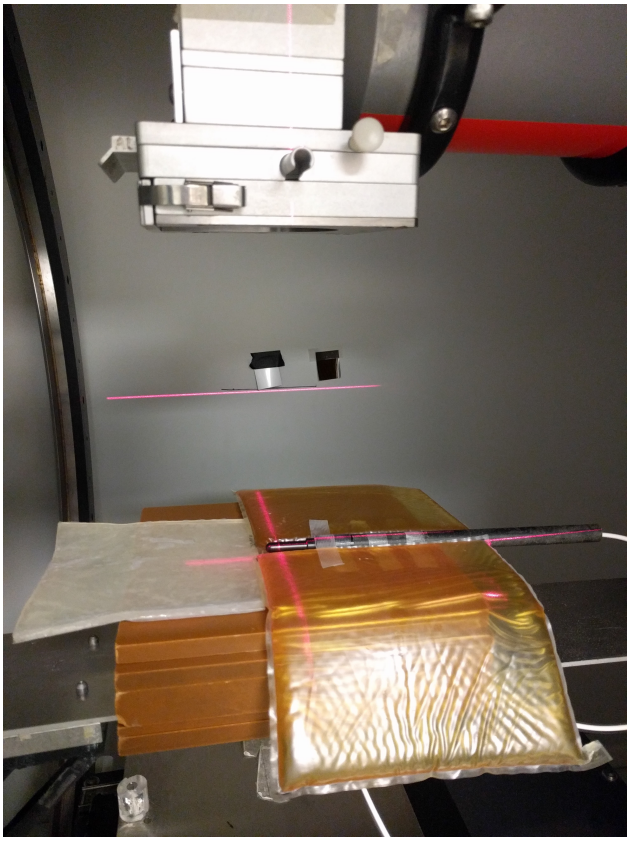

Figure 2.12: A-12 ionization placement for dosimetry measurement. The chamber sits upon 10 cm of solid water with water equivalent gel pads surrounding the tip. It was exposed for 20 s to an x-ray tube voltage of 70 kVp, a tube current of 40 mA, and 2.8 mm of aluminum filtration.

The effective atomic number of the yttrium oxide nanocrystals doped with europium was approximately 38. The ratio of the mass-energy absorption coefficients for the nanoparticles compared to the plastic mouse phantom was 112. Therefore the dose to the nanophosphors inside the fluorescence mouse phantom during the x-ray induced luminescence imaging was $4.24 \pm 0.10 \times 10^{14}$ keV/g.

2.5.5 Luminescent Efficiency Calculation

The calibrated LED in the bioluminescence mouse phantom isotropically emitted photons around 635 nm at a rate of 8.85×10^{10} photons/s. The nanoparticles primarily phosphoresce

611 nm photons. Therefore a correction factor must be applied in order to account for slightly different rates of attenuation and scattering in the optical mouse phantoms. The manufacturer provided a plot for the optical absorption coefficient and reduced scattering coefficients of the mouse phantoms as function of emission wavelength. These parameters were then applied to the normalized surface radiance equation outlined in chapter 3 and a correction factor was determined by comparing the simulated intensities for point sources at 4 mm depth in the mouse phantoms for the two different wavelengths. Line profiles of the measured surface radiances for both sources were compared as shown in Figure 2.13. After comparing the measurements and applying the correction factor for the emission wavelength shift, it was determined the the x-ray induced luminescence measurement was 2.95 times brighter than the calibrated LED. Therefore, over the course of the 20 s exposure, the nanophosphors emitted 5.22×10^{12} photons.

The luminescent efficiency is now calculated by rearranging the terms in the Equation 2.1. The indirect photon count of the nanophosphors using the calibration mouse phantoms is divided by the volume occupied by them on the CT scan, which is 0.0058 cm^3. This is the photon concentration P. This is divided by the concentration of the nanoparticles, the dose D, and the density of the optical mouse phantom. The calculated luminescent efficiency α_{NP} is 1.05 ± 0.03 $\frac{\text{photons/keV}}{\text{g/mL}}$. Previous literature analyzing radioluminescent nanophosphors estimated their efficiency by scaling the bulk scintillating properties by their density [13]. The estimated luminescent efficiency of terbium-based nanophosphors using this method was 8.06 $\frac{\text{photons/keV}}{\text{g/mL}}$. The experimentally measured value is within an order of magnitude of this estimate.

2.6 Optical Gel Phantom Fabrication

The final introductory element to experimental x-ray induced luminescence is the fabrication of optical gel phantoms. Optical imaging in mammalian tissue at depths beyond a millimeter

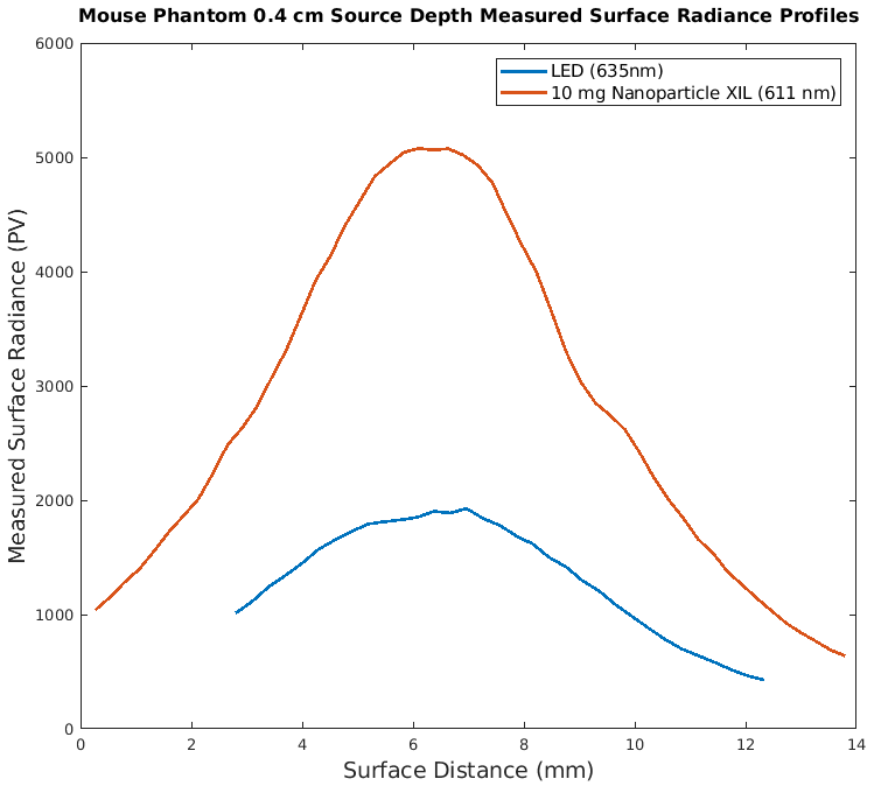

Figure 2.13: Line profiles for the measured surface radiances of the bioluminescence mouse phantom with the calibrated LED and the fluorescence mouse phantom with the nanophosphors.

is best modeled using the equations governing diffuse transport of the light in the media. Such conditions can be simulated in a simplified optically homogeneous diffuse environment by the construction of gel phantoms. These phantoms consist of three basic ingredients: agar, Intralipid, and black ink. The agar creates the gel matrix that holds the other two components. The Intralipid is a fatty solution that effectively scatters optical light and the black ink acts as an absorber. It is possible to create optical gel phantoms with particular absorption coefficients and reduced scattering coefficients based on the the concentrations of the Intralipid and the black ink used [53].

The recipe for the optical phantom is as follows. These concentrations of Intralipid and black ink create a gel phantom with an absorption coefficient of approximately 0.25 cm^{-1}

and a reduced scattering coefficient of 5 cm^{-1}. This is the standard recipe used in all the optical gel phantoms in the various experimental imaging setups.

1. Combine 200 mL of distilled water with 2.02 g of agar powder.
2. Microwave the solution until it reaches a temperature of 95 °C.
3. Transfer to a magnetic stirring plate and begin stirring continuously. Monitor the temperature of the solution as it cools.
4. When the solution reaches 60 °C, add 2.02 mL of Intralipid and 10.1 μL of black ink.
5. Continuing stirring the mixture until it cools to 40 °C.
6. Pour the mixture into the phantom mold and let it set for half an hour.

The finished phantom is a firm gel that will hold its shape. However, the phantom is prone to drying out after long periods. It is best to cover the gel surface with plastic wrap if x-ray induced luminescence measurements will not take place immediately after the phantom has set.

2.7 Discussion

Various x-ray activated nanophosphors have been reported in the literature, but the europium-doped nanoparticles have a particular advantage for imaging in tissue as shown in the spectral measurement. The peak luminescence at 611 nm is on the red end of the optical spectrum, which means the photons are more penetrating and have a greater chance of escaping the tissue for detection. Terbium based nanophosphors, for example, emit green light, which is much more readily attenuated by tissue and would be ill-suited for imaging at depths beyond a few millimeters.

The nanophosphor fabrication outlined in the first section of the chapter is a basic synthesis. Their luminescent output can be further improved by coating the nanocrystals with silica shells. It is theorized that the silica shells create an interface effect with the nanocrystals which cause more of the Europium dopants to be active in the radioluminescence process [7].

The optical gel phantoms with Intralipid and black ink serve as a simple yet versatile tool for studying diffuse light imaging. The desired optical properties of the phantom can be adjusted by the proper selection of Intralipid and black ink concentrations. A wide range of tissues can be modeled with knowledge of the optical properties of the tissues [54]. However, the recipe only produces optically homogeneous phantoms, which is rarely the case for imaging in tissues, but it can serve as a good approximation for exploratory studies.

CHAPTER 3

X-RAY INDUCED LUMINESCENCE IMAGING MODEL AND SENSITIVITY SIMULATIONS

3.1 Diffuse optical imaging equations

Light be can physically modeled in multiple ways depending on its properties and the environment with which it interacts. It can be treated as an electromagnetic wave traversing a medium. It can be modeled as individual ballistic photons, each with a directionality that changes via scattering events. Finally light can be treated as a concentration of optical energy that moves along concentration gradients via diffusion. This last example best models the movement of light in the turbid environment of tissue.

Tissue is composed of cells, extracellular matrices, and extracellular fluid. These components form an admixture comprised mostly of water, fat molecules, and proteins. As photons travels through this biological soup, they encounter a multitude of scatterers and absorbers. Photons that do not get absorbed will undergo many scattering events, such that they lose their original directionality. The collective properties of the photons enter the regime of diffusion once the photons have lost the initial direction they had when emitted from an optical probe in the tissue.

There are four fundamental quantities that describe the optical properties of tissue. The absorption coefficient μ_a describes the likelihood of a photon being absorbed in the tissue per unit length. The scattering coefficient μ_s is the likelihood of a photon being scattered in the tissue per unit length. The direction of the scattering event is characterized by the anisotropy of scattering parameter g, which is dimensionless. It is the average cosine of the scattering angle. In tissue this value is typically around 0.9. Then there is the refractive index n which is approximately 1.4 for tissue and 1.0 for air.

The scattering coefficient μ_s can be thought of as a step size for how far a photon travels

before a scattering event. However, the distance traversed after multiple scattering events from the starting point to the finishing point can be much shorter than the total length of the path the photon traveled. Therefore the reduced scattering coefficient μ_s' more accurately describes the likelihood of a scattering event per unit length traveled in tissue. It is defined in Equation 3.1 and is a function of the scattering coefficient μ_s and the anisotropy of scattering parameter g:

$$\mu_s' = \mu_s(1 - g) \ . \tag{3.1}$$

In order for diffusion theory to apply, the optical photons need to undergo multiple scattering events before absorption. In a strongly attenuating medium, the photons will be absorbed before they lose their directionality, and thus the diffusion equations will not reliably model their movement. A rule of thumb is that the ratio of the reduced scattering coefficient μ_s' to the absorption coefficient μ_a must be 10 or greater for the diffusion approximation to hold [55].

The distance a photon travels before any interaction is the mean free path (*MFP'*) and as shown in Equation 3.2, it is a function of the optical absorption coefficient μ_a and the reduced scattering coefficient μ_s':

$$MFP' = \frac{1}{\mu_a + \mu_s'} \ . \tag{3.2}$$

In tissue the *MFP'* of visible and near-infrared light is approximately 1 to 2 mm or less [55]. After the distance of one *MFP'*, diffusion theory becomes quite accurate. Therefore optical imaging at depths in tissue beyond the superficial layer can be properly modeled with diffusion equations.

Diffusion theory treats the photons in the tissue as a concentration that is proportional to the photon fluence rate ϕ. The photons' movement is then modeled as moving down the concentration gradients from a region with a greater density of optical photons to one with a

lesser density. This movement is defined by Fick's first law of diffusion as shown in Equation 3.3,

$$J = -D\frac{\partial \phi}{\partial x} \ , \tag{3.3}$$

where J is the flux of the photons, and the diffusion coefficient D is defined in Equation 3.4:

$$D = \frac{MFP'}{3} \ . \tag{3.4}$$

The solution for the photon fluence ϕ at radius r from a point source in a homogeneous diffuse medium is shown in Equation 3.5:

$$\phi(r) = \frac{P}{4\pi D r} e^{-\mu_{eff} r} \ . \tag{3.5}$$

The power P of the point source decays exponentially at the rate of the effective attenuation coefficient μ_{eff}, which is defined in Equation 3.6:

$$\mu_{eff} = \sqrt{3\mu_a(\mu_s' + \mu_a)} \ . \tag{3.6}$$

This is the case for continuous waves, implying there is no time dependency of the luminescent point source's output. This would be accurate for nanophosphors irradiated with an x-ray tube, which has a relatively continuous output compared to a LINAC, which has time-dependent pulses of radiation.

Optical imaging *in vivo* occurs at the surface of the tissue. The interface between the air and tissue forms a boundary where some of the optical photons will be reflected while others will be transmitted and eligible for detection. The extrapolated boundary condition simplifies the interface to an optically homogeneous medium that has a flat interface with the air and extends to infinity in the other directions. The source sits at depth z below the imaging surface and a negative sink called the image source is placed outside of the tissue, so

as to draw the optical signal towards the surface. The image source is placed in symmetry from the luminescent source inside the tissue across an extrapolated boundary which is an imaginary plane that resides above the true surface of the tissue. This geometry is depicted below in Figure 3.1.

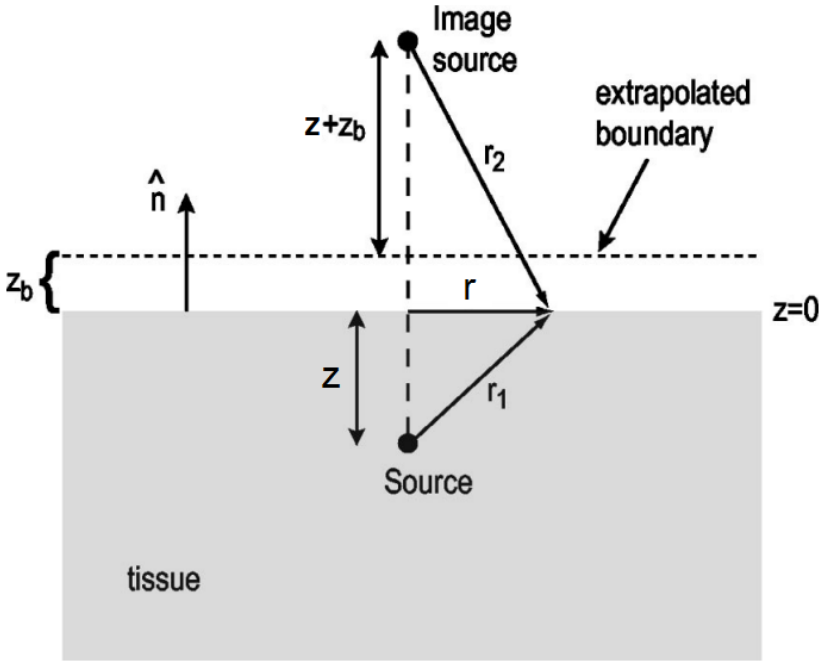

Figure 3.1: Diagram from Rice *et al.* of the luminescent source in tissue at depth z and the image source placed in opposition across the extrapolated boundary z_b [2]. The real air-tissue interface occurs at $z = 0$. The tissue is optically homogeneous and a semi-infinite medium. The radial distance on the tissue surface from the source-image source axis is r, and r_1 and r_2 are the distance from that point to the luminescent source and the image source, respectively.

The placement of the extrapolated boundary z_b is a function of the optical parameters of the tissue for the light and the effective reflectance of the air-tissue interface R_{eff}. It is defined in Equation 3.7:

$$z_b = \frac{1 + R_{eff}}{1 - R_{eff}} \frac{2}{3(\mu_a + \mu_s')} \ . \tag{3.7}$$

The effective reflectance R_{eff} determines how much diffuse light escapes into the air at the interface and how much is reflected back into the tissue. Air has a refractive index

of $n = 1.00$, while tissue has a refractive index of $n = 1.40$. The corresponding effective reflectance is $R_{eff} = 0.493$ [56].

The normalized surface radiance N at radial distance r is the detectable optical signal at the surface of the tissue from the luminescent point source at depth z. It is normalized to the luminescent power emitted by the source and has units $\frac{1}{cm^2 sr}$. It is a combination of the flux and the fluence of the luminescent source and the imaginary image source, and it is defined in Equation 3.8:

$$N(r,z) = \frac{1}{16\pi^2 D}\left\{\frac{e^{-\mu_{eff}r_1}}{r_1} - \frac{e^{-\mu_{eff}r_2}}{r_2} + 3D\left[\frac{z}{r_1^2}\left(\mu_{eff} + \frac{1}{r_1}\right)e^{-\mu_{eff}r_1} + \frac{z+2z_b}{r_2^2} \times\left(\mu_{eff} + \frac{1}{r_2}\right)e^{-\mu_{eff}r_2}\right]\right\}. \tag{3.8}$$

A short derivation is provided by Rice *et al* [2]. This analytical solution to the extrapolated boundary condition will serve as an approximation for the surface radiance in an x-ray induced luminescence imaging model that is then tested with experimental measurements in optical gel phantoms.

3.2 X-ray induced luminescence imaging model

The entire x-ray induced luminescence imaging process draws on multiple fields of physics: the x-ray interaction with the tissue and the resulting radioluminescence, the diffuse optical transport of the luminescent signal in the tissue, and the detection of the surface radiance with a lens and camera. The imaging model breaks it down into stages so that the detected signal across the camera's CCD array can be predicted from the concentration of nanophosphors in tissue at a given depth and radiation dose.

As outlined in Chapter 2, section 2.4, the radioluminescence is proportional to the nanophosphor concentration and radiation dose. The dose can then be related to the energy density deposited in tissue by taking the product of dose and the density of the tissue

ρ_{tissue}. Therefore the concentration of photons generated in a given voxel P_{voxel} is shown in Equation 3.9,

$$P_{voxel} = D_{voxel}\rho_{tissue}C_{NP}\alpha_{NP} \ , \tag{3.9}$$

and it is the product of the dose to the voxel D_{voxel}, the density of the tissue in the voxel ρ_{tissue}, the concentration of the nanophosphors in the voxel C_{NP}, and the luminescent efficiency α_{NP}.

The luminescent photons generated in the tissue at depth z will diffuse outward from the source with some migrating towards the imaging surface. The normalized surface radiance *N(r, z)* describes the resulting luminescent intensity that can be detected with a camera and lens. Figure 3.2 (a) displays the imaging geometry for a luminescent voxel $P(x, y, z)$ being excited by a selective plane of x-rays. The surface radiance function is radially symmetric, where r is the distance from the imaging axis of the luminescent voxel $P(x, y, z)$. The resulting surface radiance $f(x_0, y_0)$ from the voxel $P(x, y, z)$ will be the product of the photon concentration and the normalized surface radiance, where $r = \sqrt{(x_0 - x)^2 + (y_0 - y)^2}$. The total surface radiance will then be integrated over the entire volume so that the surface radiance at point (x_0, y_0) will be the sum of all the resulting surface radiances of all the luminescent voxels in the tissue, as shown in Equation 3.10:

$$f(x_0, y_0) = \iiint P(x, y, z)N\big(\sqrt{(x_0 - x)^2 + (y_0 - y)^2}, z\big) \ \ dxdydz \ . \tag{3.10}$$

The final step in the model is detecting the surface radiance with the lens and camera pixel array. Equation 3.11 defines the average photons incident on pixel j in the CCD array located at x_j, y_j:

$$\overline{g}_j = \frac{\pi}{4}\frac{1}{(1 + |m|)^2 N^2} cos^4(\theta_j) m^2 \iint f(x_0, y_0) rect\Big(\frac{x_0 - x_j}{\varepsilon/m}\Big) rect\Big(\frac{y_0 - y_j}{\varepsilon/m}\Big) \ . \tag{3.11}$$

The equation is adapted from one derived by Barrett and Myers[57]. The double integral

accounts for averaging of the surface radiance over camera pixels of size ε, mapped into object space by the lens magnification factor m. The terms before the integral represent the fractional solid angle subtended by the lens. Here N represents the lens f-number and θ_j is the angle of pixel j off the central imaging axis. A factor of $\frac{\pi}{4}$ is included because the luminescence emitted at the phantoms open face is Lambertian. Figure 3.2 (b) depicts the image geometry where the lens projects the surface radiance $f(x_0, y_0)$ onto pixel j.

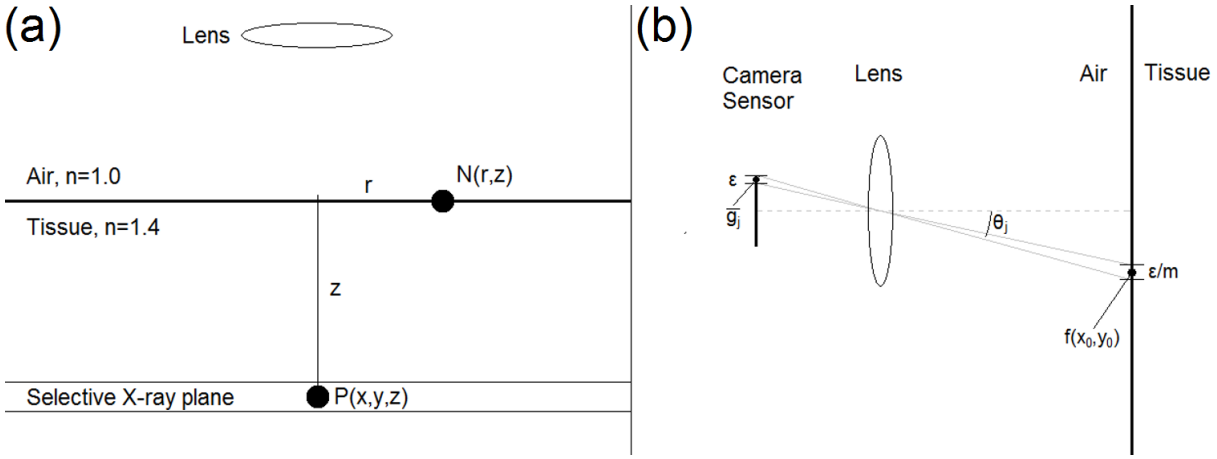

Figure 3.2: (a) Schematic showing x-ray induced luminescence *P(x,y,z)* at depth z via the selective plane excitation and the normalized surface radiance at point *N(r,z)* from a the luminescent point source in the tissue. (b) Detection of the surface radiance with CCD array via lens with f-number N and magnification m.

3.3 Thermoluminescence diode dosimetry in optical gel phantom

In order to model experimental x-ray induced luminescence imaging inside an optical gel phantom, it is important have proper dosimetry. Thermoluminescent diodes (TLDs) were selected for dosimetry measurements due to their ease of use for embedding in an optical gel phantom. The agar gel phantom is mostly water, so the water-equivalent property of the TLDs ensure there is no perturbation in the dose measurement by placing the dosimeters *in situ*.

A set of 40 TLDs was irradiated using the small animal therapy unit for 4 s with a tube

voltage of 70 kVp and a tube current of 20 mA. They were left to stabilize overnight and then their accumulated charge was measured with a TLD reader (Harshaw 5500). The set of TLDs was then then annealed at 400 °C for 1 hour and 80 °C for 24 hours to reset the TLDs; this process was repeated two more times. The resulting TLD readings were used to calculate the batch sensitivities of the TLDs along with their uncertainty.

Next a beam-quality conversion factor was calculated in order to compare the TLD readings from the small animal irradiator to TLD readings for a known calibrated output dose from a LINAC. A total of 4 TLDs received 4.25 cGy of radiation from a 6 MV LINAC beam by placing them at 10 cm depth in solid water and irradiating them with 5 MU at 90 cm SSD with a field size of 10 cm $\times$ 10 cm. The TLDs were then processed with the TLD reader and their readings were corrected with their previously calculated sensitivities. Dosimetry using an A-12 ionization chamber had already been performed in the small animal irradiator as outlined in Chapter 2, section 2.5.4. The measurement exposed the ionization chamber for 20 s with a 70 kVp tube voltage, 40 mA of tube current, and 2.8 mm of aluminum beam filtration. This experimental setup was repeated with 4 TLDs, including 10 cm of solid water beneath the TLDs for backscatter. The readings from the TLDs in the small animal irradiator and the measured ionization chamber dose of 95.3 cGy were compared with the TLD readings and dose from the 6 MV LINAC. It was determined the TLDs were 40% more sensitive to the lower-energy small animal irradiator.

The final measurement for dosimetry required embedding the TLDs inside the optical gel phantom. The TLDs were heat-sealed in plastic warp and placed in the center of a phantom mold using thin plastic sticks. A photo of the TLDs positioning before the liquid gel mixture was poured is shown in Figure 3.3. The phantom was then placed inside the small animal irradiator at isocenter and irradiated for 20 s with a tube voltage of 70 kVp and a tube current of 40 mA, as shown in Figure 3.4.

The TLDs were then removed from the gel phantom and the plastic wrap and their

Figure 3.3: Gel phantom mold with TLDs labeled and positioned along the central axis. TLDs were heat sealed in plastic wrap to protect them from liquid agar gel that was subsequently poured into the mold.

readings were recorded. The dosimetry was then calculated using Equation 3.12:

$$D_{phan} = (\overline{r \times S}) \times k_{cal}^{wat} \times \left(\frac{\mu_{en}}{\rho}\right)_{water}^{phan} \times k_{SAI} \ . \tag{3.12}$$

The first term is the average of the embedded TLD readings r corrected with their respective sensitivities S. The second term k_{cal}^{wat} is the ratio between the 4.25 cGy calibrated dose using the LINAC and the corresponding reading. The ratio between the mass-energy absorption coefficients of the phantom and water is 1, because the gel phantom is water equivalent. Finally the last term k_{SAI} is the beam-quality conversion factor that converts from the LINAC 6 MV x-rays to the small animal irradiator's x-ray tube output. TLD dosimetry measurements in a gel phantom determined the dose to be 33.8 $\pm$ 1.4 cGy at the

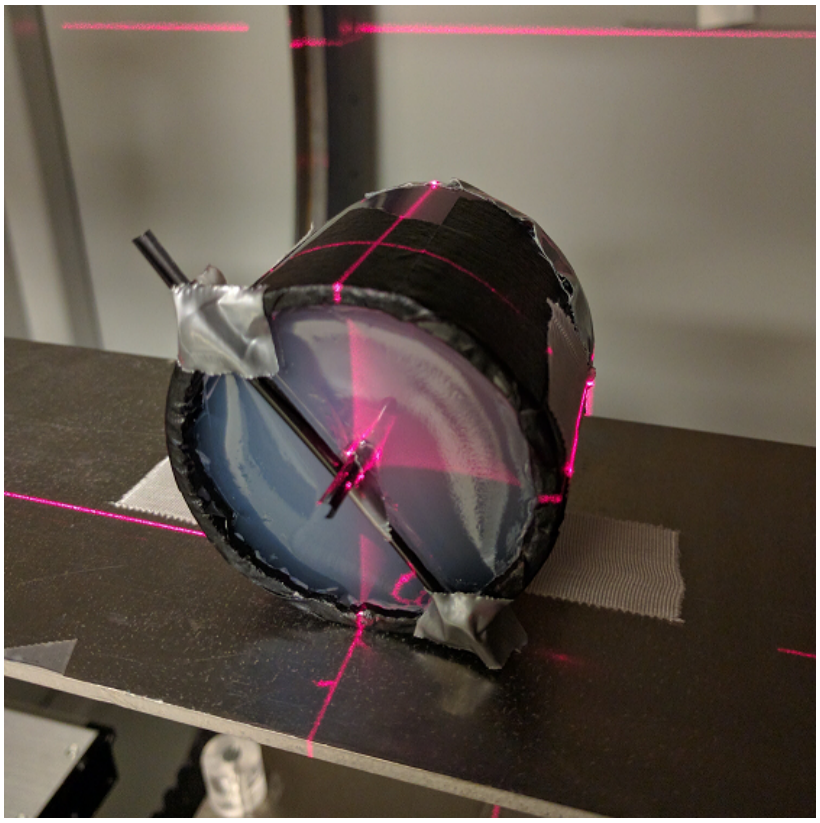

Figure 3.4: Set gel phantom containing embedded TLDs located at the isocenter of the small animal irradiator. The phantom was irradiated for 20 s with a tube voltage of 70 kVp and a tube current of 40 mA in order to match conditions for x-ray luminescence imaging with nanophosphors in a similar optical gel phantom.

central axis of the phantom for a 20 s exposure with a tube voltage of 70 kVp and tube current of 40 mA while using 2.8 mm of aluminum filtration.

3.4 X-ray induced luminescence model calibration with measurements

The image model presented in section 2 was then tested with experimental measurements using optical gel phantoms. Optical gel phantoms were fabricated and a nanophosphor source was inserted at various depths. The calculated luminescent efficiency α_{NP} from chapter 2 and the dosimetry measurement from the previous section were used to determine the number

of photons generated within the gel phantom. Then the normalized surface radiance function from section 2 was applied. The calculated detected luminescence was then compared to the experimental results in order calibrate the model for simulations in the following section.

A 10.5 mg nanophosphor source was inserted into an optical gel phantom and CT scan measurements determined the depths to be 1.6 cm, 2.2 cm, and 2.6 cm as shown in Fig. 3.5 (a), (b), and (c). The phantom was irradiated for 20 s with a tube voltage of 70 kVp and a tube current of 40 mA. The x-ray induced luminescence surface radiance measurements for the corresponding three depths are shown in Figure 3.6. These images represent the mean of eight different x-ray induced luminescence images with the dark image subtracted. This averaging was done in order to reduce noise and outliers from spurious counts caused by scattered x-rays. TLD dosimetry measurements in a gel phantom determined the dose to the gel phantom in the region of the nanophosphors to be 33.8 cGy as outlined in the previous section.

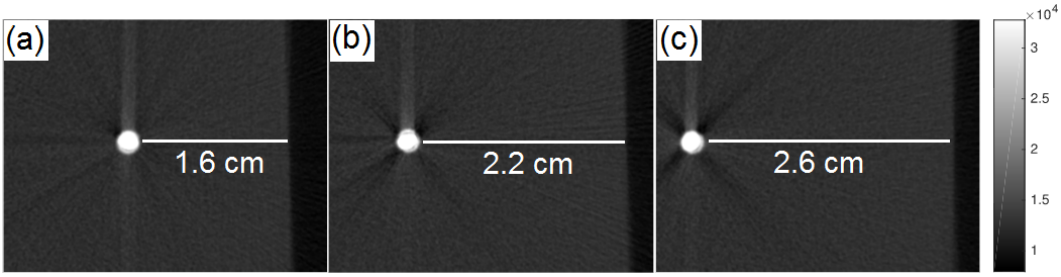

Figure 3.5: CT slices of the 10.5 mg nanophosphor source in the optical gel phantom. X-ray induced luminescence surface radiance images were acquired with the source at the depths of 1.6 cm (a), 2.2 cm (b), and 2.6 cm (c) below the imaging surface.

The x-ray induced luminescence model was used to generate surface radiance profiles based on the optical properties of the gel phantom along with the experimental CCD camera and lens specifications. The specifications for the experimental setup are listed in the first column of Table 3.2. The simulation was then scaled with a calibration factor to account for light loss in the lens and leaded glass along with other unknown instrumental factors. Note that Rice *et al.* also implicitly renormalized the surface radiance curves in a similar fashion

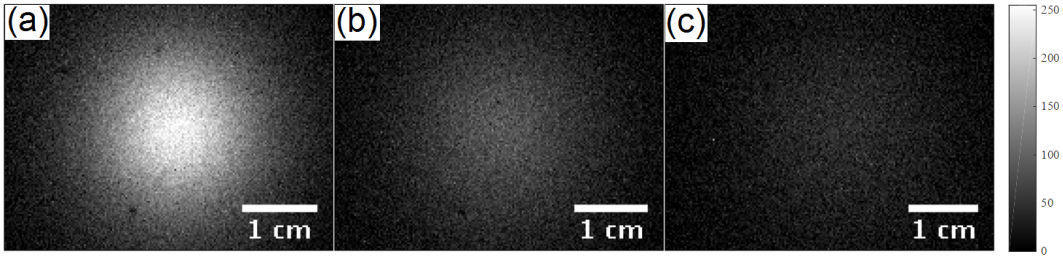

Figure 3.6: X-ray induced luminescence surface radiance images were acquired with the source at the depths of 1.6 cm (a), 2.2 cm (b), and 2.6 cm (c) below the imaging surface. The dark spots in the x-ray induced luminescence measurement were caused by dust on the cameras imaging window.

in their study of bioluminescence sensitivity[2]. Rather than introducing a depth-dependent calibration factor in the detection sensitivity estimates, we scaled the model so that the surface radiance peak value for the 2.2 cm depth source simulation matched the peak height for the x-ray induced luminescence measurement. This leads to an overestimate of the signal ($\sim$60%) of the signal at 1.6 cm and an underestimate ($\sim$40%) of the signal at 2.6 cm depth. Since our interest is in determining the imaging depth limits, this scaling ensures that the predictions will be somewhat conservative at greater depths. The scaling factors for the different depths are listed below in Table 3.1, and the line profiles for the scaled simulated detected surface radiances and experimental measurements are plotted in Figure 3.7. While the normalized surface radiance did not completely capture the depth-dependent scaling, it did accurately predict the spread of the line profile at the different depths.

Source depth (cm)	Scaling factor
1.6	170
2.2	105
2.6	64.4

Table 3.1: Depth-dependent scaling factor used in Figure 3.7 in order to match the simulated surface radiance height with the measured surface radiance. The simulated surface radiances overestimated the measured pixel values for each depth. Therefore, the simulated surface radiances were divided by the scaling factors

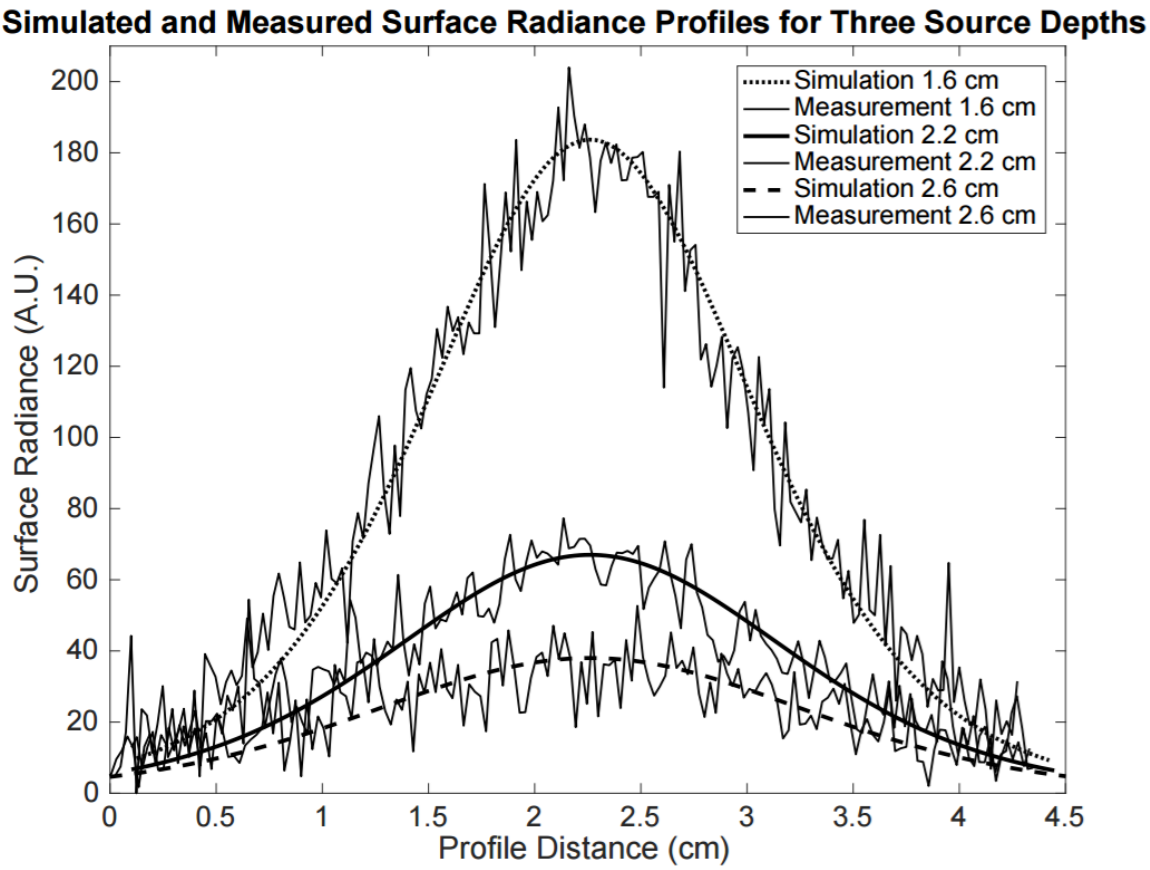

Figure 3.7: Experimental x-ray induced luminescence surface radiance profiles of the optical gel phantom with the corresponding simulated profiles for a point source at the depths of 1.6 cm, 2.2 cm, and 2.6 cm. Each simulated surface radiance profile is individually scaled to the approximate peak of the corresponding measurement. The analytical optical diffusion model accurately predicts the FWHMs of the surface radiance profile measurements.

3.5 Sensitivity simulations

The x-ray induced luminescence images acquired with the 10.5 mg nanophosphor source and diffuse optical gel phantoms were used to calibrate the imaging model outlined in section 2. The calibrated model was then used to produce simulated x-ray induced luminescence images for nanophosphor sources with varying concentrations, depths, radiation doses, and optical environments. The x-ray induced luminescence images were simulated for the experimental setup with the cooled CCD and macro lens, and for a theoretical improved configuration using

an EMCCD (iXon 897, Andor, Concord, MA, USA), larger aperture lens (EF 50 mm f/1.0 USM, Canon, Melville, NY, USA), and nanophosphors with a greater luminescent efficiency shown in Table 3.2. The luminescent efficiency assumed for the brighter nanophosphors is based on the paper of Pratx *et al.*, [13] where the efficiency was calculated from the properties of bulk Gd_2O_2S:Tb [3]. The simulations determined the photon counts on the cameras sensor arrays and this was used to then calculate signal-to-noise ratios for the simulated concentration, optical, dose, and depth parameters using Equation 3.13:

$$\left(\frac{S}{N}\right)^2 = \sum \frac{(D_{QE}\overline{g_j})^2}{F^2(D_{QE}\overline{g_j} + \delta^2_{dark}t) + \frac{\delta^2_{readout}}{M^2}} \ . \tag{3.13}$$

The noise factor F accounts for counting noise amplification in the EMCCD and t is the exposure time in the image acquisitions.

Imaging System Parameters	Cooled CCD with f/2.8 lens	EMCCD with f/1.0 lens
f-number, N	2.8	1.0
Quantum efficiency, D_{QE}	60%	95%
Pixel size, ε	6.45 μm	13 μm
Imaging array size	1392 × 1040	512 × 512
Pixel binning	8 × 8	4 × 4
Dark current, δ_{dark}	0.001 e-/pixel/s	0.00015 e-/pixel/s
Read noise, $\delta_{readout}$	4.5 e- rms	15 e- rms
G, M	1	1000
Noise factor, F	1	1.41
Luminescent efficiency, α_{NP}	1.06 photons/keV/(g/cm^3)	8.06 photons/keV/(g/cm^3)

Table 3.2: CCD and EMCCD camera parameters used to calculate the signal-to-noise ratios in simulated x-ray induced luminescence images. The cooled CCD camera with f/2.8 lens was used in experimental measurements with optical gel phantoms and the EM-CCD camera with f/1.0 lens was used to delineate the upper limits of x-ray induced luminescence imaging sensitivity by simulating optimal hardware

The calibrated simulation was then used to generate surface radiance measurements for varying depths, concentrations, radiation doses, and imaging environments using both the experimental CCD camera and lens setup along with the theoretical configuration with

improved detection hardware as listed in Table 3.2. The corresponding signal-to-noise ratios (SNRs) were calculated using Equation 3.13, the simulated incident photon count on each pixel, and camera sensor specifications. The minimum detectable signal was set at a SNR threshold of five.

Figure 3.8 displays the SNR curves for nanophosphor concentration versus depth using the experimental radiation dose of 33.8 cGy and the optical properties of the experimental gel phantom. The simulated theoretical configurations are split into a setup with improved detection hardware with the experimental nanophosphors and a setup utilizing improved hardware and brighter nanophosphors. The theoretical setup with more sensitive equipment and brighter nanoparticles decreases the minimum concentration for detection by approximately three orders of magnitude compared to the experimental setup with the existing synthesized nanoparticles.

Figure 3.9 depicts the SNR curves for radiation dose versus the depth of a nanophosphor point source with a concentration of 1 mg/mL. The theoretical configuration in the dose versus depth simulation employs improved detection hardware and brighter nanophosphors. Both the experimental and theoretical setup curves show the minimum detectable dose for the optical properties of the experimental gel phantom ($\mu_a = 0.25$ cm^{-1}, $\mu_s' = 5$ cm^{-1}), and a phantom that absorbs and scatters more light ($\mu_a = 0.5$ cm^{-1}, $\mu_s' = 10$ cm^{-1}).

3.6 Discussion

The dose versus depth sensitivity simulation predicted that, with an optimized geometry, improved hardware, and brighter nanoparticles, a concentration of 1 mg/mL could be detected with a dose of about 1 cGy at a depth from 2 to 4 cm depending on the tissue optical properties. The experimental and simulated gel phantoms used in this sensitivity evaluation do not represent a specific tissue, but rather demonstrate diffuse imaging in a turbid material with optical properties within the range of biological tissue[54]. The simulation with the

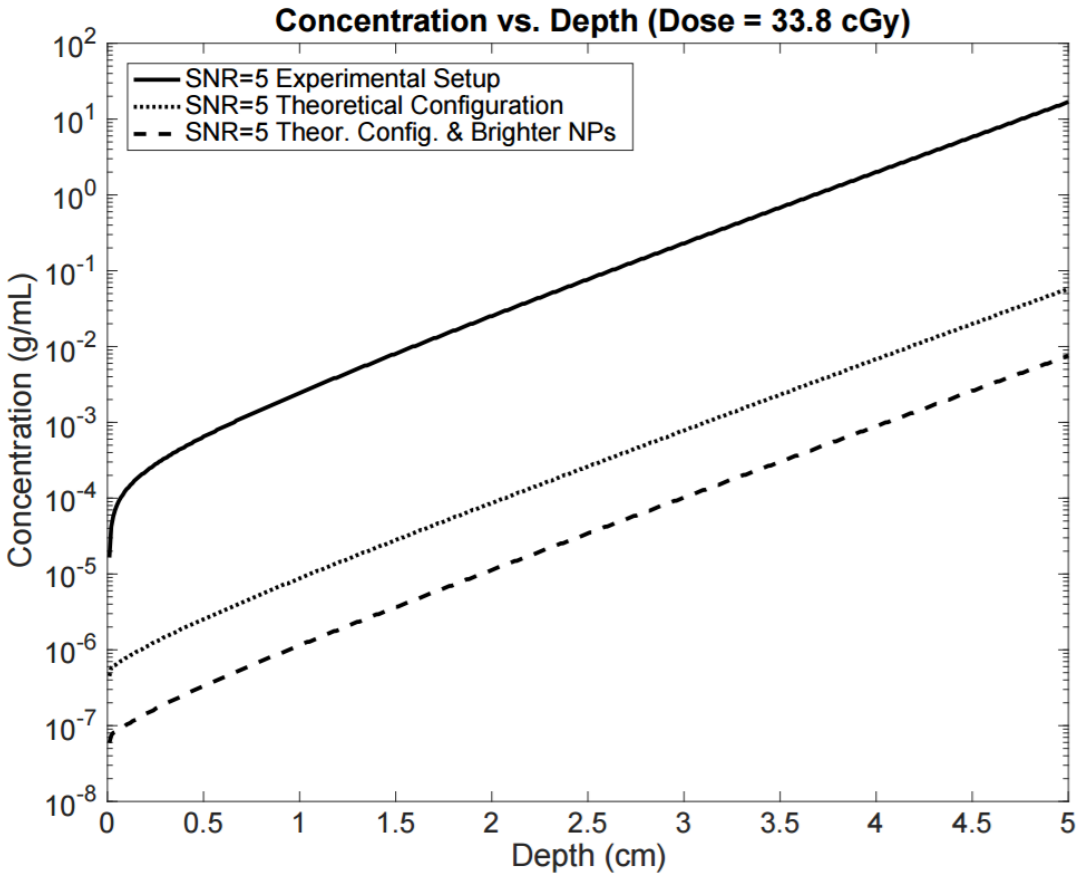

Figure 3.8: Minimum detectable concentration versus depth of nanoparticles for the experimental setup, a theoretical setup using a f/1.0 lens and an EM-CCD camera, and a theoretical setup with the f/1.0 lens, EM-CCD camera, and brighter nanophosphors

current experimental hardware and nanophosphors indicates a minimum dose of 106 cGy to achieve signal detection at comparable depths for a concentration of 1 mg/mL. Therefore a setup comparable to the theoretical configuration with a high degree of sensitivity is required in order to carry out x-ray induced luminescence imaging using clinically relevant radiation doses and nanophosphor concentrations.

Potential applications under such conditions could include intratumoral injections to treat relatively superficial head and neck cancers. Similar concentrations of metal-oxide framework nanoparticles studied as photodynamic therapy light sources have been tested

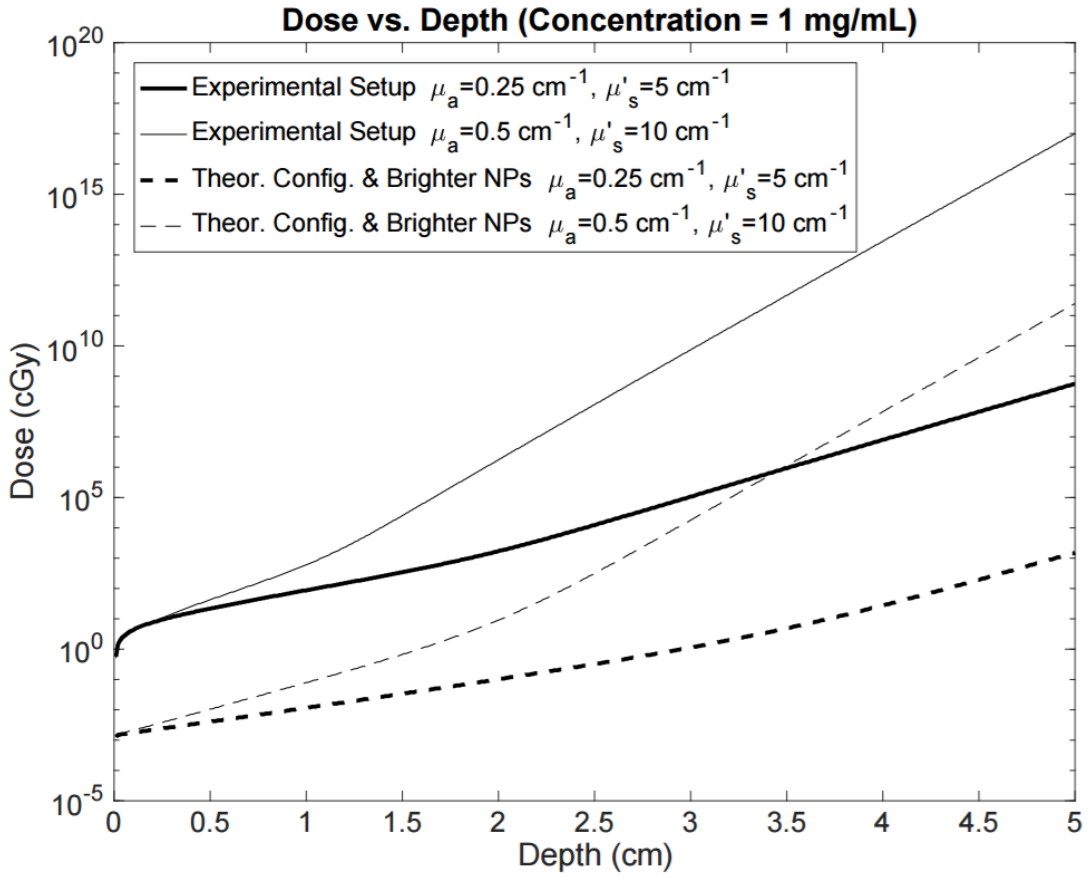

Figure 3.9: Minimum radiation dose for signal detection versus depth for a 1 mg/mL point source for the experimental setup and the theoretical configuration with more sensitive equipment and brighter nanophosphors. Each setup includes curves for the optical properties of the experimental gel phantom and for a greater optically scattering and absorbing environment.

in vivo using a murine model in order to develop a therapy for resistant head and neck cancers[58]. These nanoparticles also exhibit radioluminescence, [45] so that their localization could be roughly determined from surface radiance measurements for a radiation-activated photodynamic therapy treatment. Such imaging could potentially be achieved under normal light conditions in the clinic since Cherenkov luminescence has been detected under ambient lighting by timing the camera acquisitions with the LINAC waveform pulses [59].

The results presented here focused on optically homogeneous materials, which allowed

rapid, tractable sensitivity calculations. Expanding the studies to optically heterogeneous materials would affect our sensitivity simulations and complicate the optical diffuse transport modeling. Another limitation of this work is the assumption of a flat imaging surface. Surface radiance measurements in small animals or patients would rarely involve a relatively smooth, flat surface. Along with being optically heterogeneous, the imaging surface would contain some curvature which would affect the resulting surface radiance measurement. There is no simple analytical solution for diffuse optical imaging moving away from the semi-infinite air-tissue interface with no curvature. Monte Carlo simulations have been used to model the effect of curvature on Cherenkov luminescence at the imaging surface [60]. This modeling could be extended to x-ray induced luminescence imaging in order to account for non-flat surfaces.

CHAPTER 4

SELECTIVE PLANE X-RAY INDUCED LUMINESCENCE IMAGING

4.1 Selective Plane Imaging Geometry

The previous chapter dealt with x-ray induced luminescence imaging where the entire object was irradiated with x-rays. The point sources were at a known depth, but without that information it would have been impossible to deduce their distribution from the measured surface radiances. This ill-posed problem is solved by the introduction of a sheet-beam illumination. Selective plane x-ray induced luminescence imaging is depicted in Figure 4.1. Slit collimation of the x-ray source produces planar x-rays that selectively excite the nanophosphors within the object. Orthonormal to the sheet beam is the camera imaging axis, which captures the surface radiance resulting from the radioluminescence in the illumination plane. The imaging geometry is inspired by selective plane illumination microscopy (SPIM), which allows for fluorescent microscopic imaging and optical sectioning within objects the size of a few millimeters [61]. As discussed later in the chapter, the selective plane geometry allows for a deconvolution-based reconstruction. This approach has been demonstrated experimentally using fluorophores activated by Cerenkov radiation [62] induced by a selective plane geometry.

4.2 Two-Dimensional Convolution Imaging Model

The selective-plane geometry constrains the luminescence within the object by one dimension, creating a reconstruction with only two degrees of freedom. X-ray induced luminescence imaging detects a two-dimensional surface radiance. Therefore the reconstruction is much less ill-posed provided the object is optically homogeneous. An imaging geometry wherein

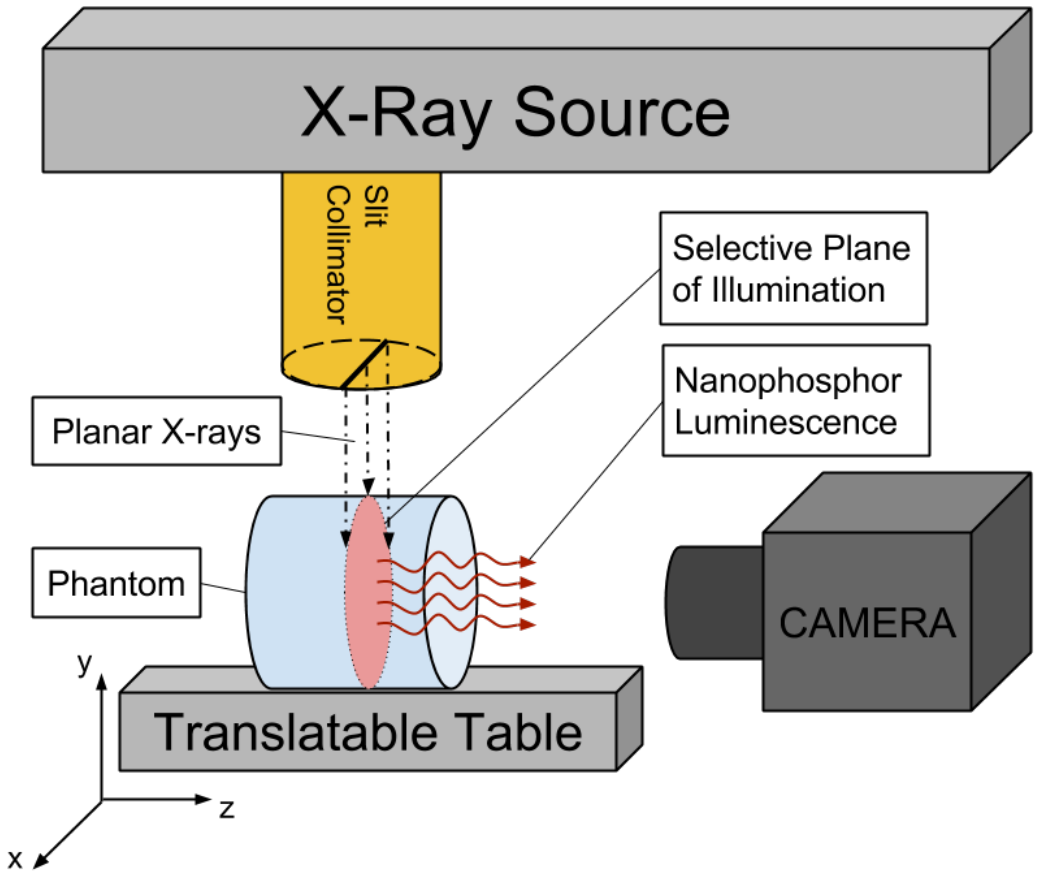

Figure 4.1: Diagram of selective plane x-ray induced luminescence imaging. A slit collimator produces planar x-rays which selectively excite the nanophosphors within the phantom. The phantom is translated through the plane of illumination along in imaging axis which is orthonormal to the selective plane.

the selective plane is parallel to a flat imaging surface and orthonormal to the camera axis further simplifies the imaging model into a two-dimensional convolution. This is outlined in Equation 4.1, where the plane of luminescence is defined with $P(x, y, z)$, and the normalized surface radiance function N serves as a point source function:

$$f(x_0, y_0) = \iiint P(x, y, z) N\big(\sqrt{(x_0 - x)^2 + (y_0 - y)^2}, z\big) \; dxdydz \; . \tag{4.1}$$

This equation is further simplified using the convolution notation and the radial coordi-

nate r_0 to define the point of radiance on the surface. The selective plane used in imaging has a finite thickness, z_s. Therefore, the selective plane at depth z_0 is integrated over its the thickness as shown in Equation 4.2:

$$f(r_0) = \int_{z_0-\frac{z_s}{2}}^{z_0+\frac{z_s}{2}} \big(P * N\big)(r_0, z_0)\; dz, \quad \text{where} \;\; r_0 = \sqrt{x_0^2 + y_0^2}\;. \tag{4.2}$$

4.3 Richardson-Lucy Deconvolution

The convolution-based selective plane imaging model leads to a straightforward reconstruction by employing a deconvolution. The normalized surface radiance function serves as a point spread function for the plane of radioluminescence in the object. The point spread function is defined by the depth of x-ray induced luminescence and the optical properties of the medium. Full knowledge of these parameters thus allows the recovery of the distribution of radioluminescence in the plane of excitation by deconvolving it from the detected surface radiance.

The statistics of the optical signal detected at the surface are a combination of Poisson counting noise and Gaussian noise from dark current and readout noise in the camera pixels. Since the sum of a Poisson distribution and a Gaussian distribution does not yield a tractable likelihood function, a shifted Poisson model is employed [63, 64]. The mathematics of this pre-processing are outlined in Equation 4.3:

$$\tilde{g} = [(g - b) + \sigma^2]\;. \tag{4.3}$$

The detected image g has the pixel bias b removed. This is accomplished by subtracting the dark images from the detected surface radiance measurements. Then the Gaussian noise variance σ^2 is added back in to produce the input image $\tilde{g}$ for the deconvolution. The pre-processing results in a statistical transformation to the data wherein it produces

a new random variable whose mean and variance equal that of a Poisson random variable appropriately defined. The shifted Poisson model has previously been applied to image reconstructions of x-ray CT with noisy, degraded image sets [65].

The algorithm used for reconstructing the radioluminescence distribution is a maximum likelihood Richardson-Lucy deconvolution[66, 67]. The update step of the algorithm is defined in Equation 4.4:

$$f^{i+1} = f^{i}\left(k^{T} * \frac{\tilde{g}}{k * f^{i} + \sigma^{2}}\right) . \tag{4.4}$$

f^{i} is the image estimate from the i^{th} iteration, and k is the point spread function defined by the normalized surface radiance function at the depth of the sheet beam. In the case of the two-dimensional deconvolution, the initial estimate $\tilde{g}$ is the corrected detected image. This initial estimate in the deconvolution will change in the subsequent chapter when a pencil beam geometry is used and the deconvolution becomes one-dimensional.

4.4 Experimental Selective Plane X-ray induced Luminescence Imaging

The experimental selective-plane x-ray induced luminescence imaging was performed in the small animal irradiator using the same gel phantom recipe outlined in chapter two. The only modification necessary for to the experimental setup was the production of a sheet beam. This was accomplished with a slit collimator on the x-ray source. The selective-plane x-ray induced luminescence imaging was first performed on an optically clear phantom for a simple proof-of-concept measurement. Then the imaging system was used to detect a dual nanophosphor point source in a diffuse optical imaging phantom, so that the Richardson-Lucy deconvolution could be tested experimentally.

4.4.1 Slit collimator construction

The slit collimator was constructed out of Cerrobend and plastic spacers. Cerrobend is a metal alloy with a low melting point of 70 that was historically used in radiation therapy clinics for rapid production of custom, form-fitting x-ray fields before the advent of multileaf collimators. Cerrobend was poured into a circular mold in order to produce a disc. After the metal alloy solidified, the disc was cut in half. Then plastic sheets of 0.6 mm and 0.3 mm were cut into small squares, so they could be placed between the two half-moon pieces of Cerrobend and form a gap. The width of this gap could be varied based on which plastic spacers were used. The disc was connected to the end of a brass collimator in order to produce a slit collimator for the small animal irradiator source. As seen below in Figure 4.2, radiochromic film was used to measure the width of the x-ray illumination plane at the isocenter and confirm that it was aligned orthonormal to the camera's imaging axis.

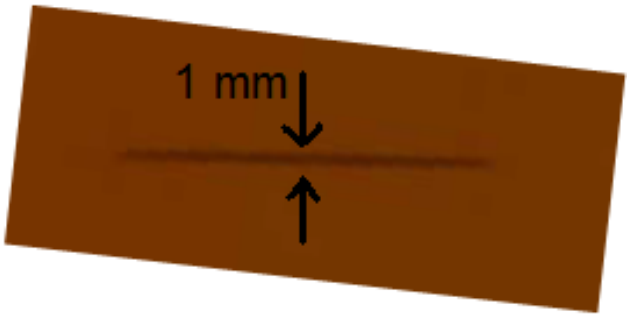

Figure 4.2: Radiochromic image of Cerrobend slit collimator within the small animal irradiator. This particular setup had a slit width of 1 mm, but changing the plastic spacers in the slit collimator allowed for various slit sizes.

4.4.2 Optically clear phantom

The selective-plane x-ray induced luminescence imaging system was first tested on an optically clear phantom for a simple proof-of-concept experiment. A spiral phantom was constructed by filling a catheter tube with an aqueous solution of nanophosphors and wrapping it around a test tube. A photo of the phantom is shown in Figure 4.3. The phantom was placed on the treatment bed beneath the slit collimator and the x-ray induced luminescence was imaged using a consumer CMOS camera (5D Mark II, Canon). A photo of the setup is shown in Figure 4.4. The phantom was irradiated with a tube voltage of 140 kVp and a tube current of 20 mA. An exposure time of 30 s was used in acquiring the images for each slice position. The phantom was translated in 1 mm steps along the direction of the camera axis for a total of 40 positions. Therefore the z-direction of the selective plane x-ray induced luminescence image stack has a depth of 4 cm.

Figure 4.3: Photograph of the optically clear spiral phantom. The catheter tube was filled with an aqueous solution of nanophosphors and wrapped around a test tube.

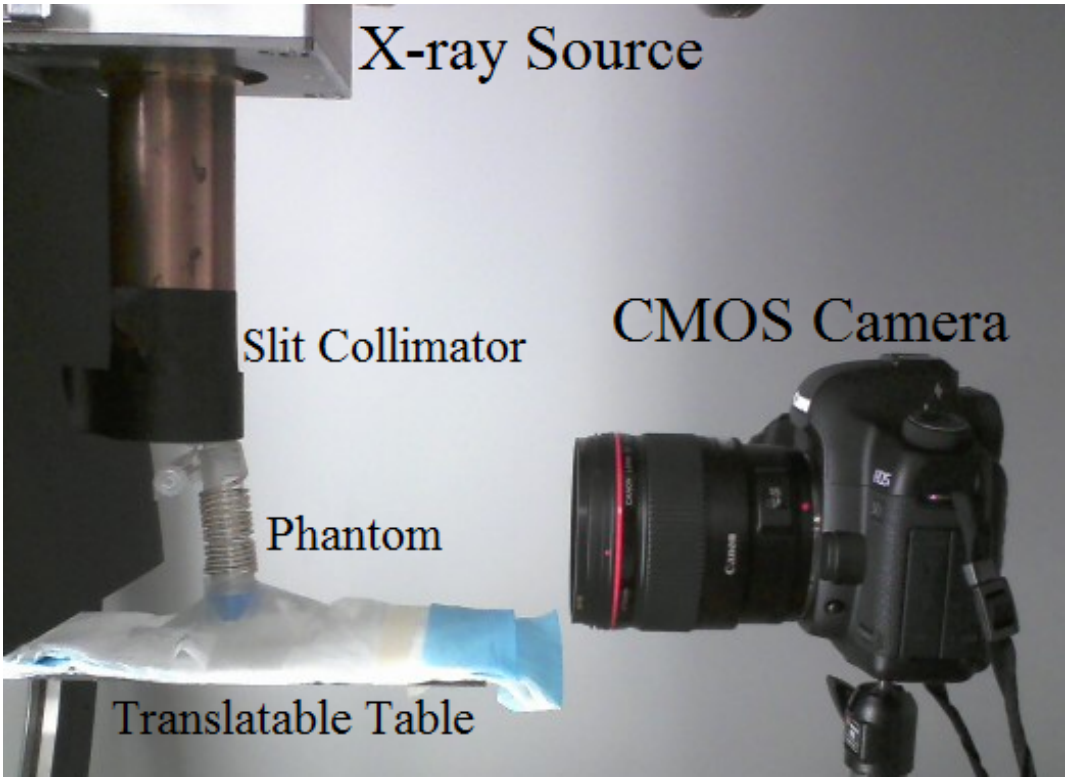

Figure 4.4: Experimental setup for the selective plane x-ray induced luminescence imaging of the optically clear spiral phantom in the small animal irradiator. The phantom was translated in the direction of the imaging axis in order to acquire a three dimensional image stack.

The sheet-beam illumination selectively excites portions of the spiral phantom. Individual consecutive slices of the image stack are shown below in Figure 4.5. A maximum intensity projection along the z-direction was applied to the image stack and the result is depicted in Figure 4.6. The original form of the phantom was successfully recovered, demonstrating the feasibility of selective excitation of nanophosphors within a phantom.

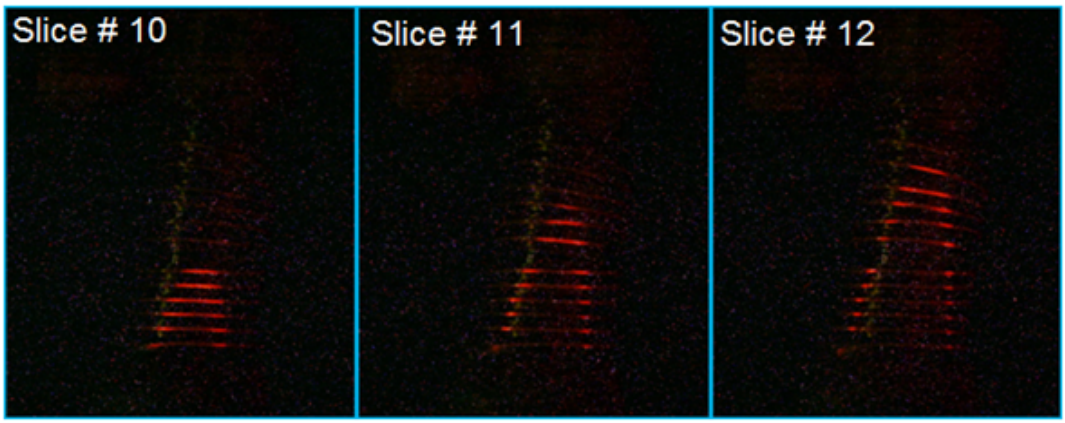

Figure 4.5: A set of consecutive selective plane slices from the x-ray induced luminescence image stack. The x-ray induced luminescence is constrained to the intersection of the x-ray sheet beam and the spiral phantom.

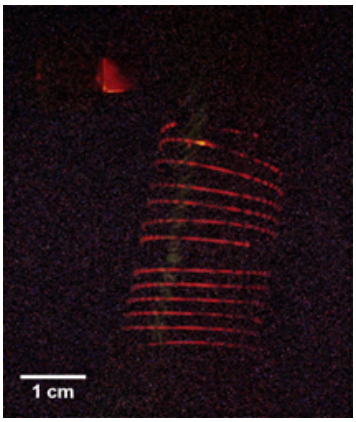

Figure 4.6: Maximum intensity projection along the z-direction of the selective plane x-ray induced luminescence image stack. The spiral shape of the nanophosphors within the twisted catheter tube is successfully recovered by the experiment.

4.4.3 Diffuse imaging phantom

Selective-plane x-ray induced luminescence imaging within a diffuse optical environment proves to be a more challenging reconstruction problem compared to an optically clear phantom. Unlike the case of the clear phantom, the surface radiance is insufficient to resolving objects at depth due to absorption and scattering of the optical signal in the diffuse medium. However, this can be overcome in the case of an optically homogeneous environment by using the selective-plane geometry and deconvolution.

In order to demonstrate this experimentally, an optical gel phantom was fabricated with two tubes containing the nanophosphors suspended in agar. The gel phantom was poured with the two tubes in positions, such that they were spaced half a centimeter apart and their tips were located approximately 4 mm below the imaging surface. A CT image of the dual-source nanophosphors tubes is shown in Figure 4.7 and it oriented such that the top of the image is the surface of the phantom where the luminescence is detected.

A larger slit was used in this experimental selective-plane x-ray induced luminescence imaging experiment. The width of the planar x-rays were measured to be 2.5 mm. The gel phantom was irradiated with a tube voltage of 140 kVp and a tube current of 20.89 mA starting near the imaging surface with the planar x-rays impinging on the tips of the tubes. A 20 s exposure was captured with the cooled CCD and the macro lens, and then the phantom was translated 2.5 mm along the imaging axis and the process was repeated until there was no longer a detectable optical signal from the imaging surface. Figure 4.8 shows the experimental setup for the dual-source phantom with the slit collimator attached to the x-ray tube and the shielded camera for detecting the x-ray induced luminescence.

Two of the detected images corresponding to the shallowest depths of the tubes are shown unprocessed in Figure 4.9. The large amount of bright specks are the result of scattered x-rays interacting with the camera sensor. This is the result of imperfect shielding and x-rays that scatter off the phantom directly towards the camera. These spurious counts need to

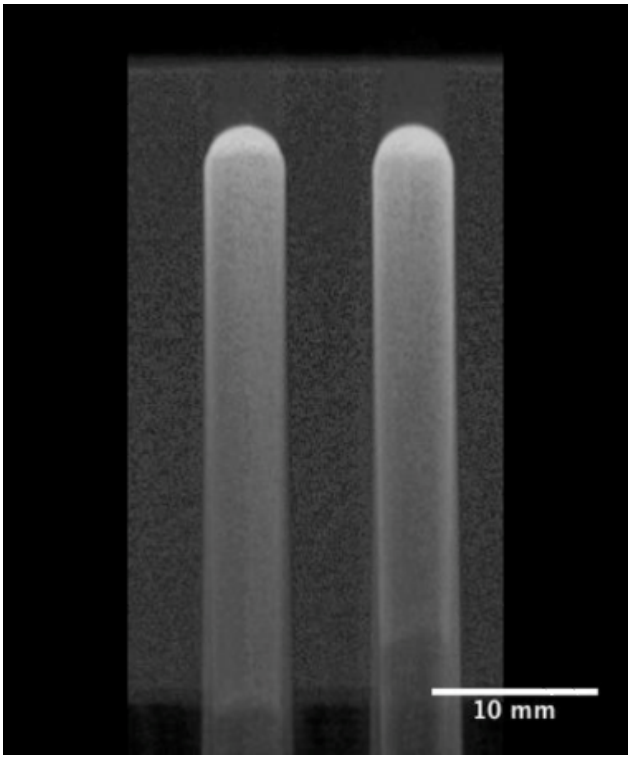

Figure 4.7: Maximum intensity project of a CT volume containing the dual source nanophosphor tubes within the optical gel phantom. The tubes contain the nanophosphors suspended in agar are spaced apart by 0.5 cm. The tips of the tubes sit approximately 4 mm below the imaging surface. The planar x-rays impinge orthogonally upon this image, so that it is orientated parallel to the image surface.

first be removed before the deconvolution so thresholding was applied to pixels with large ADU values compared to their neighbors. The threshold value was set at 700 ADU while the max ADU value for the 14-bit camera was 16383 ADU. The detectable optical signal at the surface of the phantom was low compared to the full dynamic range of the camera, even when it was operating on the most sensitive gain settings. In contrast, the spurious counts from x-rays interacting with the camera could range from 1000 ADU to the entire electron well depth of the pixel with the maximum ADU value. Hence this thresholding was necessary in order to ensure a reconstruction that would be unaffected by the spurious counts. Pixels that were identified to be above the threshold level had their pixel value replaced with the median of the eight pixels that surrounded it.

Figure 4.8: Experimental selective plane x-ray induced luminescence imaging with dual source optical gel phantom inside the small animal irradiator.

After the "hot" pixels were removed from the image, the measurement was transformed as outlined in Equation 4.3. The processed images were then input into the Richardson-Lucy algorithm with the normalized surface radiance as the point spread function for their respective depths. The iterative algorithm written in Python was run until the L2 norm of the difference between consecutive iterations was less than 10^{-6}. Three of the processed images are shown in the top row of Figure 4.10. The bottom row contains the corresponding results of the Richardson-Lucy algorithm.

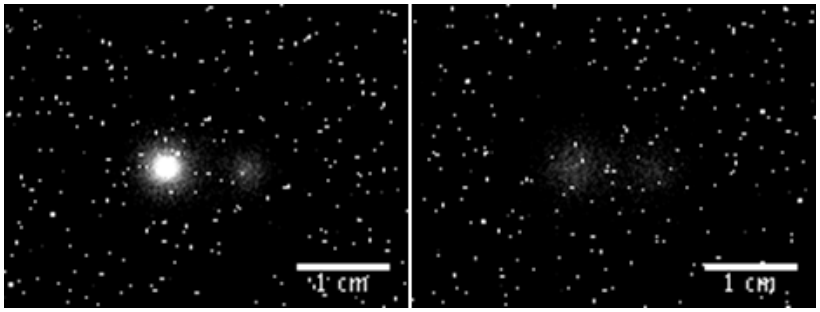

Figure 4.9: Unprocessed images of the detected surface radiance for the sheet beam at a depth of 0.5 cm (left) and 0.75 cm (right). The spurious counts are the result of scattered x-rays.

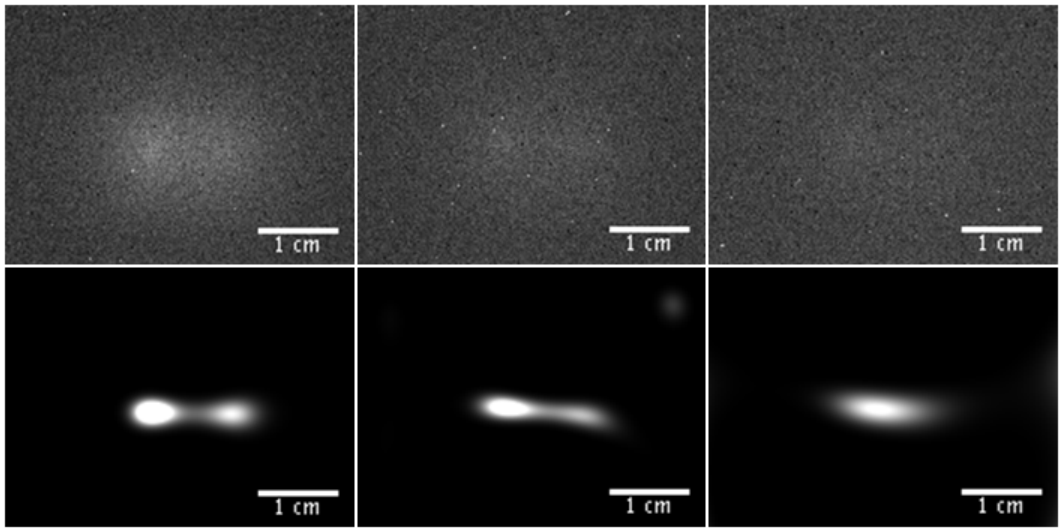

Figure 4.10: The top row depicts the processed detected surface radiance measurements for the depths of 1.0 cm (left), 1.5 cm (middle), and 2.0 cm (right). The hot pixels have been removed from the images, the dark image has been subtracted, and the Gaussian noise was added back in as described by Equation 3.3. The bottom row contains the corresponding deconvolved images.

The deconvolution was able to successfully resolve the two tubes up to a depth of 1.75 cm in the diffuse imaging environment. Beyond that depth the Richardson-Lucy algorithm reconstructed a single luminescent source at depth in the phantom, and past the depth of 2.25 cm there was no longer a detectable optical signal at the surface of the phantom. The deconvolved image stack was then resliced in the horizontal direction and is shown in the bottom of Figure 4.11. This is in comparison to the resliced image stack of the raw

measurements depicted in the top of Figure 4.11. The average peak-to-peak distance in the deconvolved sources was 9.3 mm compared to the 10 mm spacing between the centers of the two tubes in the phantom.

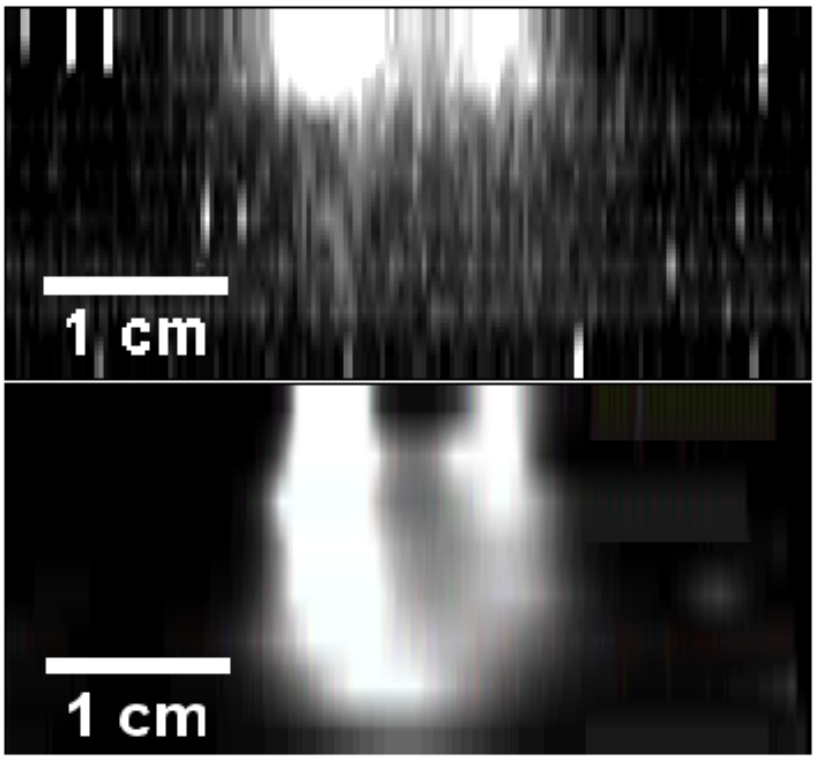

Figure 4.11: XZ reslice of the unprocessed surface radiance measurements image stack (top) and deconvolved image stack using a Richardson-Lucy algorithm (bottom). The deconvolution was able to resolve the two tubes up to a depth of 1.75 cm in the diffuse optical gel phantom.

4.5 Discussion

These results were the first published example of experimental x-ray induced luminescence imaging in a optically diffuse environment using a selective plane geometry and a deconvolution-based reconstruction [32]. The resolution of this technique is limited in the axial direction comparatively to the image plane, due to the finite thickness of the selective plane. This resolution can be improved by narrowing the slit collimator, but that causes a

trade off in incident x-ray flux resulting in a reduced radioluminescent signal. The reconstruction could then be improved by rotating the object 90 degrees and repeating the selective plane x-ray induced luminescence measurement. This approach has been demonstrated in dual-view light sheet microscopy to markedly improve the three-dimensional reconstruction of the object [68].

It is important to note that the two dimensional convolution imaging model with the selective plane geometry works because the detecting surface is flat and parallel to the imaging plane, and the object is optically homogeneous. This is no longer the case when object is heterogeneous and the surface is uneven. In that case the simple normalized surface radiance function can no longer accurately predict the surface luminescence resulting from the diffuse light transport. Nevertheless, the selective-plane geometry still reduces the imaging model from a more ill-posed three-dimensional integral equation to a less ill-posed two-dimensional integral equation. Further advanced modeling based on approximations, such as the Born or Rytov approximations [1], becomes necessary or prior knowledge of nature of the heterogeneous optical properties is required in order to tackle the image reconstruction in an optically heterogeneous environment.

CHAPTER 5

X-RAY FLUORESCENCE AND X-RAY LUMINESCENCE IMAGING WITH A PENCIL BEAM GEOMETRY

5.1 Introduction

5.1.1 Dual modality imaging

X-ray induced luminescence imaging employs phosphorescent nanoparticles that emit near-infrared light in the presence of ionizing radiation. Nanoparticles composed of high atomic number elements will also exhibit x-ray fluorescence provided that the incident photons have sufficient energy to interact with K-shell electrons. Here we present imaging with a monochromatic pencil beam interacting with $Y_2O_3 : Eu^{3+}$ nanoparticles producing both x-ray luminescence and x-ray fluorescence within an optical gel phantom. The yttrium in the nanoparticles exhibits a K-edge absorption line at 17.04 keV. The pencil beam source produces x-rays slightly above the K-edge at 17.4 keV. The fact that the x-ray source is monochromatic will be important later, because it allows the detector to differentiate between scattered x-rays from the pencil beam and the 14.9 keV fluorescent photons emitted from the yttrium in the nanophosphors.

Each modality has its own advantage in this environment. The fluorescent x-rays have a low yield, but escape the phantom with little scattering, which leads to high resolution image of the yttrium distribution within the pencil beam. The x-ray induced luminescence has a high yield of optical photons per incident x-ray photon, but poor resolution due to scattering and absorption of the optical photons in the gel phantom as they travel towards the surface. The x-ray fluorescence and induced luminescence signals can potentially be combined in a joint reconstruction that has both high sensitivity and high resolution. This imaging technique is first demonstrated in simulation followed by an x-ray fluorescence/x-ray

luminescence joint reconstruction on experimental data collected with a benchtop system.

5.1.2 System Geometry

Figure 5.1 depicts the setup of the x-ray fluorescence/x-ray luminescence imaging system. The pencil beam impinges on the sample perpendicular to the cameras' imaging axes. The x-ray fluorescence is detected with an x-ray CCD camera fitted with a vertical slit aperture. Each column on the detector maps to a voxel along the pencil beam due the imaging geometry. Thus the resulting detected x-ray fluorescence can be collapsed vertically along the pixel columns producing a detected line of x-ray fluorescence corresponding the pencil beam's position in the phantom. The luminescence is detected at the surface of the imaging phantom with an electron-multiplying CCD (EMCCD) camera and demagnifying tube. The pencil beam geometry and optically homogeneous imaging phantom allow for the reconstruction of the luminescence at depth along the pencil beam in the phantom via a one-dimensional deconvolution.

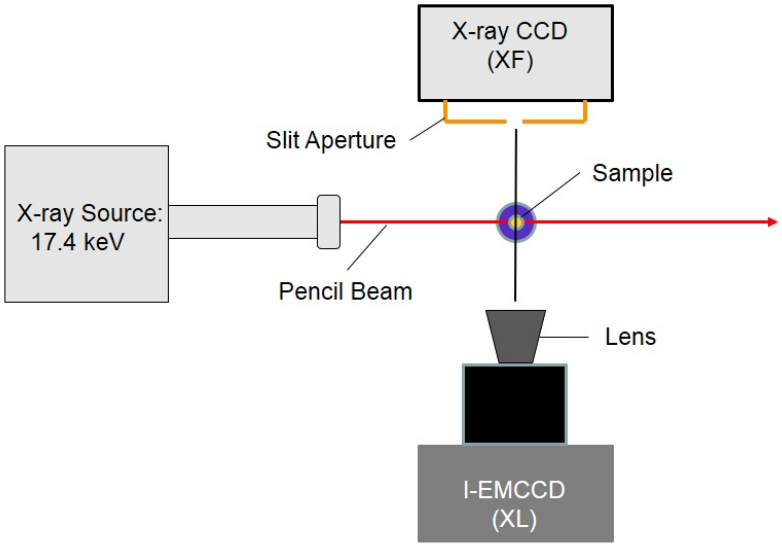

Figure 5.1: Diagram of x-ray fluorescence/x-ray luminescence imaging setup with monochromatic pencil beam source.

5.1.3 Experimental benchtop system

The experimental benchtop system is depicted in Figure 5.2. The monochromatic x-ray pencil beam is produced by a sealed tube micro source with a molybdenum target yielding the 17.4 keV photons. (GeniX 3D Mo High Flux, Xenocs). A vertical slit aperture with a width of 100 microns is fitted to the x-ray CCD (iKon-L DO936, Andor). The x-ray induced luminescence is detected on the opposite side of the symmetrical phantom. The EMCCD (iXon 887, Andor) detects the luminescence of the phantom's surface with a demagnifying tube (Distagon T* 2.8 25mm EF.2 Lens, Ziess). The gel phantom was constructed with a 5 cm by 5 cm square face with a thickness of 1.6 cm. The phantom is 1% agar gel which approximates the optical properties of mammalian tissue with the addition of 0.5% Intralipid and 0.0025% black India ink. The tips of two capillary tubes with an inner diameter of 0.6 mm were filled with the $Y_2O_3 : Eu^{3+}$ nanophosphors in order to serve a point sources. They were inserted into the phantom in the center so that they sat 8 mm below the gel surface of either face of the phantom. The spacing of the capillary tubes tips at the pencil beam location was 2.9 mm as measured in the x-fluorescence reconstruction. The pencil beam has a measured full width-half maximum of 156 microns and was scanned horizontally through the phantom with a step size of 200 microns between beam positions.

5.2 X-ray Fluorescence Simulation and Measurement

5.2.1 X-ray Fluorescence Imaging Model

The physics of x-ray fluorescence imaging can be broken down into three stages: the incident x-ray beam penetrates of the object, x-ray photoelectric interactions and fluorescence yield, and the detection of x-ray fluorescent photons exiting the object. These three basic steps are delineated by the brackets in Equation 5.1, which is provided from research on x-ray fluorescence computed tomography using a pencil beam/slit geometry with a synchrotron

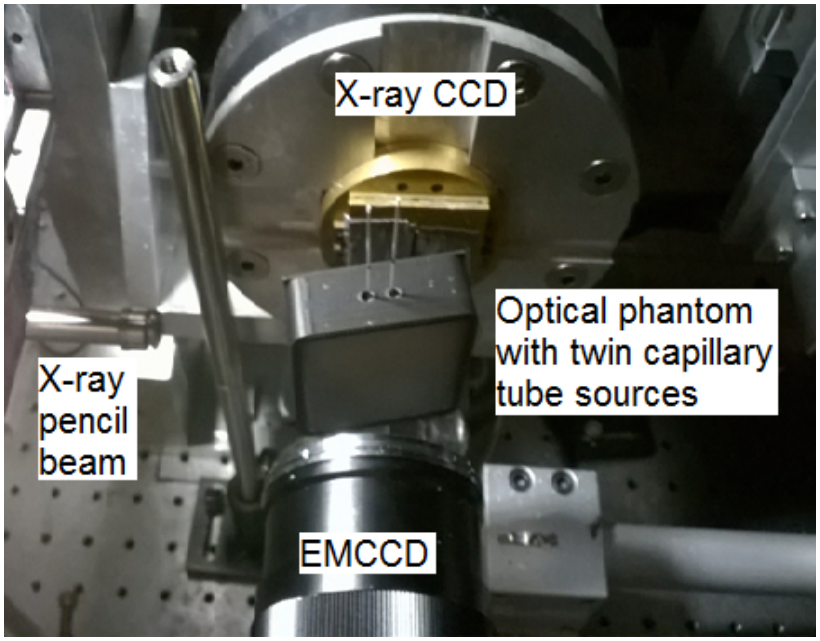

Figure 5.2: Photo of the benchtop x-ray fluorescence/x-ray luminescence imaging system with monochromatic pencil beam source. The experiment imaged dual point sources at a depth of 0.8 mm in the gel phantom.

source [69]:

$$y_{pix} = [I_0 A t F_{pix}(\vec{\mu}_{inc})]\Big[\Big(\frac{\tau}{\rho}\Big)_Y p_k \rho_Y \Delta x \omega_k \nu_\alpha\Big][G_(\vec{\mu}_{Fluoro})\Omega\epsilon] \ . \tag{5.1}$$

The number of incident photons that reach a give voxel in the object is based on the incident photon flux density I_0, the beam area A, the dwell time t, and the fraction of incident photons that have not been attenuated before reaching the voxel F_{pix}. This last term is determined by Beer-Lambert law, the distance the pencil beam travels through the object, and the mass-attenuation coefficient of the incident photons. The simulation for the 17.4 keV pencil beam shows significant attenuation by the nanoparticles due to the high-Z component elements. The surrounding gel phantom has a mass-absorption coefficient of 1.26 cm^2/g, while the effective mass-absorption coefficient of the nanoparticles is 77.66 cm^2/g.

The second set of terms in the equation deals with the x-ray fluorescence phenomenon. The photoelectric cross-section determines the likelihood of the incident photons interacting

with the yttrium in the nanoparticles. This along with the density of the yttrium ρ_Y and the voxel of size Δx determines the number of photoelectric interactions within a given pencil beam voxel. The fraction of photoelectric interactions with K-shell p_k and the fluorescence yield of K-shell ω_k determines the number of K-shell fluorescent photons that results from the photoelectric interactions. The fraction of these fluorescent events that result from the K-alpha transitions, which emit a characteristic x-ray of approximately 14.9 keV, is determined by the branching ratio ν_α.

Finally, the fluorescent photons generated in the voxel are detected by a corresponding pixel column on the detector. The fraction of emitted x-rays that escape the phantom without attenuation are represented by the function G, which is calculated with the Beer-Lambert law using the distance traveled through the phantom to reach a pixel in the detecting column and the phantom's mass-attenuation coefficient for the 14.9 keV fluorescent x-rays. The geometric efficiency Ω corresponds to the fraction of isotropically emitted fluorescent x-rays from a voxel subtended by the slit aperture, which has a width of 100 microns and a height of the corresponding detecting pixel column in the slit's imaging plane. The x-ray CCD detects incident photons on a pixel with quantum efficiency ϵ. The values used in the simulation are based on the experimental conditions and listed in Table 5.1.

5.2.2 Photon Counting

The x-ray CCD features a high dynamic range in its photon energy detection, thus allowing the camera to operate in a photon-counting mode. This is possible in a low-exposure condition, where detection events are spatially isolated, such that the recorded signals in a given region of the detector can be assigned to a single x-ray interaction [70]. An x-ray interaction with the CCD pixel can cause electrons to spill into neighboring pixels. Therefore the photon counting algorithm summed up all the neighboring pixels with ADU values above the background levels to determine the total ADU value of the detection event. The

Quantity	Definition	Units	Value
y_{pix}	Detected number of photons in pixel for element of interest	Number	Simulation output
I_0	Incident photon flux density	Number $s^{-1}cm^{-2}$	1.03×10^{11}
A	Beam Area	cm^2	2.43×10^{-4}
t	Dwell time	s	10
$F_{pix}(\vec{\mu}_{inc})$	Fraction of incident photons that reach pixel of interest without being attenuated	Dimensionless	Determined by attenuation map
$(\frac{\tau}{\rho})_Y$	Photoelectric cross section	cm^2/g	96.4
p_k	Fraction of photoelectric interactions with K shell	Dimensionless	0.8
ρ_Y	Density of Y_2O_3:Eu^{3+}	g / cm^3	0.12
Δx	Voxel size	cm	2.62×10^{-3}
ω_κ	Fluorescence yield of K shell	Dimensionless	0.71
ν_α	Branching ratio of detected line(s)	Dimensionless	0.854
$G(\vec{\mu}_{Fluoro})$	Fraction of emitted x-rays that reach slit opening without being attenuated	Dimensionless	Determined by fluorescent photon path length
Ω	Geometric efficiency	Dimensionless	2.49×10^{-4}
ϵ	Detector efficiency at emission energy	Dimensionless	0.08

Table 5.1: Parameters used in x-ray fluorescence simulation with pencil beam/slit geometry.

summed ADU value of the detecting pixels can serve as a proxy for incident x-ray energy under this low-exposure regime. A total of 60 low-exposure images was acquired for each pencil beam position during the x-ray fluorescence imaging scan. The set of all pixel values in the 60 images were then plotted as a histogram which displays a large peak for scattered incident pencil beam photons and a smaller peak for characteristic fluorescent x-rays from the yttrium. Figure 5.3 shows the histogram for one pencil beam position exhibiting fluorescence. The pixel value limits of the smaller x-ray fluorescence peak are identified and then applied to the detected images to produce a photon-counting image of the fluorescence with scattered pencil beam x-rays subtracted. An example of the resulting image from 60 acquired experimentally and combined after the removal of scatter is shown in Figure 5.4.

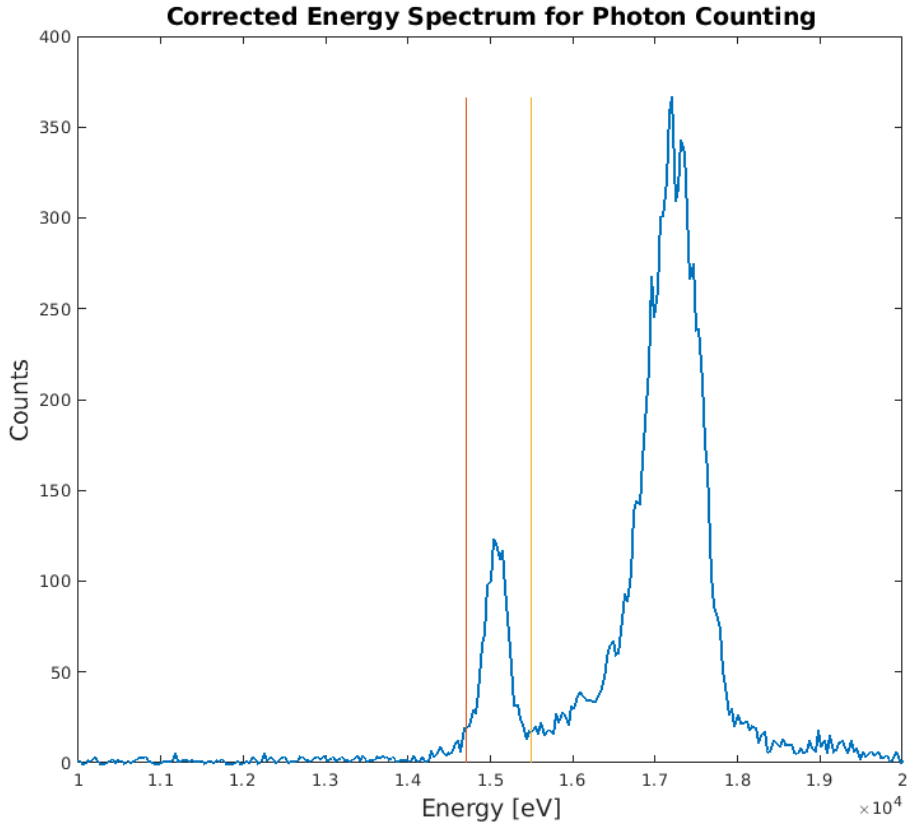

Figure 5.3: Energy spectrum of the detected photons for a pencil beam position exhibiting x-ray fluorescence. The large peak represents the scattered photons of the x-ray incident beam striking the detector and the smaller peak represents fluorescent photons from the yttrium's K-shell.

5.2.3 Density Calibration

The nanophosphor point sources were created by inserting the nanoparticles in powdered form into the tips of capillary tubes. This simple method led to a unknown density of nanoparticles within the tubes. This was the only unknown parameter of the experimental setup in the imaging model. Therefore a density calibration was required in order to estimate the density of the nanoparticles from the measured yttrium fluorescence. The simulation was initially run assuming a nanoparticle concentration of 1 g/mL. The nanoparticles are composed of Y_2O_3 nanocrystals doped with 5% Eu^{3+}. Thus the nanophosphors are 76.1%

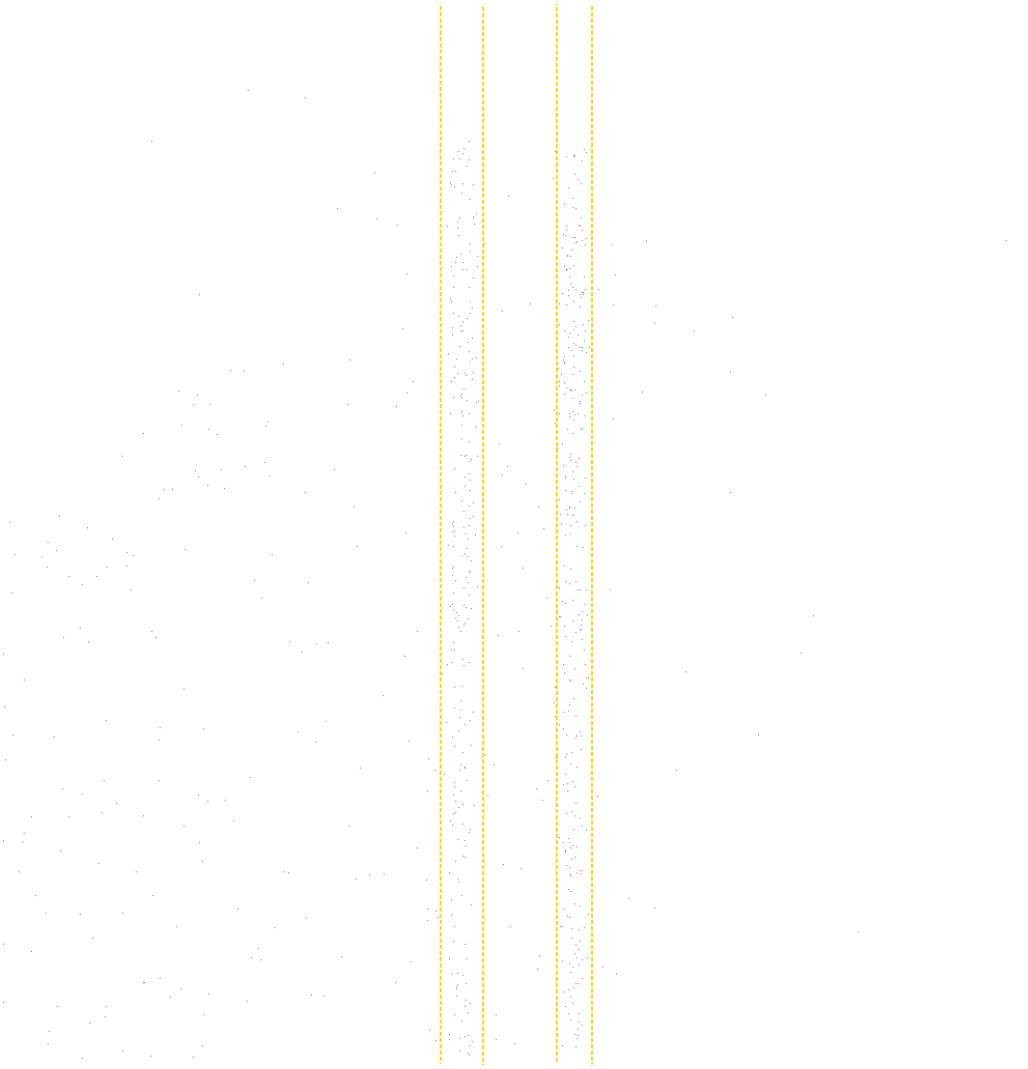

Figure 5.4: Experimental x-ray fluorescence image of a single pencil beam position with dual source fluorescence. Photon counting has been applied with the detected scattered pencil beam events identified and removed. The image has been inverted where the black spots represent pixels detecting the x-ray fluorescence and signal is present between the dotted orange lines. The resulting image is a combination of all 60 frames with pixel values corresponding to yttrium's characteristic K-edge. Each pixel column in this image is collapsed vertically in order to produce the line of detected fluorescence in the phantom corresponding to the pencil beam position.

yttrium by mass. This initial estimate was used to produced a simulated image of the tube fluorescence where the total simulated fluorescence in the first tube was compared with the experimental measurement in order to determine a density calibration factor. The results indicated a density of 0.16 g/mL of nanoparticles within the tubes. The simulation was then repeated with the calibrated density. Figure 5.5 shows the line profiles for the pencil beam positions corresponding to peak fluorescence of the first and second tube in the phantom, the first being brighter since it experiences a greater flux of incident x-ray photons. The mean fluorescence of the line profile of the first tube is 40.9 counts in the experiment and 39.1 in the simulation. The mean fluorescence of the line profile of the second tube is 22.7 counts for the experiment and 27.8 counts in the simulation. Note that the peak fluorescence in the second tube from the experimental data occurs for a pencil beam position that is not striking the first tube, due to imprecision in aligning the tubes with the pencil beam. Therefore the simulated profile for the second tube here assumes no primary tube in the x-rays' path. However, the rest of the simulations outlined here for the x-ray fluorescence and luminescence assume the ideal case where the sources are aligned with the incident pencil beam.

5.2.4 X-ray Fluorescence Reconstruction

The pencil beam/slit geometry leads to a simple reconstruction for each beam position. The total x-ray fluorescence detected across 60 images for a given pencil beam position is amassed into a single frame. Then each pixel column is summed together to create a single voxel that corresponds to a location along the x-ray pencil beam in the object. Finally, an attenuation correction is applied to the line reconstruction using the attenuation map calculated for the term $F_{pix}(\vec{\mu}_{inc})$. A total of 23 coplanar pencil beam positions were acquired in the gel phantom. Each collapsed fluorescence image is then lined up together in order to reconstruct the x-ray fluorescence for the given slice in the phantom.

The experimental and calibrated simulated reconstructions easily detected the fluorescent

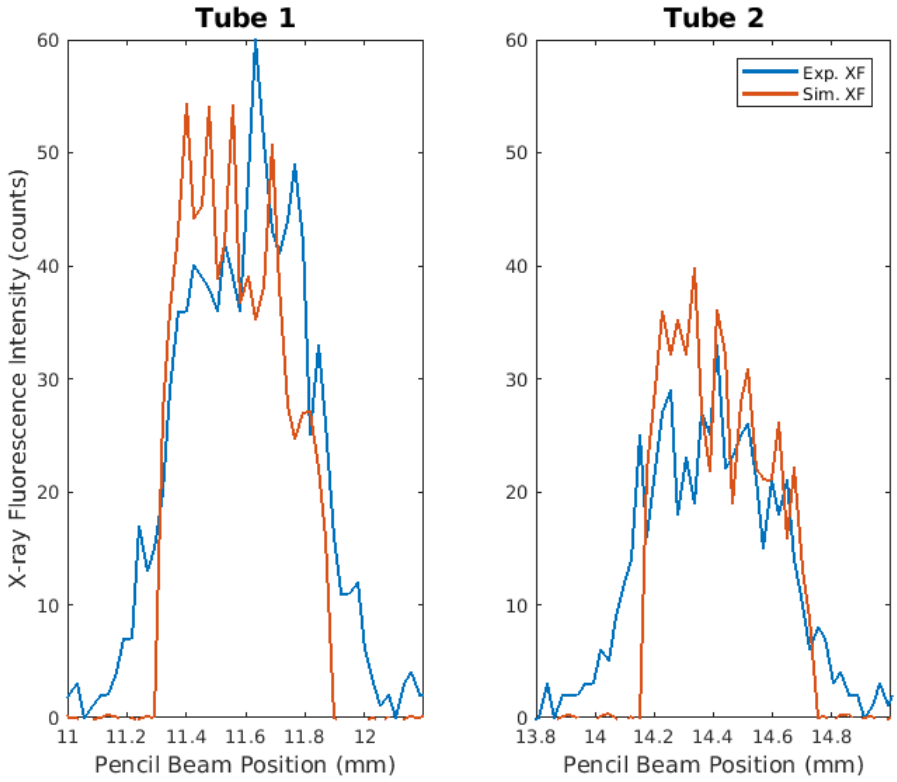

Figure 5.5: Lines profiles of the detected x-ray fluorescence through the first and second tubes in the phantom. The lines show the peak luminescence of each tube for the experimental measurement and the calibrated simulation.

x-ray tubes. Therefore, a poor quality reconstruction was carried out in which only 10% of the pixels in collapsed pixel column were used to recover the x-ray fluorescence along a given pencil beam position. These poor quality x-ray fluorescence reconstructions represent the lower limits of detectability with the benchtop system, and correspond to one tenth the imaging time of standard reconstructions. The standard imaging time for x-ray fluorescence was 600 seconds and the "poor quality" reconstructions correspond to a 60 seconds exposure. Figure 5.6 depicts the simulation results with the top row containing the nanophosphor tubes from the calibrated simulation. The bottom row contains the reconstruction of the tubes using one tenth of the fluorescent signal. Similarly, Figure 5.7 shows the experimental x-ray fluorescence reconstructions with the top row displaying the standard reconstruction and the

bottom row displaying the reconstruction with one tenth the experimental signal.

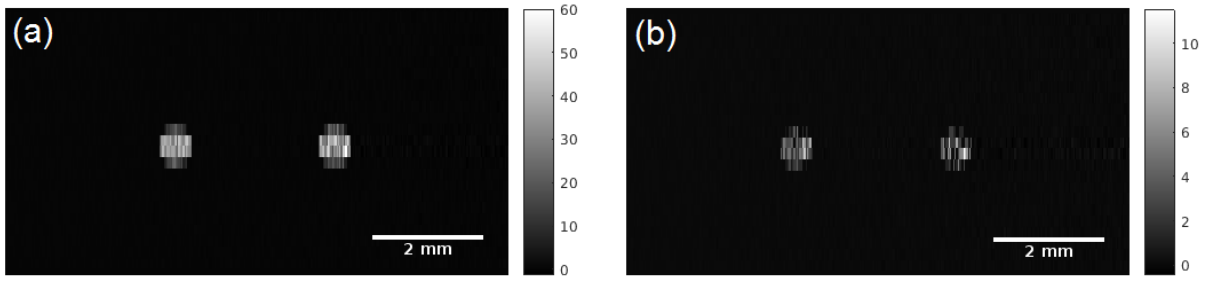

Figure 5.6: X-ray fluorescence reconstruction using the calibrated simulation (a) and the poor reconstruction with one tenth the fluorescent signal (b). The tubes have an inner diameter of 0.6 mm and are spaced apart by 2.9 mm.

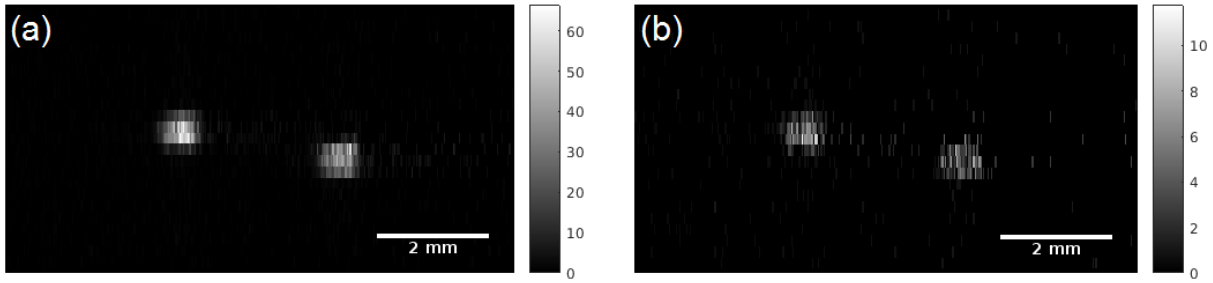

Figure 5.7: Experimental x-ray fluorescence reconstructions using the measured data (a) and the sparse sampling reconstruction with 10% of the vertical pixels (b).

5.3 X-ray Luminescence Simulation and Measurement

5.3.1 X-ray Luminescence Imaging Model

The detection of the x-ray induced luminescence is less straightforward than the fluorescence, because the optical photons travel undergo many scattering events before escaping the phantom. The migration of the photons to the surface of the phantom under these conditions is well described by diffuse transport equations. The resulting luminescence at a single

point on the phantom's surface can be the combination of optical photons from multiple locations along the incident pencil beam, which creates ambiguity. However the knowledge of the photon diffusion combined with the fixed geometry makes a deconvolution possible that can reconstruct a luminescent object at depth, but with lower resolution compared to x-ray fluorescence imaging. The x-ray induced luminescence simulation and reconstruction is based on the following series of equations.

The dose of the pencil beam in the phantom is determined using Equation 5.2:

$$D_{voxel} = I_0 E t F_{voxel}(\vec{\mu}_{\text{inc}}) \left(\frac{\mu_{en}}{\rho} \right) . \tag{5.2}$$

The photon fluence is calculated as the incident photon flux density I_0, the incident photon energy E, and dwell time t. Only a fraction of the incident photon fluence reaches a given voxel in the phantom as described by F_{voxel} as seen above in the x-ray fluorescence imaging model. Finally, the resulting energy fluence in the voxel and the mass-energy absorption coefficient $\frac{\mu_{en}}{\rho}$ approximates the dose to the voxel.

The number of photons generated by the x-ray induced luminescence is proportional to the energy deposited in the voxel, the concentration of the nanoparticles C_{NP}, and the luminescent efficiency α_{NP} as shown in equation 5.3:

$$P_{voxel} = D_{voxel} \rho_{voxel} C_{NP} \alpha_{NP} . \tag{5.3}$$

The concentration determined by the x-ray fluorescence calibration was used again here. The luminescent efficiency was measured in previous work with these Europium-doped nanophosphors [32]. The energy deposited in the voxel is the product of the dose D_{voxel} and the density ρ_{voxel} of the materials occupying it.

The aforementioned diffuse transport equations of the luminescent photons in the phantom are described by the normalized surface radiance function. The resulting surface ra-

diance f of the phantom located at position (x_0, y_0) is the one-dimensional convolution of the normalized surface radiance function with the luminescent photon concentration voxels along the pencil beam, as shown in Equation 5.4:

$$f(x_0, y_0) = A \int P_{voxel} N(\sqrt{(x_0 - x)^2 + y_0^2},\ z_{PB})\ dx\ . \tag{5.4}$$

Here the pencil beam's depth below the imaging surface is defined as z_{PB}, and the the vertical location of the pencil beam in the object corresponds to a height of zero at the imaging surface. The cross-section of the incident pencil beam is included to produce the total photon count within the pencil beam voxels, rather than the concentration.

Finally the surface radiance from the x-ray induced luminescence is detected with the demagnifying tube connected to the EMCCD, as defined by Equation 5.5:

$$\overline{g}(x_0, y_0) = \epsilon \frac{\pi}{4} \frac{1}{(1 + |m|)^2 N^2} (\Delta g)^2 f(x_0, y_0)\ . \tag{5.5}$$

The geometric efficiency is determined by the magnification m of the imaging setup and the f-number of the lens N. A factor of $\frac{\pi}{4}$ is included because the luminescence emitted at the phantoms open face is a Lambertian surface. The total photons incident on a pixel mapped onto the surface with the demagnifying tube is the area of the pixel in image space $(\Delta g)^2$ multiplied by the geometric efficiency, surface radiance, and Lambertian surface factor. Finally, the average photons detected by the pixel $\overline{g}(x_0, y_0)$ is the quantum efficiency ϵ of the detector at the wavelength of luminescence multiplied by the incident photon count.

The values corresponding to the x-ray induced luminescence imaging in the experimental setup and those used in the simulated images are outlined below in Table 5.2.

Quantity	Definition	Units	Value
I_0	Incident photon flux density	$\frac{\text{photons}}{\text{cm}^2\text{sr}}$	1.03×10^{11}
E	Incident photon energy	keV/photon	17.4
t	Dwell time	s	4
$F_{voxel}(\vec{\mu}_{\text{inc}})$	Fraction of incident photons that reach pixel of interest without being attenuated	Dimensionless	Determined by attenuation map
$(\frac{\mu_{en}}{\rho})$	Mass-energy absorption coefficient	cm^2/g	Determined by materials in voxel
D_{voxel}	Dose to a voxel in the phantom	Number	Simulation output
ρ_{voxel}	Density of phantom	g/cm^3	Determined by materials in voxel
C_{NP}	Concentration of nanoparticles	g/cm^3	0.16
α_{NP}	Luminescent efficiency	$\frac{\text{photons/kev}}{\text{g/cm}^3}$	1.06
P_{voxel}	Luminescent photon density generated by NPs in voxel	photons/ cm^3	Simulation output
$N(x, y, z)$	Normalized surface radiance function	$\frac{1}{\text{cm}^2\text{sr}}$	Determined by phantom optical properties
z_{PB}	Pencil beam depth below the imaging surface	cm	Determined by pencil beam position
A	Beam Area	cm^2	2.43×10^{-4}
$f(x_0, y_0)$	Surface radiance of phantom	$\frac{\text{photons}}{\text{cm}^2\text{sr}}$	Simulation output
Δg	Pixel size in image space	cm	2.16×10^{-2}
ϵ	Detector efficiency at emission energy	Dimensionless	0.9
N	Camera lens f-number	Dimensionless	2.8
m	Magnification of lens	Dimensionless	0.074
$\overline{g}(x_0, y_0)$	Detected number of photons in pixel for element of interest	Number	Simulation output

Table 5.2: Parameters used in x-ray luminescence modeling.

5.3.2 X-ray Luminescence Deconvolution

The pencil-beam geometry constrains the potential origin of the two-dimensional detected surface. The depth of x-ray excitation and normalized surface radiance function yields the point spread function for luminescent point sources within the path of the pencil beam.

Therefore a deconvolution applied to the detected surface radiance can reconstruct the luminescence generated along the line of illumination in the phantom. The one-dimensional convolution outlined in Equation 5.4 was used in a Richardson-Lucy deconvolution of the detected surface radiance. The normalized surface radiance function was determined based on the optical properties of fabricated gel phantom and the depth of the pencil beam below the imaging surface. The results of the deconvolution on the simulated x-ray luminescence data are depicted in Figure 5.8. The figure depicts the reconstructed slices of the 23 pencil beam positions after running the deconvolution for 10, 100, and 1000 iterations. The reconstructed object after 1000 iterations is a singular point with a full width-half maximum of 0.83 mm. Ultimately the x-ray luminescence measurements alone are unable to resolve the two tube spaced by 2.9 mm at a depth of 8 mm in the optical phantom. There is a loss of information as the luminescent photons are absorbed and scattered on their way to the imaging surface, so that the Richardson-Lucy cannot resolve the luminescent objects. It will prove necessary to have prior information of the tubes and their spacing from the x-ray fluorescence imaging and reconstruction in order to successfully resolve two tubes in the phantom after deconvolving the surface luminescence.

5.4 X-ray Luminescence/X-ray Fluorescence (XL/XF) Joint Reconstruction

X-ray fluorescence essentially provides a direct image of the object, because the x-ray photons undergo minimal scattering before detection. Therefore the deconvolution of the luminescent signal can benefit greatly from this higher resolution image. Each pencil beam position in the x-ray luminescence image corresponds to a pencil beam position in the x-ray fluorescence image. Therefore the detected surface radiance can be mapped onto the x-ray fluorescence reconstruction along the illumination line. This is a straightforward process in the pencil beam deconvolution. The x-ray fluorescence reconstruction of the pencil beam is used as

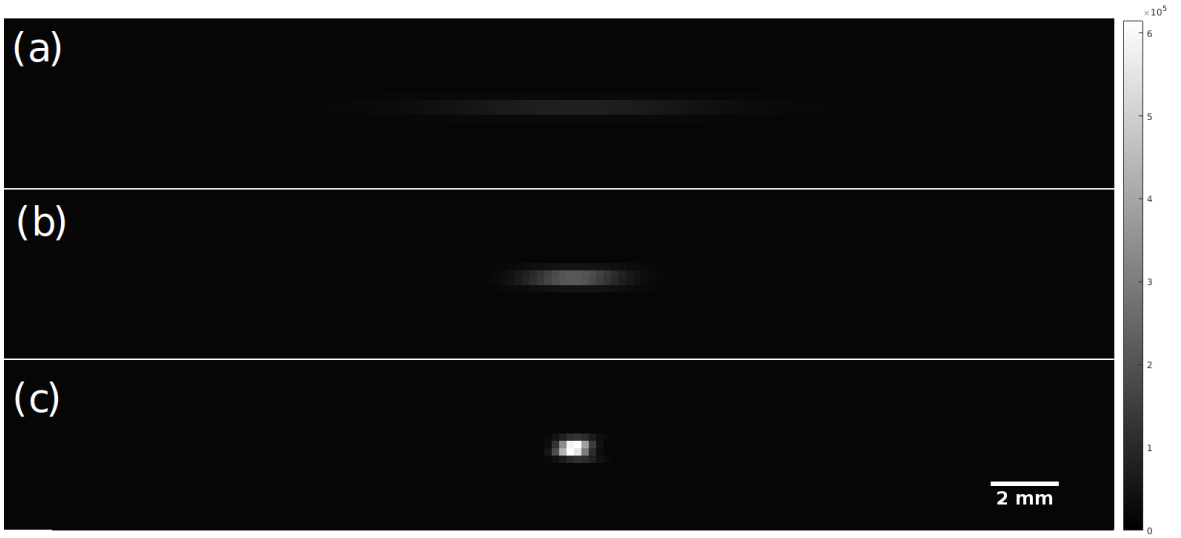

Figure 5.8: Results for 10 (a), 100 (b), and 1000 (c) iterations of the Richardson-Lucy deconvolution on the detected surface radiance of the dual-source tubes containing the nanophosphors.

a binary mask for the initial guess of the one-dimensional Richardson-Lucy deconvolution. Because the algorithm will always keep the a pixel zero if its initial guess was zero, the output of the deconvolution will only assign luminescence to regions of the pencil beam that detected fluorescence. Thus allowing for the x-ray fluorescence's higher resolution to be incorporated with the x-ray luminescence's reconstruction.

Figure 5.9 depicts the results for the simulated XL/XF joint reconstruction. The top row represents the x-ray luminescence deconvolution that used the calibrated x-ray fluorescence reconstruction as a binary mask for the initial guess in the iterative algorithm. The bottom row is the reconstruction of the tubes that used the x-ray fluorescence image with only 10 % of the original signal. Table 5.3 shows the calculated contrast-to-noise ratios (CNR) for each tube and the simulated joint reconstruction and compares it to the CNR of the corresponding x-ray fluorescence image.

Figure 5.10 is the experimental XL/XF joint reconstruction using the x-ray luminescence and x-ray fluorescence measurements collected in the optical gel phantom with the benchtop

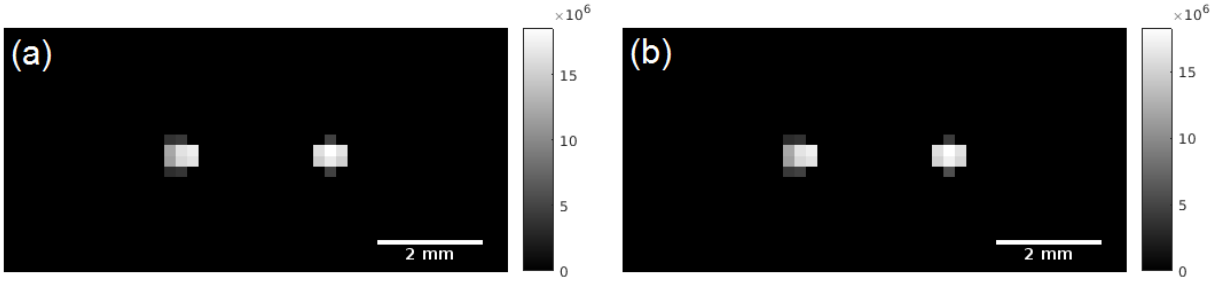

Figure 5.9: XL/XF joint reconstruction which is a deconvolution of the simulated surface radiance using the simulated x-ray fluorescence reconstruction . Figure 5.9 (a) represents the two tube from the calibrated simulation while Figure 5.9 (b) represents the joint reconstruction using the "weak signal" x-ray fluorescence data.

Data	Tube 1 (CNR)	Tube 2 (CNR)
Simulated XL/XF	6.75	13.5
Simulated XF reconstruction	5.66	3.71
Simulated XL/XF (poor XF)	6.68	14.9
Simulated XF reconstruction (poor XF)	1.96	1.23

Table 5.3: Contrast-to-noise ratios for simulated data. The first pair represents the simulated XL/XF joint reconstruction and the simulated x-ray fluorescence data. The second pair is the simulated x-ray fluorescence reconstruction using the "poor quality" XF data and the corresponding XL/XF joint reconstruction. The first column of CNRs represents the tube on the left in the images and the second column represents the tube on the right.

imaging system. The top row represents the x-ray luminescence deconvolution that used the standard x-ray fluorescence reconstruction as a binary mask. The bottom row is the x-ray luminescence deconvolution that used the x-ray fluorescence reconstruction with only 10 % of the originally detected photons. Table 5.4 shows the calculated contrast-to-noise ratios for the experimental XL/XF joint reconstruction and the XF reconstruction.

5.5 Discussion

Dual-modality imaging of x-ray luminescence and x-ray fluorescence is possible depending on the elemental components of the nanophosphors and the x-ray excitation source's energy. The pencil-beam geometry allows for high resolution imaging, due to the narrow focal size

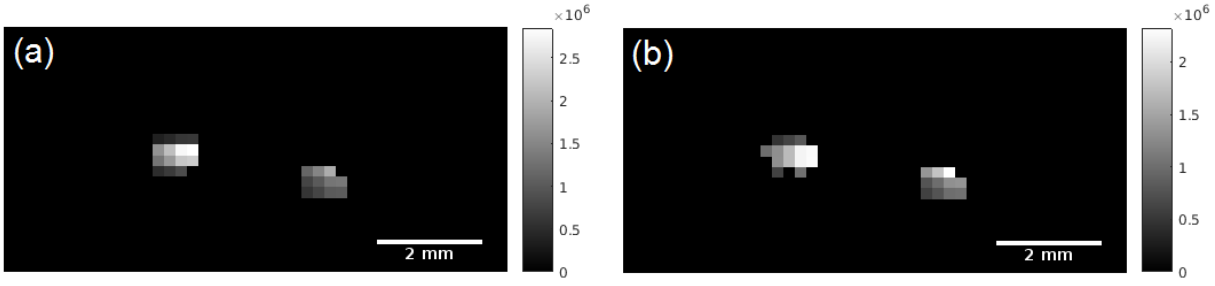

Figure 5.10: XL/XF joint reconstruction on the experimental data collected with the benchtop imaging system. Like in the previous figure, Figure 5.10 (a) represents the data as it was collected by the system and Figure 5.10 (b) is the x-ray luminescence deconvolution using the poor quality x-ray fluorescence image.

Data	Tube 1 (CNR)	Tube 2 (CNR)
Experimental XL/XF	4.16	3.72
Experimental XF reconstruction	1.98	2.24
Experimental XL/XF (poor XF)	4.70	2.99
Experimental XF reconstruction (poor XF)	1.41	1.20

Table 5.4: Contrast-to-noise ratios for experimental data. The first pair represents the experimental XL/XF joint reconstruction and the experimental x-ray fluorescence data. The second pair is the experimental x-ray fluorescence reconstruction using the "poor quality" XF data and the corresponding XL/XF joint reconstruction. The first column of CNRs represents the tube on the left in the images and the second column represents the tube on the right.

of the illumination beam. An experimental benchtop system is presented with with a 17.4 keV monochromatic pencil-beam source, an x-ray CCD camera with a slit aperture, and an EMCCD camera with a demagnifying tube. The $Y_2O_3 : Eu^{3+}$ nanophosphors have an strongly absorbing K-edge slightly below the incident x-ray energy and the yttrium fluoresces 14.9 keV x-rays. The slit aperture is orthogonal to the pencil beam, leading to a simple reconstruction of the detected x-ray fluorescence and a low-exposure regime allows for energy resolution via photon counting. The detected fluorescence signal can then be combined with the x-ray induced luminescence to form a joint reconstruction.

An imaging model for both the x-ray fluorescence and x-ray luminescence are presented for the pencil beam geometry. The x-ray fluorescence model is then calibrated to the mea-

sured x-ray fluorescence data, so that it can be used in simulations to demonstrate the XL/XF joint reconstruction. It is shown that the x-ray luminescence data alone is unable to resolve the two tubes in the optical gel phantom, due to scattering of the luminescent signal at a depth of 8 mm. Incorporating the x-ray fluorescence information into the x-ray luminescence deconvolution however overcomes this drawback. Furthermore, the x-ray luminescence imaging provides greater sensitivity compared to the x-ray fluorescence imaging alone. This is demonstrated in the tables with the contrast-to-noise ratios. In all cases, the XL/XF joint reconstruction for both tubes has a greater CNR than the corresponding XF reconstruction.

The benchtop imaging system presented here is well suited for specimen imaging. One advantage to the joint reconstruction is the ability to recover the object within a given slice without the need to rotate. This cuts down on imaging time and the measurement time could be reduced further as demonstrated by the reconstructions using on 10% of the x-ray fluorescence data per pencil beam position. One drawback to the current setup is that the detectors sit on opposite sides of the object being imaged. This was not an issue for the experimental imaging, because the phantom was designed to be symmetrical. However, in the case when the object is not symmetrical, it could be advantageous to simultaneously image from the the same side. This could be accomplished with a thin mirror that deflects the luminescent signal vertically to be detected by the lens and EMCCD, while allowing for the fluorescent x-rays to pass through to the slit aperture and x-ray CCD behind the mirror.

CHAPTER 6

SUMMARY AND CONCLUSIONS

6.1 Summary

X-ray induced luminescence imaging is a nascent modality using x-ray scintillators as probes for biological study. The dose deposited by radiation releases fast electrons in the tissue that can then activate the imaging probes to emit light via phosphorescence. The literature review demonstrated that a wide variety of applications have been explored, from monitoring drug delivery to molecular imaging. X-ray luminescence is unique compared to other optical imaging modalities due to the penetrating nature of the x-rays that activate the nanophosphors and the ability to shape the incident beam. Researchers have explored various beam geometries such as pencil beam, fan beam, and cone beam, which each have their advantages and drawbacks. Optical imaging in tissue at depths beyond 1-2 mm is an ill-posed problem because there is ambiguity in inferring the distribution of luminescent probes at depth from the detected surface radiance. X-ray luminescence addresses this issue by making the reconstruction more well-posed through selective excitation through various beam geometries.

Initial characterization of the Y_2O_3:Eu^{3+} nanophosphors measured their emission spectrum and demonstrated a linear luminescent response to radiation dose and nanophosphor concentration. These properties were then used in a calibration measurement using bioluminescence and fluorescence mouse phantoms in order to determine the nanophosphors' luminescent efficiency. This was then incorporated into an imaging model along with diffuse optical transport equations and surface radiance detection modeling with a camera and lens. An analytical solution to the surface radiance using the extrapolated boundary condition was used to model the optical diffusion. The x-ray induced luminescence imaging model was applied to experimental measurements in optically homogeneous gel phantoms in order to

calibrate it. Then simulations were carried out using the calibrated imaging model in order to determine the minimum concentration and dose at various depths for a detectable signal at the surface of the tissue.

The x-ray beam was reduced to a two-dimensional geometry using planar x-rays to selectively excite a slice within the object. In the case of an optically homogeneous diffuse environment, the imaging model became a two-dimensional convolution between the luminescence in the plane of excitation and the point spread function for the surface radiance resulting from a point source at the depth of the selective plane. Selective plane x-ray induced luminescence imaging was first demonstrated in an optically clear spiral phantom. Then an optical gel phantom was fabricated containing dual sources of nanophosphors spaced 0.5 cm apart. An iterative deconvolution was applied to the experimental images which could resolve the two tubes up to a depth of 1.75 cm.

Dual-modality imaging was introduced by incorporating x-ray fluorescence imaging with the x-ray induced luminescence. A pencil beam geometry using monochromatic x-rays excited two capillary tubes placed at 0.8 mm depth in an optical gel phantom. The x-ray detector used a slit aperture orthogonal to the pencil-beam and the reconstruction provided a high-resolution image due to minimal scattering of detected fluorescent x-rays. The pencil-beam geometry led to a one-dimensional deconvolution-based reconstruction of the x-ray luminescence signal in which the x-ray fluorescence image could be used as prior information. Simulations and experimental measurements with the benchtop system proved the dual-modality reconstruction showed improved contrast compared to x-ray fluorescence imaging alone. The x-ray fluorescence/x-ray luminescence reconstruction combined the resolution of x-ray imaging with the sensitivity of optical imaging.

6.2 Hurdles to clinical application

Currently x-ray induced luminescence imaging is ill-suited for clinical use. It is difficult to achieve imaging at depth in tissue at a reasonable radiation dose and nanophosphor concentration. Optical imaging at depth in tissue is already challenging due to large amounts of the signal being absorbed. This is further restricted by clinical limits on the radiation dose that is required to generate the optical signal. The sensitivity research demonstrated a minimum detectable signal at depths of 2 to 4 cm for a concentration of 1 mg/mL exposed to 1 cGy of radiation [32]. This was under ideal conditions and without modeling autoluminescence in the air or tissue. This was not detectable for the experimental setup with the f/2.8 lens and cooled CCD, but would be with a more optimal theoretical configuration, thus degrading the sensitivity.

As outlined by Pratx [40], current technology needs to be improved upon before nanophosphors would become suitable for medical imaging. Engineering brighter nanoparticles could mitigate some of the issues with the sensitivity/radiation dose trade-off. Also more research focusing on fabricating nanoparticles with biocompatibility is necessary in order to ensure x-ray induced luminescence imaging can pass regulatory hurdles and be introduced into the clinic. The depth limitations of this technique may restrict applications to superficial diseases in the head and neck region or applications for endoscopic imaging.

6.3 Specimen imaging applications

X-ray induced luminescence imaging could have a viable future in specimen imaging. In these regimes, the objects are much smaller compared to biomedical imaging applications, thus addressing issues concerning sensitivity and loss of optical signal. Furthermore there are fewer limits on the radiation dose required for imaging. The big advantage of x-ray induced luminescence imaging is that the excitation source can be restricted a size below the

diffraction limit of visible light, thus allowing for suboptical-limit imaging [49].

High resolution x-ray imaging has been achieved with synchrotron sources by employing phosphorescent materials as scintillating screens [71]. This approach has been successfully applied to for micro-computed tomography to image millimeter thick slices of mouse brain tissue[72]. X-ray activated nanophosphors could be functionalized for specific molecular targets thus allowing for molecular imaging in tandem with the neuroatonomical microCT. Similarly x-ray fluorescence has been used for specimen imaging, such as staining zebrafish samples with heavy metals[69]. These specimen imaging modalities already require x-ray exposure to the sample. Incorporating nanophosphors and a second detector for x-ray induced luminescence imaging would allow for greater information to be extracted from an imaging session.

Further work need to be done in order to properly model the diffuse light propagation in the heterogeneous structures of specimens. The inverse problem will no longer simplify to a deconvolution as in the optically homogeneous case, but will still be better posed than pure optical imaging without x-ray selective excitation. The heterogeneous x-ray case can itself be made less ill-posed by using anatomical information extracted from the other modalities in the scan. This can in turn could be used to estimate optical properties. Further development of mathematical models for three-dimensional optical imaging in a heterogeneous environment would benefit specimen imaging applications along with other potential images tasks using x-ray luminescence.

6.4 Conclusions

X-ray induced luminescence imaging is an emerging field of study with a wide array of potential imaging applications. It merges the selectiveness of collimated x-rays with the sensitivity of optical imaging and can achieve results that neither modality can alone. This potential can be further enhanced by incorporating x-ray fluorescence detection into an imaging sys-

tem. The physics of diffuse optical imaging can be effectively modeled and used to institute a deconvolution for two-dimensional and one-dimensional x-ray beam geometries. X-ray fluorescence can be included to provided high-resolution imaging of the nanophosphors, which can then be used as prior information for the x-ray luminescence reconstructions. While current nanoparticles lack the brightness to be imaged at doses and concentration relevant to the clinic, future nanoengineering could potentiate x-ray induced luminescence imaging for advanced applications in the next generation of medicine. In their current form, the nanophosphors have potential in the field of micro x-ray imaging with synchrotron sources for functionalized molecular imaging. Further work in optimizing the optical reconstructions based on x-ray beam geometries for heterogeneous environments will serve as valuable research to realizing the full potential of this modality.

REFERENCES

[1] Jorge Ripoll Lorenzo. *Principles of Diffuse Light Propagation: Light Propagation in Tissues with Applications in Biology and Medicine*. World Scientific, 2012.

[2] Michael B. Nelson Bradley W. Rice, Michael D. Cable. In vivo imaging of light-emitting probes. *Journal of Biomedical Optics*, 6:432–440, 2001.

[3] C. W. E. van Eijk. Inorganic scintillators in medical imaging detectors. *Nuclear Instruments and Methods in Physics Research*, 509:17–25, 2003.

[4] Ying Tian, Wang-He Cao, Xi-Xian Luo, and Yao Fu. Preparation and luminescence property of Gd_2O_2S:Tb x-ray nano-phosphors using the complex precipitation method. *Journal of Alloys and Compounds*, 433(1):313–317, 2007.

[5] Ming Ming Xing, Wang He Cao, Tao Pang, Xiao Qiao Ling, and Ning Chen. Preparation and characterization of monodisperse spherical particles of x-ray nano-phosphors based on Gd_2O_2S:Tb. *Chinese Science Bulletin*, 54(17):2982–2986, 2009.

[6] Haiying Wang, Ruji Wang, Xiaoming Sun, Ruoxue Yan, and Yadong Li. Synthesis of red-luminescent Eu^{3+}-doped lanthanides compounds hollow spheres. *Materials Research Bulletin*, 40(6):911 – 919, 2005.

[7] Menglei Chang and Shaolong Tie. Fabrication of novel luminor $Y_2O_3Eu^{3+}$ @ SiO_2 @ YVO_4 : Eu^{3+} with core/shell heteronanostructure. *Nanotechnology*, 19(7):075711, 2008.

[8] Hongyu Chen, David E. Longfield, Venkata S. Varahagiri, KhanhVan T. Nguyen, Amanda L. Patrick, Haijun Qian, Donald G. VanDerveer, and Jeffrey N. Anker. Optical imaging in tissue with x-ray excited luminescent sensors. *Analyst*, 136:3438–3445, 2011.

[9] Hongyu Chen, Amanda L. Patrick, Zhiqiang Yang, Donald G. VanDerveer, and Jeffrey N. Anker. High-resolution chemical imaging through tissue with an x-ray scintillator sensor. *Analytical Chemistry*, 83(13):5045–5049, 2011.

[10] C. M. Carpenter, C. Sun, G. Pratx, R. Rao, and L. Xing. Hybrid x-ray/optical luminescence imaging: Characterization of experimental conditions. *Medical Physics*, 37(8):4011–4018, 2010.

[11] Jeffrey S. Souris, Shih-Hsun Cheng, Charles Pelizzari, Nai-Tzu Chen, Patrick La Riviere, Chin-Tu Chen, and Leu-Wei Lo. Radioluminescence characterization of in situ x-ray nanodosimeters: Potential real-time monitors and modulators of external beam radiation therapy. *Applied Physics Letters*, 105(20):203110, 2014.

[12] Guillem Pratx, Colin M. Carpenter, Conroy Sun, Ravi P. Rao, and Lei Xing. Tomographic molecular imaging of x-ray-excitable nanoparticles. *Opt. Lett.*, 35(20):3345–3347, 2010.

[13] G. Pratx, C. M. Carpenter, C. Sun, and L. Xing. X-ray luminescence computed tomography via selective excitation: A feasibility study. *IEEE Transactions on Medical Imaging*, 29(12):1992–1999, 2010.

[14] Changqing Li, Kun Di, Julien Bec, and Simon R. Cherry. X-ray luminescence optical tomography imaging: experimental studies. *Opt. Lett.*, 38(13):2339–2341, 2013.

[15] Dongmei Chen, Shouping Zhu, Huangjian Yi, Xianghan Zhang, Duofang Chen, Jimin Liang, and Jie Tian. Cone beam x-ray luminescence computed tomography: A feasibility study. *Medical Physics*, 40(3):031111, 2013.

[16] Xin Liu, Qimei Liao, and Hongkai Wang. In vivo x-ray luminescence tomographic imaging with single-view data. *Opt. Lett.*, 38(22):4530–4533, 2013.

[17] Colin Carpenter, Guillem Pratx, Conroy Sun, and Lei Xing. Limited-angle x-ray luminescence tomography: Methodology and feasibility study. *Physics in medicine and biology*, 56:3487–502, 2011.

[18] Xin Liu, Qimei Liao, and Hongkai Wang. Fast x-ray luminescence computed tomography imaging. *IEEE Transactions on Biomedical Engineering*, 61:1621–1627, 2014.

[19] Dongmei Chen, Shouping Zhu, Xueli Chen, Tiantian Chao, Xu Cao, Fengjun Zhao, Liyu Huang, and Jimin Liang. Quantitative cone beam x-ray luminescence tomography/x-ray computed tomography imaging. *Applied Physics Letters*, 105(19):191104, 2014.

[20] Wenxiang Cong, Haiou Shen, and Ge Wang. Spectrally resolving and scattering-compensated x-ray luminescence/fluorescence computed tomography. *Journal of Biomedical Optics*, 16(6):066014, 2011.

[21] Changqing Li, Arnulfo Martinez-Davalos, and Simon R. Cherry. Numerical simulation of x-ray luminescence optical tomography for small-animal imaging. *Journal of Biomedical Optics*, 19(4):046002, 2014.

[22] Colin M Carpenter, Conroy Sun, Guillem Pratx, Hongguang Liu, Zhen Cheng, and Lei Xing. Radioluminescent nanophosphors enable multiplexed small-animal imaging. *Opt. Express*, 20(11):11598–11604, 2012.

[23] Wenxiang Cong, Fenglin Liu, Chao Wang, and Ge Wang. X-ray micro-modulated luminescence tomography (XMLT). *Opt. Express*, 22(5):5572–5580, 2014.

[24] Wenxiang Cong, Zhengwei Pan, Robert J. Filkins, Alok M. Srivastava, A. Nadeem Ishaque, Plamen Stefanov, and Ge Wang. X-ray micromodulated luminescence tomography in dual-cone geometry. *Journal of Biomedical Optics*, 19(7):076002, 2014.

[25] Wenxiang Cong, Chao Wang, and Ge Wang. Stored luminescence computed tomography. *Appl. Opt.*, 53(25):5672–5676, 2014.

[26] M. Ahmad, G. Pratx, M. Bazalova, and L. Xing. X-ray luminescence and x-ray fluorescence computed tomography: New molecular imaging modalities. *IEEE Access*, 2:1051–1061, 2014.

[27] Xin Liu, Hongkai Wang, and Zhuangzhi Yan. Chapter 13 - Nanobiomaterials in x-ray luminescence computed tomography (XLCT) imaging. In Alexandru Mihai Grumezescu, editor, *Nanobiomaterials in Medical Imaging*, pages 403 – 420. William Andrew Publishing, 2016.

[28] Adam K. Glaser, William H. A. Voigt, Scott C. Davis, Rongxiao Zhang, David J. Gladstone, and Brian W. Pogue. Three-dimensional Cerenkov tomography of energy deposition from ionizing radiation beams. *Opt. Lett.*, 38(5):634–636, 2013.

[29] Brian W. Pogue. High resolution molecular imaging with cerenkov excited luminscence scanned imaging (CELSI). *Optics in the Life Sciences*, page BM3A.1, 2015.

[30] Jinchao Feng, Petr Bruza, Hamid Dehghani, Scott C. Davis, and Brian W. Pogue. Cherenkov-excited luminescence sheet imaging (celsi) tomographic reconstruction. *Proc.SPIE*, 10049:10049 – 10049 – 6, 2017.

[31] Wenxiang Cong and Ge Wang. X-ray fan-beam luminescence tomography. *Austin Journal of Biomedical Engineering*, 1(5):1024, 2014.

[32] Bryan P. Quigley, Corey D. Smith, Shih-Hsun Cheng, Jeffrey S. Souris, Charles A. Pelizzari, Chin-Tu Chen, Leu-Wei Lo, Chester S. Reft, Rodney D. Wiersma, and Patrick J. La Riviere. Sensitivity evaluation and selective plane imaging geometry for x-ray-induced luminescence imaging. *Medical Physics*, 44(10):5367–5377, 2017.

[33] Wei Zhang, Dianwen Zhu, Michael Lun, and Changqing Li. Multiple pinhole collimator based x-ray luminescence computed tomography. *Biomed. Opt. Express*, 7(7):2506–2523, 2016.

[34] S. Tzoumas, D. Vernekohl, and L. Xing. Coded-aperture compressed sensing x-ray luminescence tomography. *IEEE Transactions on Biomedical Engineering*, 2017. This article has been accepted for publication in a future issue of this journal, but has not been fully edited.

[35] Changqing Li Wei Zhang, Michael Lun. Fiber based fast sparse sampling x-ray luminescence computed tomography. *Proc.SPIE*, 10057:1005704, 2017.

[36] Wei Zhang, Michael C. Lun, Alex Anh-Tu Nguyen, and Changqing Li. X-ray luminescence computed tomography using a focused x-ray beam. *Journal of Biomedical Optics*, 22(11):1–11, 2017.

[37] G. Zhang, F. Liu, J. Liu, J. Luo, Y. Xie, J. Bai, and L. Xing. Cone beam x-ray luminescence computed tomography based on bayesian method. *IEEE Transactions on Medical Imaging*, 36(1):225–235, 2017.

[38] Tianshuai Liu, Junyan Rong, Peng Gao, Wenlei Liu, and Hongbing Lu. Cone-beam x-ray luminescence computed tomography based on x-ray absorption dosage. In *The 14th International Meeting on Fully Three-Dimensional Image Reconstruction in Radiology and Nuclear Medicine*, volume 14, pages 281–285, Xi'an, 2017.

[39] Michael C. Lun, Wei Zhang, and Changqing Li. Sensitivity study of x-ray luminescence computed tomography. *Appl. Opt.*, 56(11):3010–3019, 2017.

[40] Guillem Pratx. A tale of two photons: radioluminescence and its application in molecular imaging. *Proc.SPIE*, 10049:1004916, 2017.

[41] Michael C. Lun and Changqing Li. X-ray luminescence imaging of water, air, and tissue phantoms. *Proc.SPIE*, 10487:10487 – 10487 – 12, 2018.

[42] Conroy Sun, Guillem Pratx, Colin M. Carpenter, Hongguang Liu, Zhen Cheng, Sanjiv Sam Gambhir, and Lei Xing. Synthesis and radioluminescence of pegylated eu3+-doped nanophosphors as bioimaging probes. *Advanced Materials*, 23(24):H195–H199, 2011.

[43] Wenli Zhang, Yingli Shen, Miao Liu, Peng Gao, Huangsheng Pu, Li Fan, Ruibin Jiang, Zonghuai Liu, Feng Shi, and Hongbing Lu. Sub-10 nm water-dispersible β -NaGdF^4:X % Eu^{3+} nanoparticles with enhanced biocompatibility for in vivo x-ray luminescence computed tomography. *ACS Applied Materials & Interfaces*, 9(46):39985–39993, 2017.

[44] Yasuko Osakada, Guillem Pratx, Conroy Sun, Masanori Sakamoto, Moiz Ahmad, Olga Volotskova, Qunxiang Ong, Toshiharu Teranishi, Yoshie Harada, Lei Xing, and Bianxiao Cui. Hard x-ray-induced optical luminescence via biomolecule-directed metal clusters. *Chem. Commun.*, 50:3549–3551, 2014.

[45] Cheng Wang, Olga Volotskova, Kuangda Lu, Moiz Ahmad, Conroy Sun, Lei Xing, and Wenbin Lin. Synergistic assembly of heavy metal clusters and luminescent organic bridging ligands in metalorganic frameworks for highly efficient x-ray scintillation. *Journal of the American Chemical Society*, 136(17):6171–6174, 2014.

[46] Xueli Chen, Jimin Liang, Xin Cao, Defu Yang, Dongmei Chen, Jorge Ripoll, and Jie Tian. Feasibility study of endoscopic x-ray luminescence computed tomography: Simulation demonstration and phantom application. *Journal of Applied Physics*, 114(8):084701, 2013.

[47] Thomas L. Moore, Fenglin Wang, Hongyu Chen, Stuart W. Grimes, Jeffrey N. Anker, and Frank Alexis. Polymer-coated radioluminescent nanoparticles for quantitative imaging of drug delivery. *Advanced Functional Materials*, 24(37):5815–5823, 2014.

[48] Donald Benza, Unaiza Uzair, Yash Raval, Tzuen-Rong J. Tzeng, Caleb J. Behrend, and Jeffrey N. Anker. X-ray excited luminescent chemical imaging (XELCI) for non-invasive imaging of implant infections. *Proc.SPIE*, 10081:100810K, 2017.

[49] C. Jacobsen, S. Lindaas, S. Williams, and X. Zhang. Scanning luminescence xray microscopy: Imaging fluorescence dyes at suboptical resolution. *Journal of Microscopy*, 172(2):121–129, 1993.

[50] Damon Hyde, Ralf Schulz, Dana Brooks, Eric Miller, and Vasilis Ntziachristos. Performance dependence of hybrid x-ray computed tomography/fluorescence molecular tomography on the optical forward problem. *J. Opt. Soc. Am. A Opt. Image Sci. Vis.*, 26(4):919–923, 2009.

[51] C. M. Carpenter, C. Sun, G. Pratx, R. Rao, and L. Xing. Hybrid x-ray/optical luminescence imaging: Characterization of experimental conditions. *Medical Physics*, 37(8):4011–4018, 2010.

[52] C.-M. Ma, C. W. Coffey, L. A. DeWerd, C. Liu, R. Nath, S. M. Seltzer, and J. P. Seuntjens. AAPM protocol for 40–300 kV x-ray beam dosimetry in radiotherapy and radiobiology. *Medical Physics*, 28(6):868–893, 2001.

[53] Rinaldo Cubeddu, Antonio Pifferi, Paola Taroni, Alessandro Torricelli, and Gianluca Valentini. A solid tissue phantom for photon migration studies. *Phys. Med. Biol.*, 42(10):1971–9, 1997.

[54] Steven L Jacques. Optical properties of biological tissues: a review. *Physics in Medicine and Biology*, 58(11):R37–61, 2013.

[55] Brian W. Pogue Simon Jacques. Tutorial on diffuse light transport. *Journal of Biomedical Optics*, 13:041302, 2008.

[56] Richard C. Haskell, Lars O. Svaasand, Tsong-Tseh Tsay, Ti-Chen Feng, Matthew S. McAdams, and Bruce J. Tromberg. Boundary conditions for the diffusion equation in radiative transfer. *J. Opt. Soc. Am. A*, 11(10):2727–2741, 1994.

[57] Harrison H. Barrett and Kyle J. Myers. *Foundations of Image Science*. Wiley-Interscience, 2003.

[58] Kuangda Lu, Chunbai He, and Wenbin Lin. Nanoscale metalorganic framework for highly effective photodynamic therapy of resistant head and neck cancer. *Journal of the American Chemical Society*, 136(48):16712–16715, 2014.

[59] Adam K. Glaser, Rongxiao Zhang, Scott C. Davis, David J. Gladstone, and Brian W. Pogue. Time-gated Cherenkov emission spectroscopy from linear accelerator irradiation of tissue phantoms. *Opt. Lett.*, 37(7):1193–1195, 2012.

[60] Rongxiao Zhang, Adam K. Glaser, Jacqueline Andreozzi, Shudong Jiang, Lesley A. Jarvis, David J. Gladstone, and Brian W. Pogue. Beam and tissue factors affecting cherenkov image intensity for quantitative entrance and exit dosimetry on human tissue. *Journal of Biophotonics*, 10(5):645–656, 2016.

[61] Jan Huisken, Jim Swoger, Filippo Del Bene, Joachim Wittbrodt, and Ernst H. K. Stelzer. Optical sectioning deep inside live embryos by selective plane illumination microscopy. *Science*, 305(5686):1007–1009, 2004.

[62] Petr Brůža, Huiyun Lin, Sergei A. Vinogradov, Lesley A. Jarvis, David J. Gladstone, and Brian W. Pogue. Light sheet luminescence imaging with Cherenkov excitation in thick scattering media. *Opt. Lett.*, 41(13):2986–2989, 2016.

[63] Donald L. Snyder, Abed M. Hammoud, and Richard L. White. Image recovery from data acquired with a charge-coupled-device camera. *J. Opt. Soc. Am. A*, 10(5):1014–1023, 1993.

[64] Donald L. Snyder, Carl W. Helstrom, Aaron D. Lanterman, Mohammad Faisal, and Richard L. White. Compensation for readout noise in CCD images. *J. Opt. Soc. Am. A*, 12(2):272–283, 1995.

[65] P. J. La Riviere, Junguo Bian, and P. A. Vargas. Penalized-likelihood sinogram restoration for computed tomography. *IEEE Transactions on Medical Imaging*, 25(8):1022–1036, 2006.

[66] William Hadley Richardson. Bayesian-based iterative method of image restoration. *J. Opt. Soc. Am.*, 62(1):55–59, 1972.

[67] L. B. Lucy. An iterative technique for the rectification of observed distributions. *Astron. J.*, 79:745–754, 1974.

[68] Yicong Wu, Peter Wawrzusin, Justin Senseney, Robert S Fischer, Ryan Christensen, Anthony Santella, Andrew G York, Peter W Winter, Clare M Waterman, Zhirong Bao, Daniel A Coln-Ramos, Matthew McAuliffe, and Hari Shroff. Spatially isotropic four-dimensional imaging with dual-view plane illumination microscopy. *Nature Biotechnology*, (31):1032, 2013.

[69] G. Fu, L.J. Meng, P. Eng, M. Newville, P. Vargas, and P.J. La Riviere. Experimental demonstration of novel imaging geometries for x-ray fluorescence computed tomography. *Medical Physics*, 40(6):061903, 2013.

[70] A. Groll, J. George, P. Vargas, P. J. La Rivire, and L. J. Meng. Element mapping in organic samples utilizing a benchtop x-ray fluorescence emission tomography (XFET) system. *IEEE Transactions on Nuclear Science*, 62(5):2310–2317, Oct 2015.

[71] Thierry Martin and Andreas Koch. Recent developments in X-ray imaging with micrometer spatial resolution. *Journal of Synchrotron Radiation*, 13(2):180–194, 2006.

[72] Eva L. Dyer, William Gray Roncal, Judy A. Prasad, Hugo L. Fernandes, Doga Gürsoy, Vincent De Andrade, Kamel Fezzaa, Xianghui Xiao, Joshua T. Vogelstein, Chris Jacobsen, Konrad P. Körding, and Narayanan Kasthuri. Quantifying mesoscale neuroanatomy using x-ray microtomography. *eNeuro*, 4(5):e0195–17, 2017.